NASA/TM–2010-215863

The Interaction of the Solar Wind with *Solar Probe Plus* — 3D Hybrid Simulation

Report 2: The study for the distance 9.5Rs

Alexander S. Lipatov, Edward C. Sittler, Richard E. Hartle, and John F. Cooper

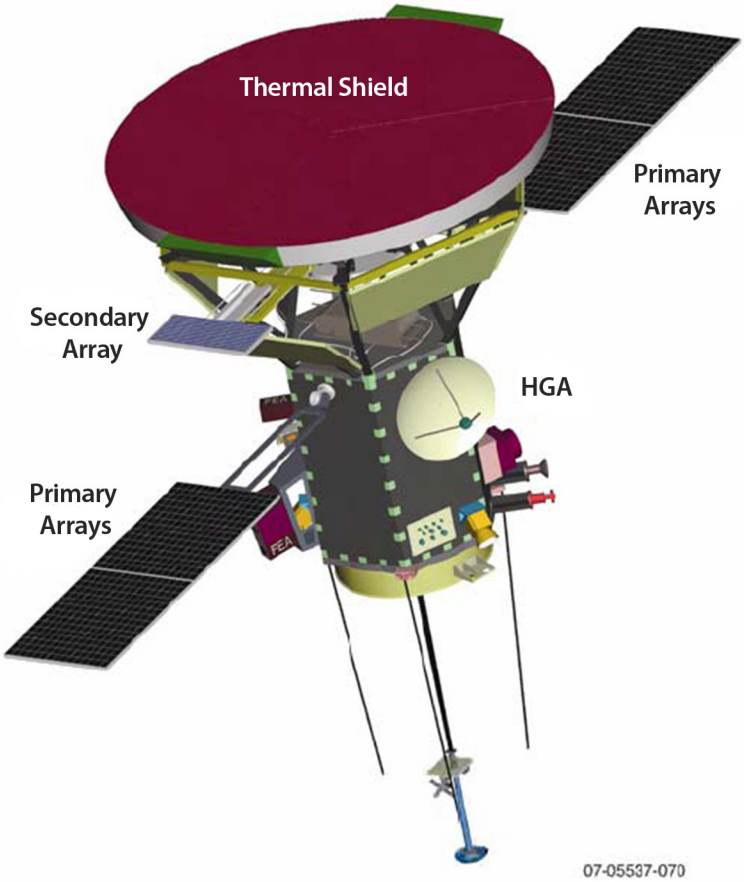

December 2010

The NASA STI Program Office … in Profile

Since its founding, NASA has been dedicated to the advancement of aeronautics and space science. The NASA Scientific and Technical Information (STI) Program Office plays a key part in helping NASA maintain this important role.

The NASA STI Program Office is operated by Langley Research Center, the lead center for NASA's scientific and technical information. The NASA STI Program Office provides access to the NASA STI Database, the largest collection of aeronautical and space science STI in the world. The Program Office is also NASA's institutional mechanism for disseminating the results of its research and development activities. These results are published by NASA in the NASA STI Report Series, which includes the following report types:

- TECHNICAL PUBLICATION. Reports of completed research or a major significant phase of research that present the results of NASA programs and include extensive data or theoretical analysis. Includes compilations of significant scientific and technical data and information deemed to be of continuing reference value. NASA's counterpart of peer-reviewed formal professional papers but has less stringent limitations on manuscript length and extent of graphic presentations.
- TECHNICAL MEMORANDUM. Scientific and technical findings that are preliminary or of specialized interest, e.g., quick release reports, working papers, and bibliographies that contain minimal annotation. Does not contain extensive analysis.
- CONTRACTOR REPORT. Scientific and technical findings by NASA-sponsored contractors and grantees.
- CONFERENCE PUBLICATION. Collected papers from scientific and technical conferences, symposia, seminars, or other meetings sponsored or cosponsored by NASA.
- SPECIAL PUBLICATION. Scientific, technical, or historical information from NASA programs, projects, and mission, often concerned with subjects having substantial public interest.
- TECHNICAL TRANSLATION. English-language translations of foreign scientific and technical material pertinent to NASA's mission.

Specialized services that complement the STI Program Office's diverse offerings include creating custom thesauri, building customized databases, organizing and publishing research results . . . even providing videos.

For more information about the NASA STI Program Office, see the following:

- Access the NASA STI Program Home Page at http://www.sti.nasa.gov/STI-homepage.html
- E-mail your question via the Internet to help@sti.nasa.gov
- Fax your question to the NASA Access Help Desk at (443) 757-5803
- Telephone the NASA Access Help Desk at (443) 757-5802
- Write to:
  NASA Access Help Desk
  NASA Center for AeroSpace Information
  7115 Standard Drive
  Hanover, MD 21076

NASA/TM–2010-215863

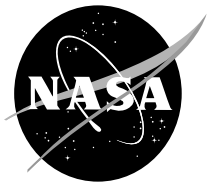

The Interaction of the Solar Wind with *Solar Probe Plus* — 3D Hybrid Simulation

Report 2: The study for the distance 9.5Rs

Alexander S. Lipatov
The Goddard Earth Sciences and Technology Center,
University of Maryland, Baltimore County, Baltimore, MD

Edward C. Sittler
NASA Goddard Space Flight Center Greenbelt, MD

Richard E. Hartle
NASA Goddard Space Flight Center Greenbelt, MD

John F. Cooper
NASA Goddard Space Flight Center Greenbelt, MD

Prepared under NASA Grant NCC5–494

January 1, 2009 to September 1, 2010
Prepared for Dr. Madhulika Guhathakurta
NASA Headquarters, Code SMD
Washington, DC 20546

National Aeronautics and
Space Administration

Goddard Space Flight Center
Greenbelt, Maryland 20771

December 2010

Available from:

NASA Center for AeroSpace Information
7115 Standard Drive
Hanover, MD 21076-1320

National Technical Information Service
5285 Port Royal Road
Springfield, VA 22161

Abstract. Our report are the 2.5D and 3D numerical models of the interaction of the solar wind with the Solar Probe Plus (SPP) spacecraft. These results should be interpreted as an engineering document for which the derived SW interaction with SP+ could have consequences for both plasma wave and electron plasma observations. The SPP model includes 3 main parts, namely, a non-conducting heat shield, a support system, and cylindrical section or spacecraft bus that contains the particle analysis devices and antenna. The simulation was performed using 3D hybrid code which describes proton dynamics by particle motions whereas the electrons are considered in a fluid approximation. The results of the quasi-parallel and quasi-perpendicular solar wind – SPP interaction at the distance $r = 4.5R_s$ were discussed in the preliminary Report (Lipatov, Hartle and Sittler, 2009). In present Report we discuss the results of simulation of the solar wind – spacecraft quasi-parallel interaction at the distance $r = 9.5R_s$. In this regime the value of the ion thermal velocity is about of the value of the bulk velocity and the polarization electric filed is strong enough so that only a very small cavern is formed behind the heat shield and the bus. One observes an excitation of the low frequency Alfvén and whistler type wave directed by the magnetic field with an amplitude of the electromagnetic field oscillation about of (0.06-1.5) V/m. The compression waves and the jumps in an electric field with an amplitude of about (0.15-1.5) V/m were also observed. The results of our hybrid simulation will be useful for understanding the plasma environment near the SP+ spacecraft. Future simulation will take into account charging of the spacecraft, charge separation effects, outgassing from the heat shield, photoionization and electron impact ionization effects near

the spacecraft. We also need to perform a longer simulation in order to receive a "steady-state" solution with formation of a plasma wake in a quasi-parallel interaction. We are now in a position to do this, since these codes have now been converted to the hybrid MPI/OpenMP environment and can now run on the Pleiades and Discover massively-parallel supercomputers with distributed memory.

Numerical simulation studies; **Key words:** Solar wind; Spacecraft; Alfvén waves, Whistlers, Ionospheres; Atmospheres; Induced magnetospheres; Magnetic barrier; Satellites

1. Introduction

The numerical simulation of the interaction of space plasma with spacecraft devices plays a key-role in their design. The study of the excitation of waves near a rapidly moving body has long history starting from the quasi-analytical approach (see e.g. Alpert (1974) and the references thereby) to the recent electrostatic modeling. While the electrostatic studies produced very important information concerning the charging of spacecraft, plasma void and wake, the problem of excitation of the electromagnetic waves upstream and downstream flow near spacecraft are great interest for onboard measurement in the SW, magnetosphere and ionosphere. This is especially true for SPP where new regimes of solar wind plasma are being explored. The simulation provides the general characteristics of the plasma environment and the electromagnetic field distribution near the probe and at it's surface. The external surface of the Solar Probe Plus consists of a conducting part and an insulating part. It moves in the supersonic/subsonic and superalfvénic/subalfvénic solar wind flow.

In the first approximation the plasma environment near the Solar Probe+ may be similar to the plasma environment near the Moon with a weakly conducting surface. In the case of a non-conducting model of the Moon the solar wind particles penetrate the surface on the day-side of the Moon whereas on the night-side a plasma wake with the low-density void is formed. On the day side of the Moon's surface the plasma particles are absorbed, and the perturbation region forms a thin boundary layer of thickness $\delta \sim c/\omega_{\rm pe} \propto 1\,{\rm km}$ at 1 AU. (Neugebauer, 1960). On the night side the perturbation region is bounded by a surface of weak perturbations forming a cone with half-apex

angle $\sin^2\theta = 1/M_{\rm A}^2 + 1/M_{\rm S}^2$ ($M_{\rm A} \propto 8$ and $M_{\rm S} \propto 8$ are the Alfvén and sound Mach numbers, $V_A \approx 50\,{\rm km/s}$, $w_{th} \approx 50\,{\rm km/s}$, $U \approx 400\,{\rm km/s}$, and $\theta \approx 10^\circ$) (Whang, 1969; Lipatov, 1976).

No bow shock or oblique Mach cone are formed. The perturbation of the magnetic field inside the plasma wake is mostly determined by diamagnetic current and the drift currents due to a curvature of the magnetic field and acceleration of the bulk velocity [Wang, 1968; Wang, 1969; Wang and Ness, 1970; Lipatov 1976, Lipatov, 2002]. Kinetic instabilities may also play a role in wake dynamics. Hybrid simulation of the interaction between supersonic plasma flow and a weakly conducting body shows formation of a strong oblique double shock structure inside the plasma wake [Lipatov, Motschmann, et al., 2005].

2. Formulation of the Problem and Mathematical Model

2.1. Solar Wind Simulation Model

The interaction of solar wind particles with the "Solar Probe+" is more complicated because the gyroradius of the protons (for Maxwellian core of the velocity distribution $50 - 500\,{\rm km}$) is much larger than the size of the spacecraft (2-3m). For energetic components the ion gyroradius may be extremely large with respect to the spacecraft. So the kinetic approximation for ions is an essential part of the mathematical model. The electron gyroradius may vary in range from 2.5×10^2m at Earth orbit to much smaller scale, 1 m, near Sun. Therefore, electrons need a fluid-kinetic approximation to study the plasma environment along the "Solar Probe+" trajectory.

We study the plasma environment near the "Solar Probe+" by various simulations; e.g., (a) standard hybrid simulation (ion in kinetic approximation, electron in fluid approach) on the large scale; (b) fully kinetic implicit simulation with kinetic model for electrons and ions (see e.g. Hewett and Langdon, 1987; Lipatov and Lobachev, 1996; Lipatov, 2002; Damiano, Sydora, Samson, 2003; Lipatov and Rankin, 2008) incorporated in the large scale hybrid model. The last simulation will take into account charge separation near the surface of the spacecraft and finite electron gyroradius effects. We will take into account the realistic distribution of the spacecraft surface's conductivity. Our simulation will serve as an expert system for design of the "Solar Probe+" spacecraft. The present model of the interaction of the solar wind with the SP+ does not take into account several effects in plasma environment near the spacecraft. Future simulation will take into account the charging of the spacecraft, charge separation effects, outgassing from heat shield, photoionization and electron impact ionization effects near the spacecraft.

To study the interaction of the solar wind with the SP+ spacecraft we use a quasi-neutral hybrid model for ions and electrons.

In our coordinate system the X (radial) axis is parallel to the solar wind velocity - $\mathbf{U_0}$, Z is aligned with the equatorial plane, and $\mathbf{Y} = \mathbf{Z} \times \mathbf{X}$, Fig. 1.

In the hybrid simulations described here, the dynamics of upstream ions is described by kinetic approach, while the dynamics of the electrons is described by a hydrodynamical approximation.

The single particle ion distribution function $f_i(t, \mathbf{x}, \mathbf{v})$ has to satisfy the

Vlasov/Boltzmann equation

$$\frac{\partial}{\partial t} f_i + \mathbf{v} \frac{\partial}{\partial \mathbf{x}} f_i + \frac{\mathbf{F}}{M_i} \frac{\partial}{\partial \mathbf{v}} f_i = F_{coll}, \tag{1}$$

where $\mathbf{F}$ symbolizes forces due to electric and magnetic fields acting on the ions, F_{coll} is the collision term. In this paper we use the particle-mesh model for ion dynamics instead of the Vlasov equation, Eq. (1).

The single ion particle motion is described by the equations (see, e.g. Eqs. (1) and (14) from [Mankofsky, Sudan and Denavit, 1987]):

$$\frac{d\mathbf{r}_{i,l}}{dt} = \mathbf{v}_{i,l}; \quad \frac{d\mathbf{v}_{i,l}}{dt} = \frac{e}{M_\mathrm{i}} \left(\mathbf{E} + \frac{\mathbf{v}_{i,l} \times \mathbf{B}}{c} \right) - \frac{m_e \nu_{ie}}{M_i e n_i} \mathbf{J}. \tag{2}$$

Here we assume that the charge state is $Z_i = 1$ and that all ions have the same mass M_i. $\mathbf{U}_i$ and $\mathbf{J}$ denote the charge-averaged velocity of all (incoming and pickup) ions and the total current, Eq. (6). The subscript i denotes the ion population and the index l is the macro-particle index. ν_{ie} is collision frequency between ions and electrons, that may include Coulomb collisions and collisions due to particle-wave interaction. Note that the collision rates used in Eq. (2) must depend on the individual velocities of ions and electrons. However, we use the effective resistivity η, $\eta = \sigma^{-1} = m_e/(ne^2\tau_e)$, where $\tau_e = \nu_{ie}^{-1}$. The electrical conductivities may be estimated as

$$\sigma_\perp = \sigma_1 T_e^{3/2}, \quad \sigma_\parallel = 1.92\sigma_\perp, \quad \sigma_1 = 0.9 \times 10^{13}/((\Lambda/10)Z_i)\,\mathrm{s}^{-1} \cdot \mathrm{eV}^{-3/2}, \tag{3}$$

where T_e denotes the electron temperature and Λ is the Coulomb logarithm (see, e.g., pages 215-216 from [Braginskii, 1965]). For typical solar wind parameters $T_e = 100\,\mathrm{eV}$

(electron temperature), $n_0 = 10^4 \mathrm{cm}^{-3}$ (density), and electrical conductivities are $\sigma_\perp \approx 4.7 \times 10^{13}\,\mathrm{s}^{-1}$ and $\sigma_\parallel \approx 9.2 \times 10^{13}\,\mathrm{s}^{-1}$.

In our simulation we use the value of the effective conductivity that is much smaller than the real value to suppress "shot" noise. The numerical "shot" noise is a result of a fluctuation in density and bulk velocity due to a small number of particles per cell in the particle in cell simulation. We also use an effective conductivity for modeling Solar Probe+'s bus. Hence, we must keep the first collision term in the right hand side of Eq. (2).

In the nonradiative limit Ampère's law is given by

$$\frac{4\pi}{c}\mathbf{J} = \nabla \times \mathbf{B}; \tag{4}$$

and the induction equation (Faraday's law) by

$$\frac{1}{c}\frac{\partial \mathbf{B}}{\partial t} + \nabla \times \mathbf{E} = 0. \tag{5}$$

The total current is given by

$$\mathbf{J} = \mathbf{J}_\mathrm{e} + \mathbf{J}_\mathrm{i}; \quad \mathbf{J}_\mathrm{i} = e n_i \mathbf{U}_i. \tag{6}$$

We further assume quasi-neutrality

$$n_\mathrm{e} \approx n_i. \tag{7}$$

The equation of motion of the electron fluid takes the form of the standard generalized Ohm's law (e.g. Braginskii, 1965):

$$\mathbf{E} = \frac{1}{e n_\mathrm{e} c}(\mathbf{J}_\mathrm{e} \times \mathbf{B}) - \frac{1}{e n_\mathrm{e}}\nabla p_\mathrm{e} + \frac{m_\mathrm{e}}{e}\nu_{e,i}\frac{\mathbf{J}}{ne} - \frac{m}{e}\frac{d}{dt}\mathbf{U}_e, \tag{8}$$

where $p_e = nm_e\langle v_e'^2\rangle/3 = n_e k_B T_e$, and v_e' are the scalar electron pressure and the thermal velocity of electrons, and the electron current is estimated from Eq. (6). The last term on the right side of Eq. (8) is the electron inertial term. At $5R_s$ we have $n_0 = 10^4\,\mathrm{cm}^{-3}$, $v_e' = 5000\,\mathrm{km/s}$, and from Eq. (3) one gets $\sigma_{e,i} = 0.4 \times 10^{14}\,\mathrm{s}^{-1}$ for background plasma parameters.

Since we suppose that electron heating due to collisions with ions is very small, the electrons are considered as adiabatic fluid. For simplicity we assume that the electron pressure may be represented as:

$$p_e \propto n_i^{5/3}. \tag{9}$$

We also assume that $n_e \approx n_i$. Otherwise, we have to calculate the electron pressure from heat balance for electrons (see, e.g., Braginski, 1965) taking into account the heat fluxes. The hybrid model allows us to study the dynamics of the ion velocity distribution and the effects of a finite ion gyroradius. The electron gyroradius and charge separation effects are not resolved in hybrid models and we have to use a full kinetic model in future simulations.

2.2. Solar Probe Plus Spacecraft Model

Figure 1 shows a scheme of the Solar Probe Plus (SP+) spacecraft, a system of coordinates and a direction of the plasma flow and magnetic field. The SP+ model includes 3 main parts, namely, a non-conducting heat shield (1), a support system (2), and a cylindrical section or spacecraft bus (3) that contains the particle analysis devices and antenna. The heat shield has the following geometrical parameters: diameter,

$D_{shield} = 2.7\,\mathrm{m}$, and thickness $= 0.335\,\mathrm{m}$. The gap between the heat shield and cylindrical section is 1.188 m. Note the gap is now covered with radiators, so there is no penetration of the solar wind through the radiators. The cylindrical section or bus has a diameter of 1.026 m and length 1.188 m. We also take into account the effective resistivity of the Solar Probe+'s bus, the heat shield and the gap between the heat shield and the spacecraft bus:

$$\rho_{bus} = (1-15)\times 10^{-3}\, ohm\cdot m; \quad \rho_{shield} = (3-15)\, ohm\cdot m; \quad \rho_{gap} = (3-15)\times 10^{-3}\, ohm\cdot m \tag{10}$$

Our code solves equations (1) - (5), (6) - (9) (Lipatov, Hartle, Sittler, 2009). Here we note that the gap has several trusses to provide a mechanical interface between bus and heat shield. If electrical conductivity of trusses is high enough that differential charging between spacecraft bus and heat shield is low, then the heat conduction from heat shield to spacecraft bus may be too high. We still don't know the exact value at this time with regard to truss electrical conductivity parameters.

Initially the computational domain contains only supersonic or subsonic solar wind flow with a homogeneous spatial distribution. The magnetic field and electric fields are $\mathbf{B} = \mathbf{B}_0$ and $\mathbf{E} = \mathbf{E_0} = -\mathbf{U}_0 \times \mathbf{B}_0$. Inside the Solar Probe+ spacecraft the electromagnetic fields are $\mathbf{E} = 0$ and $\mathbf{B} = \mathbf{B}_0$, and bulk velocities of ions and electrons are also equal to zero. In the cases examined here we choose for the magnetic field a spiral angle $\theta_{bu} = 11^\circ$.

Far upstream ($x = -DX/2$), the ion flux is assumed to have a Maxwellian

distribution,

$$f = n_\infty (\pi v_{th}^2)^{-3/2} \exp\left[-\frac{(\mathbf{v}-\mathbf{U})^2}{2v_{th}^2}\right], \tag{11}$$

where v_{th} and $\mathbf{U}$ are the thermal and the bulk velocities of the solar wind plasma flow. We have not included a contribution from the field aligned strahl electrons which are non-Maxwellian.

Far downstream, we use a buffer zone to provide the return of particles with negative values of the u velocity component. We also adopted Sommerfeld's radiation condition for the magnetic field. On the side boundaries ($y = \pm DY/2$ and $z = \pm DZ/2$), unperturbed boundary conditions were imposed for the incoming flow particles and the electromagnetic field. At the spacecraft surface the particles are absorbed. There is no boundary condition for electromagnetic fields, and we also use our equations for the electromagnetic field inside the spacecraft but with internal conductivity and the bulk velocity that is calculated from the particles. In this way the jump in the electric field is due to the variation of the values of the conductivity and bulk velocity across the surface of the spacecraft PS+. The position of the center of the bottom of the heat shield is defined as $x = 0, y = 0, z = 0$.

The three-dimensional computational domain has dimensions $DX = 10L$, $DY = 8L$, and $DZ = 8L$, where $L = D_{shield}/2 = 1.35\,\mathrm{m}$ is the radius of the heat shield. We use a mesh of $401 \times 301 \times 301$ grid points, and 9×10^8 particles for protons in a homogeneous mesh computation. We use a subcycling procedure for time integration of the particle and the electromagnetic equations (see, e.g. Lipatov 2002). The time step for the particle

update, Δt_p satisfies the condition $v_{max}\Delta t_p \leq \min(\Delta x, \Delta y, \Delta z)/16$, whereas the time step for the electromagnetic field time integration, Δt_f, is much smaller than the time step for particle update. Δt_f satisfies the condition $v_{max}\Delta t_f \leq \min(\Delta x, \Delta y, \Delta z)/6400$. The grid spacings are as follows: $\Delta x = \Delta y = \Delta z = 0.036\,\mathrm{m}$.

The relationships between dimensional ($\mathbf{U}$, $\mathbf{E}$, $\mathbf{B}$, p_e, n, T) and dimensionless ($\mathbf{U}'$, $\mathbf{E}'$, $\mathbf{B}'$, p'_e, n', T') parameters may be expressed via the dimensional upstream values as follows:

$$\mathbf{U} = \mathbf{U}'U_0, \quad \mathbf{E} = \mathbf{E}'B_0U_0/c, \quad \mathbf{B} = \mathbf{B}'B_0, \quad p_\mathrm{e} = p_{e'}p_{e0},$$

$$n = n'n_0, \quad T = T'M_\mathrm{i}U_0^2, \tag{12}$$

whereas the dimensional time and distance may be expressed via the bulk velocity U_0 and characteristic scale $L = D_{shield}/2$:

$$t = t'L/U_0, \quad x = x'L. \tag{13}$$

The global physics in SP+'s environment is controlled by a set of dimensionless independent parameters such as Alfvén Mach number M_A, ion and electron plasma betas β_i, β_e, electron/proton mass ratio m/M_p, diffusion lengths, and the gyroradius $\epsilon = \rho_\mathrm{ci}/L$. Here $\rho_\mathrm{ci} = U_0/(eB/M_\mathrm{i}c) = M_\mathrm{A}c/\omega_\mathrm{pi}$ and the ion plasma frequency $\omega_\mathrm{pi} = \sqrt{4\pi n_0 e^2/M_\mathrm{i}}$. The actual value of the proton gyroradius is about $(0.31 - 2.5)\,\mathrm{km}$ using the above formulas. The grid spacing has the value $\Delta_x = L/50 = 0.036\,\mathrm{m}$. In order to model the ion kinetics, the ion gyroradius must be resolved on the grid.

2.3. Numerical Method

We employed a standard particle-in-cell (PIC) method with a homogeneous grid. The time integration of the particle equations of motion uses a trapezoidal leapfrog scheme (see e.g., Lipatov, 2002). The time integration of the electromagnetic field equations uses an implicit finite difference scheme (see, e.g., Lipatov (2002)).

Equation (8) is evaluated at a time level between the n and $n+1$ levels. The electric and magnetic fields at this time level, $n+\theta$, are given by

$$\mathbf{E}^{n+\theta} = \theta \mathbf{E}^{n+1} + (1-\theta)\mathbf{E}^{n}, \tag{14}$$

$$\mathbf{B}^{n+\theta} = \theta \mathbf{B}^{n+1} + (1-\theta)\mathbf{B}^{n}. \tag{15}$$

In the predictor step one needs to calculate $\vec{E}$ and $\vec{B}$ at time level $n+\theta$, and for this purpose we used second Maxwell equation, which gives

$$\mathbf{B}^{n+\theta} = \mathbf{B}^{n} - \theta c \Delta t \nabla \times \mathbf{E}^{n+\theta}. \tag{16}$$

The finite difference approximation for the electric field at time level $n+\theta$ in combination with (16) and the electron velocity equations may be produced by the following way:

$$A\mathbf{E}^{n+\theta} + (\nabla \times \mathbf{E}^{n+\theta}) \times \mathbf{I}$$

$$+ g((\nabla \times (\nabla \times \mathbf{E}^{n+\theta})) \times \mathbf{B}^{n}) = \mathbf{Q}, \tag{17}$$

where

$$d = \theta n_{\mathrm{e}} l_{\mathrm{d}}^{*} \Delta t, \quad A = n_{\mathrm{e}}, \quad g = \frac{\theta \Delta t \epsilon}{M_{\mathrm{A}}^{2}}, \tag{18}$$

$$\mathbf{I} = \frac{\theta\epsilon\Delta t}{M_{\rm A}^2}\left(\frac{M_{\rm A}^2}{\epsilon}\sum_{k=1}^{N_{\rm s}}\mathbf{J}_k^{n+1/2} - \nabla\times\mathbf{B}^n\right), \tag{19}$$

$$\mathbf{Q} = -\left(\sum_{k=1}^{N_{\rm s}}\mathbf{J}_k^{n+\frac{1}{2}} - \frac{\epsilon}{M_{\rm A}^2}\nabla\times\mathbf{B}^n\right)\times\mathbf{B}^n - \frac{\epsilon\beta_{\rm e}}{2M_{\rm A}^2}\nabla p_{\rm e} + n_{\rm e}l_{\rm d}^*\nabla\times\mathbf{B}^n. \tag{20}$$

and

$$\mathbf{U}_{\rm e} = \mathbf{U}_{\rm i} - \epsilon\mathbf{J}/(M_{\rm A}^2 n_{\rm e}). \tag{21}$$

Note that we dropped the electron inertia term in the above finite-difference scheme for the electric field.

In the case with adiabatic electrons one can split the total electric field into the sum of inductive ($\vec{E}_1$) and electrostatic ($\vec{E}_2$) fields:

$$\vec{E} = \vec{E}_1 + \vec{E}_2, \tag{22}$$

where $\vec{E}_2$ satisfies the condition

$$\nabla\times\vec{E}_2 = 0. \tag{23}$$

Then we can solve (17) for component $\vec{E}_1$ neglecting $\nabla p_{\rm e}$. The electrostatic (polarization) electric field $\vec{E}_2$ can be calculated from $p_{\rm e}$ (Lipatov, 2002) because

$$\vec{E_2} = -\frac{1}{en_{\rm e}}\nabla p_{\rm e}. \tag{24}$$

Let us consider two meshes. The first mesh contains the nodes i, j, k, which are located in the center of a cell. It is used for the computation of the density, current, bulk velocity, electron pressure and inductive electric field. The second mesh contains the nodes $i \pm 1/2, j \pm 1/2, k \pm 1/2$, which are located at the corners of a cell. This mesh is used for the computation of the magnetic field components, electrostatic field

and final electric field. Let us assume that $\vec{J}_{\rm i}^{n+1/2}$, $\omega_{\rm pe}$ and $n_{\rm i}$ are known at time level $n+1/2$. Then, expressing $\nabla \times \vec{E}_1^{n+\theta}$ and $\nabla \times (\nabla \times \vec{E}_1^{n+\theta})$ via central finite differences at each cell center, one can obtain the following 3×3 matrix equation:

$$\vec{L} \cdot \vec{E}_{i,j,k}^{n+\theta} = \vec{F}\left(\vec{E}_{i\pm1,j\pm1,k\pm1}^{n+\theta}\right). \tag{25}$$

Equation (25) may be solved by iteration. In each iteration the electric field on the right side is given. The iteration continues until some convergence criterion is satisfied. At the same time the electrostatic field $\vec{E}_2$ is calculated at from Eq. 24.

In the corrector step, when $\vec{E}_2$ is obtain, one can update the magnetic field, using again the second Maxwell equation:

$$\mathbf{B}^{n+1} = \mathbf{B}^n - \frac{c\Delta t}{2}\nabla \times (\mathbf{E}^{n+1} + \mathbf{E}^n). \tag{26}$$

The second term on right side of Eq. 20 keeps a large parameter, so that a strong shot noise in a density computation may cause a strong oscillation in the electric field.

Since the gyroradius must be resolved, a grid point spacing of less than 1 gyroradius is required in order to avoid numerical dispersion and dissipation. On the other hand, good statistics are required, therefore a sufficiently large number of particles per cell have to be used (i.e., to obtain low "shot" noise, which manifests itself as fluctuations in the numerical plasma parameters due to a small number of particles per cell).

A multiscale simulation will be conducted using adaptive mesh and particle refinement techniques with composite grids. This code exploits a splitting-of-particles procedure to keep a low level of "shot" noise on the finer mesh. At the end of the global time step we use the synchronization for the values of the electromagnetic field on coarse

and finer meshes. A.S. Lipatov has developed a version of the Complex Particle Kinetic method (see, Hewett, 2003) [in collaboration with D.W. Hewett (LLNL) and M.R. Combi (Univ. of Michigan)] which allows us a reduction in computational resources by factors of 100 - 1000 in comparison with standard PIC simulation (Lipatov, 2008a). These codes were optimized for parallel computation using MPI and OMP.

One 3D hybrid simulation takes around five months for computing with 24 processors and 64-128 GB RAM on the "shared memory" Columbia SGI system in the NASA Ames Supercomputer Center. Currently, our code operates in the parallel processing with the OpenMP environment. Converting this code to the MPI environment was performed by technical staff members of the Information Technology and Visualization Office (NASA GSFC) starting from Spring 2008 and we are now testing the MPI and OpenMP versions of the code on Pleiades and Discover massively-parallel supercomputers with distributed memory.

3. Results of the Simulation

To study the interaction of solar wind with the SP+ we use the following sets of solar wind plasma parameters: $\beta_{\rm i} = 0.1\,(T_i = 1\,MK)$; $\beta_{\rm e} = 0.1\,(T_e = 1\,MK)$; magnetic field, $B_0 = 1500\,{\rm nT}$; bulk velocity $U_0 = 200\,{\rm km/s}$, density $n_{SW} = 5 \times 10^3\,{\rm cm}^{-3}$, Alfvén Mach number $M_{\rm A} = 1. - 1.5$ and $\theta_{bu} = 11^\circ$. The value of the plasma bulk velocity in the spacecraft frame may vary from $200\,{\rm km/s}$ to $800\,{\rm km/s}$ so we can use a higher Alfvén and sonic Mach numbers in our simulation. Table 2 shows the all parameters that correspond the cases: (a), (b), (c), (d), (d'), (e) and (e'). These parameters correspond

to the values of the motional electric field $E_0 \approx 0.3\,\mathrm{V/m}$ for $r = 9.5R_s$. For the distance from the Sun of about $5R_s$ the value of the magnetic field is of about 6000 nT and the solar wind density is of about $2 \times 10^4\,\mathrm{cm}^{-3}$ (Lipatov, Hartle and Sittler, 2009). We present here the results of simulation for the distance, $r = 9.5R_s$. The time step for electromagnetic field update in the simulation of the quasi-parallel interaction is 48 times smaller than the time step in an oblique case. In the present simulation, the dimensionless scale of proton gyroradius is $\epsilon = \rho_p/L = 10^3$. We discuss the results of 3D hybrid simulations in Sect. 3.1. The results of 2.5D simulation will be discussed in Sect. 3.2. 2.5D simulations include both the particle absorption boundary condition at the heat shield (case d) and the particle reflection boundary condition on the heat shield (case e). We are checking the results of 2.5D simulations in cases (d) and (e) with simulation having smaller grid spacing (case d' and case e') but with the same plasma parameters and boundary conditions.

3.1. Quasi-parallel Interaction of the Solar Wind with Solar Probe Plus. 3D Simulations

In this section we discuss the results of 3D simulations for three cases, namely, case (a): lower number of the macro-particles, $N_p \approx 2.7 \times 10^9$, so there are about 220 macro-particles per cell; (case b): a large number of the macro-particles, $N_p \approx 8 \times 10^9$, so there are about 700 macro-particles per cell with extra-smoothing of the polarization electric field; (case c): same as case (b) except now without extra-smoothing of the polarization electric field. It seems that the larger number of the macro-particles is

not large enough to produce a solution with a low "shot" noise for plasma parameters near $r = 9.5R_S$. Note, that a 'shot" noise is a statistical effect of a fluctuation of the plasma parameters such as bulk velocity, density etc. which results in the fluctuation in the electromagnetic field. These fluctuations in the electromagnetic field produce overheating of the macro-particles. For that reason we use a special smoothing procedure to reduce this noise (case b).

3.1.1. Linear Regime. The results for a long time simulation show the formation of only a small cavity with low plasma density. The reason is the large thermal speed in comparison with the bulk velocity and a strong polarization electric field, $\mathbf{E}_{pol} = -\nabla p_e/en_e$, in cases (a), (b), (c) with $\beta_e = 0.1$. A large polarization electric field can support a strong gradient in the density profile and the result is the formation of a large electric field behind the bus and the heat shield.

Figures 2 and 3 show 2D cuts for proton density in the $y - x$ and $z - x$ planes at $t = 0.014T_{ce}$ ($t = 0.006T_{transit}$), where T_{ce} is the electron gyroperiod and $T_{transit}$ denotes the time for particle transit from the left boundary to the right boundary of the computational domain, (cases a and b). We see the picture of the solar wind flow around the spacecraft. Behind the heat shield a density profile forms a cone due to expansion of the external plasma into the gap between the heat shield and the spacecraft bus. (Present SP+ spacecraft from AO has this region closed off with radiators). Behind the spacecraft bus there is no apparent plasma wake due to low value of the Alfvén Mach number, $M_A = 1.5$, and relatively high plasma beta values, $\beta_p = 0.1$, $\beta_e = 0.1$ (Table 2).

In these simulations the current closure near the spacecraft is very complicated

and is directed by the external magnetic field. Figures 4 - 9 show the 2D cuts for the electric field at $t = 0.014\,T_{ce}$. A linear perturbation occurs in the electric field in the form of whistler/Alfvén waves in upstream and downstream regions at the beginning of the simulation.

In case a, the value of the perturbation in the electric field is about $\delta E \approx (0.02 - 0.6)\,E_0$, for which $E_0 \approx 0.3\,\mathrm{V/m}$ is defined as a standard unit for these computations (see Table 3 for a summary of the electric and magnetic field perturbation amplitudes).

Figures 10 - 15 show 1-D cuts for the electric field profile along the x axis through the point at $y = 0$ and $z = 0$, y axis through the point at $x = 1.5\,L$ and $z = 0$, and z axis through the point at $x = 1.5\,L$ and $y = 0$.

In case a, shown in Fig. 10, far from the spacecraft, the value of perturbation in the electric field component, E_x, is about of $\delta E_x \approx 0.01\,E_0$, whereas $\delta E_y \approx 0.05\,E_0$ and $\delta E_z \approx 0.05\,E_0$, in the x- direction (upstream and downstream). We assume that these waves represent the right-polarized whistler with wavelength $\lambda \approx 2\,\mathrm{m}$. We also observe this type of waves in the downstream region behind the bus.

In y- direction, Fig. 12, the perturbation in the electric field far from spacecraft are the following: $E_x \approx 0.003\,E_0$, $E_y \approx 0.01\,E_0$ and $E_z \approx 0.005\,E_0$.

We also observed the excitation of a high frequency wave that propagates across the magnetic field in the z - direction, Fig. 14, with wavelength $\lambda \approx 0.15\,\mathrm{m}$. The perturbations in the electric field are the following: $E_x \approx 0.04\,E_0$, $E_y \approx 0.05\,E_0$ and $E_z \approx 0.2\,E_0$.

In case a, near the spacecraft the value of perturbation in the electric field components, E_y and E_z, is about $(0.05, 0.15)\,E_0$ (whistler type waves) in the x- direction (upstream and downstream) in Fig. 10; $\delta E_x \approx 0.02\,E_0$, $\delta E_y \approx 0.4\,E_0$ and $\delta E_z \approx 0.1\,E_0$ in the y- direction (Fig. 12); and $\delta E_x \approx 0.06\,E_0$, $\delta E_y \approx 1.0\,E_0$ and $\delta E_z \approx 0.4\,E_0$ in the z- direction (Fig. 14). Near the surface of the spacecraft, the jumps in the electric field, $\delta E_x = (-0.075, -0.15)\,E_0$, $\delta E_y = (-0.075, 0.02)\,E_0$ and $\delta E_z = (-0.12, 0.15)\,E_0$ occur behind the heat shield (Fig. 10). Behind the bus (Fig. 12), the jumps are $\delta E_x = 0.01\,E_0$, $\delta E_y = -0.2\,E_0$, $\delta E_z = -0.025\,E_0$. At the side surface of the bus (Fig. 14), $\delta E_x = (-0.005, 0.025)\,E_0$, $\delta E_y = (-0.1, -0.14)\,E_0$ and $\delta E_z = (-0.07, 0.01)\,E_0$ in the y - direction and $\delta E_x = (-0.02, 0.03)\,E_0$, $\delta E_y = (-0.3, -0.4)\,E_0$ and $\delta E_z = (0.1, -0.175)\,E_0$ were observed in the z - direction.

In Figures 11, 13 and 15 we show electric field for case (b).

Far from the spacecraft, the value of perturbation in the electric field component, E_x, is about of $\delta E_x \approx 0.1\,E_0$, whereas $\delta E_y \approx 0.2\,E_0$ and $\delta E_z \approx 0.3\,E_0$, in the x- direction (upstream). We assume that these waves represent the right-polarized whistler with wavelength $\lambda \approx 0.2\,\mathrm{m}$.

In y- direction, the perturbation in the electric field far from spacecraft are the following: $E_x \approx 0.005\,E_0$, $E_y \approx -0.2\,E_0$ and $E_z \approx 0.01\,E_0$.

In z - direction, the perturbations in the distant electric field are the following: $E_x \approx 0.05\,E_0$, $E_y \approx -0.2\,E_0$ and $E_z \approx 0.02\,E_0$.

Near the spacecraft, Fig. 11, the E_x profile has a jump, $\delta E_x = -0.1\,E_0$ before the heat shield and $\delta E_x = -0.3\,E_0$ before the bus and $\delta E_x = 0.1\,E_0$ behind the bus. Near

the spacecraft we see an excitation of a weak oblique Alfvén (magnetosonic) waves with an amplitude, $\delta E_x \approx \pm 0.05\, E_0$ along y axis (Fig. 13), and $\delta E_x \approx -0.05\, E_0$ along the z axis (Fig.15). The profile of the E_y component has a jumps, $\delta E_y \approx \pm 1\, E_0$ in y direction (Fig. 13) and $\delta E_y \approx 0.4\, E_0$ in z direction, (Fig. 15). The components E_z has a jump, $\delta E_z \approx \pm 0.3\, E_0$ in the y (Fig. 13) and $\delta E_z \approx \pm 1\, E_0$ in the z directions (Fig. 15).

Figures 16 - 21 demonstrate 2D cuts for the magnetic field. At the front of the heat shield a formation of the magnetic field barrier is observed. At the side parts of the computational domain the whistler/Alfvén waves were observed in the $x - z$ plane. The value of the perturbation in the magnetic field component, B_y, is about of $\delta B_y \approx 0.005\, B_0$ ($\approx 7.5\,\mathrm{nT}$ for $B_0 \approx 1500\,\mathrm{nT}$.). The value of the perturbation in the magnetic field B_z is about of $\delta B \approx 0.02\, B_0$.

3.1.2. Regime of Nonlinear Saturation. Let us consider the results of simulations at later times, $t = 0.1\, T_{ce}$ (case a), $t = 0.15\, T_{ce}$ (case b), $t = 0.29\, T_{ce}$ (case c).

Figures 22 - 24 show a 2D cut for proton density in the $y - x$ and $z - x$ planes. The small voids with low plasma density are observed behind the heat shield and the bus. However, the size of these is limited by a strong polarization field. Possibly we need a several times longer simulation.

Figures 25 - 33 show the 2D cuts for the electric field. Since the density distribution had not changed during the simulation and the perturbation in the electromagnetic field reaches the saturation level, we do not find any strong transverse perturbation in the electric fields in the upstream region, but we do see large perturbations in the downstream region.

Figures 34 - 45 show 1-D cuts for the electric field profile along the x axis at the point $y = 0$ and $z = 0$, along the y axis at the point $x = 1.5\,L$ and $z = 0$ and along the z axis at the point $x = 1.5\,L$ and $y = 0$.

In case a, Figs. 34 and 37, the value of these perturbations far from the spacecraft is about of $\delta E \approx (3.0 - 5.0)\,E_0 \approx (7.0 - 10.0)\,\mathrm{V/m}$ in x - direction (upstream). Far from the spacecraft in the downstream region, the value of perturbation in the electric field component, δE_x, is about of $\delta E_x \approx \pm(3.0 - 5.0)\,E_0$ in the x - direction, $\delta E_x \approx \pm(3.0 - 5.0)\,E_0$ in the y - direction (Fig. 40), whereas $\delta E_x \approx \pm(3.0 - 4.0)\,E_0$ in the z- direction (Fig. 43). The value of perturbation in the electric field components, E_y and E_z, is about of $\delta E \approx \pm(3.0 - 5.0)\,E_0$ (whistler type waves) in the x- direction (downstream), Figs. 34 and 37. $\delta E_y \approx \pm(3.0 - 4.0)\,E_0$ in the y- direction (Fig. 40), and $\delta E_y \approx \pm 2.0\,E_0$ in the z- direction, Fig. 43. The value of perturbation in the electric field component, E_z, is about of $\delta E_z \approx \pm(3.0 - 5.0)\,E_0$ in the y- direction, Fig. 40, and $\delta E_z \approx \pm(3.0 - 5.0)\,E_0$ in the z- direction, Fig. 43. Near the spacecraft, Fig. 43, the E_x profile has a jump, $\delta E_x = -250\,E_0$ behind the cylindrical section (conducting bus). We also see a jump in E_y component of the electric field, $\delta E_y \approx \pm 55.0\,E_0$ in y direction (Fig. 40) and $\delta E_y \approx (7.0 - 8.0)\,E_0$ in z direction. The component E_z has a jump, $\delta E_z \approx (-60.0, -400.0)\,E_0$ in x direction (Fig. 34), $\delta E_z \approx (4.0, -6.0)\,E_0$ in y direction (Fig. 40) and $\delta E_z \approx \pm 60.0\,E_0$ z direction (Fig. 43).

In case b, far from the spacecraft, the value of perturbation in the electric field component, E_x, is about of $\delta E_x \approx (1.0, 0.5)\,E_0$ in the x- direction (upstream and downstream), Figs. 35, 38, whereas $\delta E_x \approx \pm 0.5\,E_0$ in the y- direction, Fig. 41, and

$\delta E_x \approx (1.0, 0.5)\, E_0$ in z - direction, Fig. 44. The value of variation in the electric field components, E_y and E_z, is about of $\pm 0.5\, E_0$ in x, y and z (upstream), Fig. 38. Downstream, the value of the perturbations in E_y and E_z are about of $\delta E \approx 2.0\, E_0$ in x - direction, Fig. 38.

Near spacecraft, Fig. 35, the E_x profile has a jump, $\delta E_x \approx -190\, E_0$ in x - direction behind the heat shield and the bus, and $\delta E_x \approx (0.5 - 1.5)\, E_0$ along y (Fig. 41) and z - axes (Fig. 44). We also see a jump in E_y component of the electric field, $\delta E_y \approx 100\, E_0$ in x - direction behind the bus (Fig. 35), $\delta E_y \approx \pm 40\, E_0$ in y - direction (Fig. 41) and $\delta E_y \approx (6.0, 7.0)\, E_0$ in z - direction (Fig. 44). The component E_z has jumps, $\delta E \approx -160\, E_0$ in x - direction (Fig. 35), $\delta E_z \approx -(5.0, 6.0)\, E_0$ in y (Fig. 41), and $\delta E_z \approx \pm 40\, E_0$ and z - directions (Fig. 44).

In case c, far from the spacecraft, the value of perturbation in the electric field component, E_x, is about of $\delta E_x \approx \pm 2.0\, E_0$ in the x - direction (upstream and downstream), Fig. 39. Similar oscillations occur for cuts along y - direction (Fig. 42) and z - direction (Fig. 45). The value of perturbation in the electric field components, E_y, is about of $\delta E_y \approx \pm 2.0\, E_0$ (whistler/Alfvén waves) in the x- direction (upstream and downstream), y, and z- directions, Figs. 39, 42 and 45, respectively. The value of perturbation in the electric field component, E_z, is about of $\delta E_z \approx \pm 2.0\, E_0$ in the x, y and z - directions, Figs. 39, 42 and 45. Near spacecraft, Fig. 36, the E_x profile has a jump, $\delta E_x \approx -230\, E_0$ in x - direction behind the heat shield and the bus. Near spacecraft we see an excitation of a strong Alfvén waves with an amplitude, $\delta E_x \approx (2.0, -3.0)\, E_0$ along y - axis (Fig. 42), and $\delta E_x \approx (-1.0, -2.0)\, E_0$ along the z -

axis (Fig. 45). We also see a jump in E_y component of the electric field, $\delta E_y \approx -250\, E_0$ in x - direction behind the bus and $\delta E_y \approx \pm 40.0\, E_0$ in y - direction and $\delta E_y \approx 4.0\, E_0$ in z - direction, Figs. 39, 42 and 45, respectively. The component E_z has jumps, $\delta E \approx -100.0\, E_0$ in x - direction behind the bus (Fig. 36), $\delta E \approx -4.0\, E_0$ in y - direction (Fig. 42), and $\delta E \approx \pm 35.0\, E_0$ in z - direction (Fig. 45). As before, the above figures demonstrate a strong oscillation in the electric field. We deducted the polarization electric field from the total electric field and we found the regular current closure that corresponds the Alfvén wing.

The above figures demonstrate a strong oscillation in the electric field. We also deducted in case (a) the polarization electric field from the total electric field and we found the regular current closure that corresponds the Alfvén wing. If we assume the "shot" noise $\delta n/n = 0.07$ then a fluctuation in the polarization electric field may be estimated as $\delta E_{pol} = -\nabla p_e/en_e \approx 2 \times 10^2 E_0$. The nature of the "shot" noise is a statistical fluctuation of the particle velocity distribution in cell due to a limited number of the macro-particles per cell (see e.g., Birdsall, Langdon and Okuda, 1970). This value represents the upper limit for the polarization electric field, however, the level of electric field fluctuations is much lower because we use a "quiet start" in our simulation i.e. we started from a plasma distribution without any fluctuation in the density and current. In case (b) the "shot" noise in density is estimated as $\delta n/n = 0.04$, then a fluctuation in the polarization electric field may be estimated as $\delta E_{pol} = -\nabla p_e/en_e \approx 10^2\, E_0$. And, finally, in case (c) the estimation of the "shot" noise gives the same value in the polarization electric field as in case (b).

Figures 46 - 54 demonstrate 2D cuts for the magnetic field. In case (a), we do not find any magnetic field barrier near the heat shield. At the side parts of the computational domain, compression waves occur in the simulations. The value of perturbation in the magnetic field is about of $\delta B \approx 0.02\, B_0$. In case (b), at the front of the heat shield a formation of the magnetic field barrier or build up was observed. The formation of the Alfvén wing was also observed. The value of perturbation in the magnetic field is about of $\delta B \approx (0.004, 0.03)\, B_0$. In case (c), at the front of the heat shield a formation of the magnetic field barrier or build up was observed. At the side parts of the computational domain, compression waves were observed in simulations. The value of perturbation in the magnetic field is about of $\delta B \approx 0.02\, B_0$.

Summary 1. 3D hybrid simulations show the following global plasma dynamics near the SP+ spacecraft. The heat shield and bus generate a pulse of the transverse waves. The lead front of the pulse represents a whistler-like wave in upstream and downstream directions.

At later time the lead front of the electromagnetic pulse intersects the boundary of the computational domain, and the low-frequency Alfvén waves, which are directed by the external magnetic field, were observed near the spacecraft. The excitation of these waves are accompanied by the formation of the double current closure attached to the heat shield. The maximum value of the perturbations is located between the double currents.

The amplitude of these waves are about of $0.05\, E_0$ at the linear stage and $(1-5)\, E_0$ at the saturation stage.

These waves were generated by the gradients in plasma parameters and the Hall term plays the key role to support these waves. Note that such type of waves was also observed near a tether system moving across the magnetic field in the ionosphere, in the plasma environment of small moons (e.g. Io - Alfvén wing), near plasma clouds moving across the magnetic field.

Near the bus, the jumps in the normal component of the electric field (polarization field) have approximately the same value in all cases: (a) $E_x = 250\,E_0$, $E_y = 50\,E_0$, $E_z = 60\,E_0$; (b) $E_x = 200\,E_0$, $E_y = 60\,E_0$, $E_z = 40\,E_0$; (c) $E_x = 250\,E_0$, $E_y = 40\,E_0$, $E_z = 40\,E_0$, respectively. The tangential components of the electric field near the spacecraft evolve in time and their values may be different in these regimes. Note that the results of simulation at the saturation stage correspond to the different moments of time for cases (a), (b) and (c). The observed strong wave amplitudes upstream and downstream the SPP do not occur in the 3D hybrid simulation with a lower value of the $\beta_e = 0.000125$ and $\beta_e = 0.00125$ (see Lipatov, Sittler and Hartle, 2009). That fact allows us to make a conclusion that the growth of these waves is controlled by electron temperature and we need a further study of the mechanism of an excitation of these waves.

3.2. Parallel Interaction of the Solar Wind with Solar Probe Plus. 2.5D simulations

3.2.1. Parallel Interaction of the Solar Wind with Solar Probe Plus. 2.5D simulation with large grid spacing.

Since a 3D hybrid simulation of the

Solar Probe Plus spacecraft's environment is very costly we have also performed a set of 2.5D simulations. The simulation of the oblique and quasi- parallel interaction shows the unphysical growth of the magnetic field barrier since the magnetic field line cannot penetrate though the cylindrical obstacle. Here we discuss the results of 2.5D simulations with the particle absorption boundary condition (case d) and the particle reflection boundary condition on the heat shield (case e).

We are also checking the results in case (d) and (e) with simulation using smaller grid spacing (case d' and case e'). Here we present only the cases with a parallel interaction, $\theta = 0°$. We use 880×10^6 macro-particles and a mesh with 401×601 grid points so that we have 3675 particles per cell in our 2.5D simulation.

The simulation with reduced 2.5D configuration shows formation of an extended plasma wake at much longer time interval. Let us consider now the simulation results with $\beta_e = 0.1$ at time, $t = 2.2\,T_{ce}$ ($t = 0.26\,T_{transit}$), where $T_{transit}$ is the time for particle transit from the left boundary to the right boundary of the computational domain. Figure 55 shows a proton density in the $y - x$ plane in cases d (top, particle absorption boundary condition) and e (bottom, particle reflection boundary condition on the heat shield). We see the formation of the large void behind the heat shield and the bus. In case e, we also see a formation of a higher plasma density region at the front of the heat shield. The value of the density in this case, Fig.55 (bottom) may exceed by factor of 2 the value of the density in upstream in case d, Fig. 55 (top). The perturbation in the electromagnetic field reaches the saturation level, since the density distribution has not changed during the simulation.

Figures 56, 57 and 58 show the distributions for the electric field at $t = 2.2\,T_{ce}$. As before, the perturbations in the electromagnetic field reached the saturation levels.

The electric field upstream is calculated by the use of the simplified generalized Ohm'law

$$\mathbf{E} = -\frac{1}{en_{\rm e}c}(\mathbf{J}_{\rm i} \times \mathbf{B}) + \frac{1}{en_{\rm e}c}(\mathbf{J} \times \mathbf{B}), \tag{27}$$

where we dropped the ∇P_e term because there are no strong perturbations in the plasma density upstream. Since the simulation does not show any perturbations in bulk velocity upstream we can conclude that the perturbations in the electric field E_y and E_z have a whistler-like type and these perturbations with $E_y \neq E_z$ are due to the second term in the right side of Eq. 27 (Hall term).

Figures 59, 60 and 61 shows 1-D cuts for the electric field profile along the x and y axes through the point $y = 0$ and $x = 1.5$, respectively.

In case d, far from the spacecraft, the values of perturbation in the electric field components, E_x, E_y and E_z are about of $\delta E_x \approx \delta E_y \approx \pm 2.0\,E_0$ and $\delta E_z \approx 0.1\,E_0$ in the x- direction (upstream and downstream). The values of perturbation in the electric field components, E_x, E_y and E_z, are about of $\delta E_x \approx \delta E_y \approx \pm(1.0 - 2.0)\,E_0$ (oblique whistler/Alfvén waves or "shot noise") in the y- direction, and $\delta E_z \approx 0.02\,E_0$ in the y-direction.

In case d, near spacecraft, the E_x profile has a jump, $\delta E_x \approx (+14.0, -33.0)\,E_0$ in *thex* - direction behind the heat shield and the bus, respectively. We also see a jump in E_y component of the electric field, $\delta E_y \approx (+15.0, -38.0)\,E_0$ in x - direction behind the

bus and $\delta E_y \approx \pm 55.0\, E_0$ in y - direction, also near bottom of bus. The component E_z has jumps, $\delta E_z \approx (-0.4, 0.3)\, E_0$ in the x - direction, and $\delta E_z \approx -(0.4, 0.05)\, E_0$ in the y - direction, Figs. 60 and 61, respectively.

In case e, far from the spacecraft, the values of perturbation in the electric field components, E_x, E_y and E_z are about of $\delta E_x \approx \delta E_y \approx \pm 2.0\, E_0$ and $\delta E_z \approx (0.1 - 0.3)\, E_0$ (oblique whistler/Alfvén waves or "shot noise") in the x- direction (upstream and downstream), Fig. 60. The values of perturbation in the electric field components, E_x, E_y and E_z, are about of $\delta E_x \approx \delta E_y \approx \pm 1.0\, E_0$ (oblique whistler/Alfvén waves or "shot noise") in the y- direction and $\delta E_z \approx 0.3\, E_0$ in the y- direction.

In case e, near the spacecraft, the E_x profile has a jump, $\delta E_x \approx 500.0\, E_0$ and $\delta E_x \approx -20.0\, E_0$ in x - direction at the front of the heat shield and behind the bus. We also see a jump in the E_y component of the electric field, $\delta E_y \approx 10.0\, E_0$ in the x - direction behind the bus and $\delta E_y \approx 60.0\, E_0$ in the y - direction. The component E_z has jumps, $\delta E_z \approx -1.0\, E_0$ in the x - direction, and $\delta E_z \approx \pm 0.5\, E_0$ in the y - direction, Figs. 60 and 61.

The above figures demonstrate a strong oscillation in the electric field. If we assume the "shot" noise $\delta n/n = 0.016$ then a fluctuation in the polarization electric field may be estimated as $\delta E_{pol} = -\nabla p_e / e n_e \approx 40\, E_0$. This value represents the upper limit for the polarization electric field.

Figures 62, 63 and 64 demonstrate distributions for the magnetic field. At the front of the heat shield a formation of the magnetic field barrier or build up was observed. At the side parts of the computational domain, compression waves were

observed in simulations. The value of the perturbation in the magnetic field is about of $\delta B \approx 0.02\, B_0$.

3.2.2. Parallel Interaction of the Solar Wind with Solar Probe Plus.

2.5D simulation with smaller grid spacing. In order to check the results of simulation we have repeated the simulation with a 2x smaller computational domain and a 2x smaller grid cell size. Let us consider now the result of simulation with $\beta_e = 0.1$ at time, $t = 1.0\, T_{ce}$ ($t = 0.12\, T_{transit}$), where $T_{transit}$ is the time for particle transit from the left boundary to the right boundary of the computational domain. Figure 65 shows a proton density in the $y - x$ plane in cases d' (top, particle absorption boundary condition) and e' (bottom, particle reflection boundary condition on the heat shield).

We see the formation of the large void behind the heat shield and the bus. As in case e, we see the formation of high density region at the front of the heat shield, Fig. 65 (case e', bottom).

The perturbation in the electromagnetic field reaches the saturation level, since the density distribution has not changed during the simulation.

Figures 66, 67, and 68 show the distributions for the electric field at $t = 1.0\, T_{ce}$. Since the density distribution had not changed during the simulation the perturbation in the electromagnetic field reached the saturation levels. Figures 69, 70 and 71 shows 1-D cuts for the electric field profile along the x and y axes through the point $y = 0$ and $x = 1.5\, L$, respectively.

In case d', far from the spacecraft, the values of perturbation in the electric field components, E_x, E_y and E_z, are about of $\delta E_x \approx \delta E_y \approx \pm(2.0 - 3.0)\, E_0$

(whistler/Alfvén waves or "shot noise") in the x- direction (upstream and downstream), and $\delta E_z \approx \pm(0.1 - 0.5)\, E_0$ in the x- direction. The values of perturbation in the electric field components, E_x, E_y and E_z, are about of $\delta E_x \approx \delta E_y \approx \pm(2.0 - 3.0)\, E_0$ and $\delta E_z \approx \pm 0.05\, E_0$ in the y- direction.

In case d', near spacecraft, the E_x profile has a jump, $\delta E_x \approx 80.0\, E_0$ and $\delta E_x \approx -15.0\, E_0$ in x - direction at the front of the heat shield and behind the bus, respectively. We also see a jump in E_y component of the electric field, $\delta E_y \approx 2.0\, E_0$ in x - direction behind the bus and $\delta E_y \approx 100.0\, E_0$ in y - direction, also behind the bus. The component E_z has jumps, $\delta E_z \approx \pm 2.5\, E_0$ in x - direction in the plasma wake, and $\delta E_z \approx \pm 0.25\, E_0$ in y - direction, Figs. 70, 71.

In case e', far from the spacecraft, the values of perturbation in the electric field components, E_x, E_y and E_z are about of $\delta E_x \approx \delta E_y \approx \pm(2.0 - 3.0)\, E_0$ (whistler/Alfvén waves or "shot noise") in the x- direction (upstream and downstream), and $\delta E_z \approx \pm 0.01\, E_0$ in the x- direction. The values of perturbation in the electric field components, E_x, E_y and E_z, are about of $\delta E_x \approx \delta E_y \approx \pm(2.0 - 3.0)\, E_0$ and $\delta E_z \approx \pm 0.1\, E_0$ in the y- direction.

In case e', near spacecraft, the E_x profile has a jump, $\delta E_x \approx 150.0\, E_0$ and $\delta E_x \approx -20.0\, E_0$ in x - direction at the front of the heat shield and behind the bus, respectively. While, $\delta E_x \approx \pm 20.0\, E_0$ in y - direction. We also see a jump in E_y component of the electric field, $\delta E_y \approx 1.0\, E_0$ in x - direction behind the bus and $\delta E_y \approx \pm 100.0\, E_0$ in y - direction also behind the bus. The component E_z has jumps, $\delta E_z \approx 0.04\, E_0$ in x - direction, and $\delta E_z \approx (-5.0, 1.5)\, E_0$ in y - direction, Figs. 70, 71.

The above figures demonstrate a strong oscillation in the electric field. If we assume the "shot" noise $\delta n/n = 0.016$ then a fluctuation in the polarization electric field may be estimated as $\delta E_{pol} = -\nabla p_e/en_e \approx 40\, E_0$. This value represents the upper limit for the polarization electric field.

Figures 72, 73 and 74 demonstrate the distributions for the magnetic field. At the front of the heat shield a formation of the magnetic field barrier or build up was observed. At the side parts of the computational domain, compression waves were observed in simulations. The value of perturbation in the magnetic field is about of $\delta B \approx 0.02\, B_0$.

Unfortunately, 2.5D simulation was limited by the parallel interaction case. The simulation of the quasi-parallel and oblique interactions show the formation of the non-physical magnetic barrier since the magnetic filed lines cannot move through the cylindrical obstacle.

Summary 2. 3D and 2.5D hybrid simulations well enough describe the global plasma dynamics near the SP+ spacecraft. In 3D simulation the heat shield and bus generate as pulse of the transverse waves. The lead front of the pulse represents a whistler-like waves in upstream and downstream. In 2.5D simulations shows the compression-like perturbations in E field, possible associated with "shot" noise. The parallel 2.5D simulation does not demonstrate any two-current system upstream of the heat shield in case of the parallel interaction when the angle between the bulk velocity and the background magnetic field, θ_{U_0,B_0} equals zero.

Table 3 accumulates the results of the simulations presented in this Report. Let

us compare the level of fluctuations in the E-field in 3D and 2.5D simulations. As was indicated on page 24 and page 28 the maximum level of fluctuations in the E-field due to "shot" noise effects are $200\,U_0 \times B_0$ in 3D simulations (case a), $100\,U_0 \times B_0$ (cases b and c), $40\,U_0 \times B_0$ in 2.5D simulations for the SW parameters at $9.5\,R_s$.

The relatively short 3D simulations produce the following oscillations in the E-field: $\delta E \approx 5\,E_0$ (case a); $(0.5\text{-}1.0)\,E_0$ (case b); $2.0\,E_0$ (case c), depending on the smoothing procedures in the E_{pol} field or N_p. In the 2.5D much longer simulations the limit for fluctuations in the E-field due to a "shot" noise is about of $40\,U_0 \times B_0$. Fortunately, the fluctuations in the E-field in our relatively short 2.5D simulations are about of $(2-4)\,E_0$ (Figs. 60, 61, 70 and 71.

So, the single way to reduce these fluctuations is to increase the number of macro-particles. We also need to study the convergence of our hybrid algorithm to the analytical solution in case of a strong "shot" noise. Possibly, we have to repeat our computations with the use the advection equation applied directly to magnetic induction field. The scheme's viscosity may to suppress spurious oscillations, probably caused by a "shot" noise" (see e.g. Lipatov, 2002). Note, that spurious oscillations may occur because our numerical model includes the second order approximation in space, whereas the convective term in the induction equation was presented by the first order derivative. This inconsistency may result in a spurious oscillation occurrence.

The jump in the polarization field (2.5D simulations), E_{pol} near the surface of SPP is very strong and it value does not connect with "shot" noise (Figs. 60, 61, 70 and 71.

Note, that there is also possibility for an excitation of the plasma wave ($\omega \approx \omega_{pe}$)

in the regions of the plasma wake with a low ion density, however, the study of these effects needs full kinetic model.

4. Conclusions and possible future simulations

3D hybrid simulations of the interaction of the solar wind plasma with Solar Probe Plus at the distance $r = 9.5\, R_S$, have demonstrated several new features:

- In the quasi-parallel case the current closure near a spacecraft is very complicated and is directed by the external magnetic field. At the front of the heat shield the magnetic field barrier forms, whereas strong whistler/Alfvén waves occur in both upstream and downstream regions. At the side parts of the computational domain, compression waves are found. The values of the electric field oscillation near the spacecraft bus may be the same order as the maximum of expected electric field (d.c.) in an antenna (see, Table 1 from Murphy et al, 2008).

- 3D hybrid simulations do not demonstrate the formation of the extended plasma void wake near the SP+ spacecraft, due to short time simulation (5 months), and also due to the strong polarization electric field and a large thermal ion speed compared with the bulk velocity.

- For absorption boundary conditions we do not observe any perturbations in the plasma density upstream the SP+.

- Now it is possible to use more than 1024 processors on "SGI-Columbia", "SGI-Pleiades" (NASA Ames Center) and "Linux cluster Discover" (NASA

GSFC) parallel computer systems with hybrid MPI/OpenMP environment to achieve improved scalability for longer computations.

- Simulated electric field perturbations are comparable to or exceed the maximum electric field expected for the SP+ spacecraft. Therefore, a wake deployment of an electric field plasma-wave antenna may not be a viable option for SP+.

2.5D hybrid simulations of the interaction of the solar wind plasma with Solar Probe Plus at the distance $r = 9.5\,R_S$, have demonstrated several following features:

- 2.5D simulations show the formation of the extended plasma wake with a small density cavern around the spacecraft. The large spatial wake results in the reduction in the polarization field near the spacecraft and behind the spacecraft bus.

- 2.5D simulations with a particle reflection boundary condition at the heat shield show the formation of the enhanced density in the external region of the plasma wake. Upstream of the SP+, the plasma velocity distribution may change a lot due to possible two-stream (beam-beam) instability.

Future work that is still needed:

Hybrid simulations

- Simulations with low value of Mach number and various boundary conditions on the spacecraft bus and trusses configuration; in, particular, simulations with

reflected boundary condition for particle at the surface of the spacecraft in order to take into account the effect of the spacecraft charging.

- Simulation with much higher space resolution and a number of macro-particles to reduce a "shot" noise in density and polarization electric field;

- 2.5D simulations with direct numerical time integration of the equation for magnetic field (numerical scheme for advection equation with an alternative direction implicit (ADI) method). Such type of scheme was used for 2.5 simulation by Lipatov for the study of the interaction plasma flow with a comet, Venus etc (see e.g., Lipatov 2002). It may possibly help us to reduce the short wavelength electromagnetic oscillation by the scheme resistivity. Currently, we use an implicit time integration scheme suggested in 1992 (limited number copies of preprint from the LLNL) (see e.g., Anderson and Shumaker, 1995 and further modifications in Lipatov, 2002). Another possibility is to use the full kinetic code that provides the absorption of the whistler-like wave by the wave-electrons interactions.

- Simulations with using the (implicit or semi-implicit) equation for the time evolution of the electron pressure. This way may result to reduction of the oscillations in the electric field.

- 2.5D simulations with fine spatial resolution to confirm the results produced in 3D simulations.

- 3D hybrid long time simulation with fine resolution and the best boundary

conditions that minimize electromagnetic perturbations near the spacecraft bus.

The results of these simulations will be included in future publications.

Full kinetic simulations

- Simulations with a test-particle approximation for electrons while the electromagnetic fields will be taken from 3D hybrid simulations. Such computations will provide electron dynamics near the spacecraft, and provide estimates of the particle flux (velocity distribution) at the surface of the spacecraft.

- Simulation that will take into account the charging of the spacecraft, charge separation effects, outgassing from the heat shield, and effects due to photoionization and electron impact ionization effects near the spacecraft.

Hall-MHD or two-fluid simulations

- Hall-MHD or two-fluid simulations. These models have no any "shot" noise effects and may produce a perfect current closure and the low-frequency wave system near the SPP.

- Two-fluid models (separate fluid approximation for ions and electrons) may help us to study the low- and high-frequency plasma oscillations inside the plasma wake in the regions with a low value of the density.

Acknowledgments.

E.C. Sittler and A.S. Lipatov were supported in part by grant of the NASA' Grant N 93672302010619 (PI - E.C. Sittler) through NASA GSFC and GEST Center UMBC,

respectively. Computational resources were provided by the NASA's High-End Computing Centers at NASA Goddard (SGI shared memory parallel system "Palm/Explore") and Ames (SGI shared memory parallel system "Columbia") Centers through the NASA Computational Grants SMD-07-0458 and SMD-08-0636.

References

Alpert, Ya.L., Waves and satellites in the near-earth plasma. Studies in Soviet space. (Translated from Russian by J.B. Barbour), Consultants Burea, New York, pp. 205 (1974).

Anderson, D.V., and Shumaker, D.E. Hybrid Ordered Particle Simulation (HOPS) code for plasma modelling on vector-serial, vector-parallel, and massively parallel computers. Comput. Phys. Comm. 87(1-2), 16-34 (1995).

Bale, S.D., C.J. Owen, J.I. Bougret, K. Goetz et al., *Geophys. Res. Lett.*, **24**, 1427 (1997).

Birdsall, C.K., A.B. Langdon, H. Okuda, Finite-Size Particle Physics Applied to Plasma Simulation. In: *Methods in Computational Physics. Plasma Physics, Vol. 9*, ed. by B. Alder, S. Fernbach, M. Rotenberg (Academic Press, New York and London 1970) p. 241

Braginskii, S.L., Transport processes in a plasma. In: Leontovich, M.A. (Ed.), Reviews of Plasma Physics. Consultants Bur., New York, p. 205 (1965).

Chang, C.L., A.S. Lipatov, A.T. Drobot, K. Papadopoulos, P. Satya-Narayana, Hybrid simulation of whistler waves generation and current closure by a tether in the ionosphere, *Geophys. Res. Lett.*, 21, 1015 (1994).

Damiano, P.A., R.D. Sydora, J.C. Samson, Hybrid magnetohydrodynamic-kinetic model of standing shear Alfvén waves, *J. Plasma Physics*, **69**(4), 277-344 (2003).

Hewett, D., Fragmentation, merging, and internal dynamics for PIC simulation with finite size particles, J. Comput. Phys., **189**, 390-426 (2003).

Hewett, D.W. and A.B. Langdon, Electromagnetic Direct Implicit Plasma Simulation, *J. Comput. Phys.*, **72**, 121 (1987).

Lipatov, A.S., *About the three-dimensional structure of the lunar wake. Cosmic Res.* **14**, 103 (1976).

Lipatov, A.S., *The Hybrid Multiscale Simulation Technology. An Introduction with Application to Astrophysical and Laboratory Plasmas*, Springer-Verlag, Berlin, Heidelberg, New York, pp. 1-403 (2002).

Lipatov A.S., V.A. Lobachev, Numerical Kinetic Simulation of the One-dimensional Structure of Oblique and Quasi-Perpendicular Collisionless Shocks, *Cosmic Res. (Sov. J. Kosmich. Issledov.)*, **34**(5), 420 (1996).

Lipatov, A.S., U. Motschmann, T. Bagdonat, and J.-M. Grießmeier, The interaction of the stellar wind with an extrasolar planet – 3D hybrid and drift-kinetic simulations, *Planet. Space Sci* **53**, 423-432 (2005).

Lipatov, A.S., Merging for complex particle kinetic modeling of the multiple plasma beams (inter-penetrating flows), *J. Comput. Phys.* (to be submitted) (2008a).

Lipatov, A.S., R. Rankin, Electron acceleration by th Alfvén wave pulses: 2.5D hybrid modeling, *Physics of Plasma*, (to be submitted, 2008b).

Mankofsky, A., Sudan, R.N., and Denavit, J., Hybrid Simulation of Ion Beams in Background Plasma. J. Comput. Phys. 70, 89-116 (1987).

Marconi, M.L., Dagum, L. and Smyth, W.H., Hybrid fluid/kinetic approach to planetary atmospheres: An example of an intermediate-mass body. Astrophys. J. 469, 393-401 (1996).

Murphy, N., et al., Thermal Design Consideration for the Solar Probe Electric Field Antenna, Feb. 2008.

Neugebauer, M., *Phys. Rev. Lett.*, **4**(1), 6 (1960).

Neubauer, F.M., Nonlinear standing Alfvén wave current system at Io–Theory, *J. Geophys. Res.*, 85, 1171-1178 (1980)

Van'yan, L.L., A.S. Lipatov, Three-dimensional hydromagnetic disturbances generated by a magnetic dipole in an anisotropic plasma, *Geomagn. Aeronomy*, 12(2), 316-318 (1972)

Wang, Y.C., Theoretical study of the magnetic field in the lunar wake, *Phys. Fluids* **11**(8), 1713 (1968)

Wang, Y.C., Field and plasma in the lunar wake, *Phys. Rev.* **186**(1), 143 (1969)

Wang, Y.C., N.F. Ness, *J. Geophys. Res.* **75**(31), 6002 (1970)

Received _____

Table 1. Important values of the electromagnetic field in an antenna from "Thermal Design Consideration for the Solar Probe Electric Field Antenna by Murphy et al., Feb. 2008".

	$4R_s$	$12R_s$	$20R_s$
$U \times B$	$12\,\mathrm{V/m}$	$2.5\,\mathrm{V/m}$	$0.5\,\mathrm{V/m}$
E_{max}, DC	$1\,\mathrm{V/m}$	$0.1\,\mathrm{V/m}$	$0.1\,\mathrm{V/m}$
E_{max}, 100kHz	$10^{-3}\,\mathrm{V/m\,Hz^{-1/4}}$	$10^{-4}\,\mathrm{V/m\,Hz^{-1/4}}$	$10^{-4}\,\mathrm{V/m\,Hz^{-1/4}}$
V Noise at 100 kHz	$10^{-6}\,\mathrm{V/Hz^{-1/4}}$	$3 \times 10^{-7}\,\mathrm{V/Hz^{-1/4}}$	$2 \times 10^{-7}\,\mathrm{V/Hz^{-1/4}}$

Table 2. Solar Wind Parameters for Modeling.

Case	U_0	n_{SW}	B_0	θ_{bu}	M_A	β_p	β_e	$U_0 \times B_0$	N_p per cell	Comments
a	200 km/s	5×10^3	1500 nT	11°	1.5	0.1	0.1	0.3 V/m	75	no smoothing in E_{pol}
b	200 km/s	5×10^3	1500 nT	11°	1.5	0.1	0.1	0.3 V/m	800	smoothing in E_{pol}
c	200 km/s	5×10^3	1500 nT	11°	1.5	0.1	0.1	0.3 V/m	800	no smoothing in E_{pol}
d	200 km/s	5×10^3	1500 nT	0°	1.5	0.1	0.1	0.3 V/m	800	2.5D, with absorption
d'	200 km/s	5×10^3	1500 nT	0°	1.5	0.1	0.1	0.3 V/m	800	2.5D, with absorption; higher spatial resolution
e	200 km/s	5×10^3	1500 nT	0°	1.5	0.1	0.1	0.3 V/m	800	2.5D with reflection
e'	200 km/s	5×10^3	1500 nT	0°	1.5	0.1	0.1	0.3 V/m	800	2.5D with reflection; higher spatial resolution

Table 3. Electromagnetic Field Perturbation in Plasma Environment near SP^+, $\delta E(0.3\,\mathrm{V/m})$, $\delta B(1500\,\mathrm{nT})$.

Case	$t(T_{ce})$	δE_x	δE_y	δE_z	δB_x	δB_y	δB_z	E_n at bus
a	0.014	0.02-0.15	0.03-0.1	0.02-0.1	0.001	0.0002	0.001	0.01-0.1
a	0.29	5.0	5.0	5.0	0.005	0.01	0.1	60-250
b	0.014	0.2	0.2	0.2	0.002	0.005	0.02	0.4-1.0
b	0.15	0.5-1.0	0.5-1.0	0.5-1.0	0.005	0.01	0.1	40-200
c	0.29	2.0	2.0	2.0	0.005	0.01	0.1	35-250
d	2.2	1.0-2.0	1.0-2.0	0.1	0.02	0.02	0.005	30-60
d'	2.2	2.0-3.0	2.0-3.0	0.1	0.02	0.02	0.005	30-60
e	2.2	1.0-2.0	1.0-2.0	0.3	0.02	0.02	0.005	30-60
e'	2.2	2.0-3.0	2.0-3.0	0.3	0.02	0.02	0.005	30-60

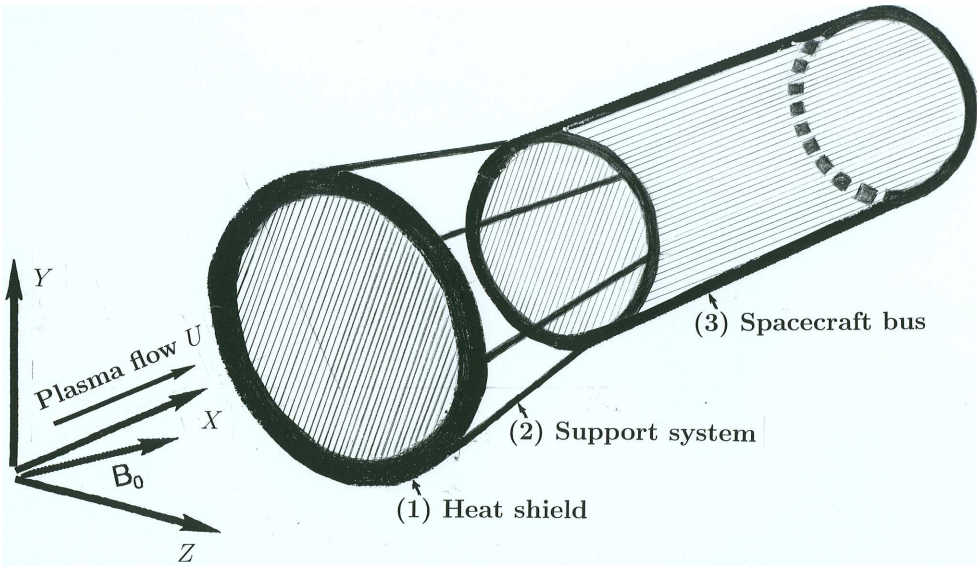

Figure 1. Scheme of the interaction of the solar wind with SP+. The spiral magnetic field is inside the x-z plane. (1) a heat shield; (2) a support system; (3) a spacecraft bus.

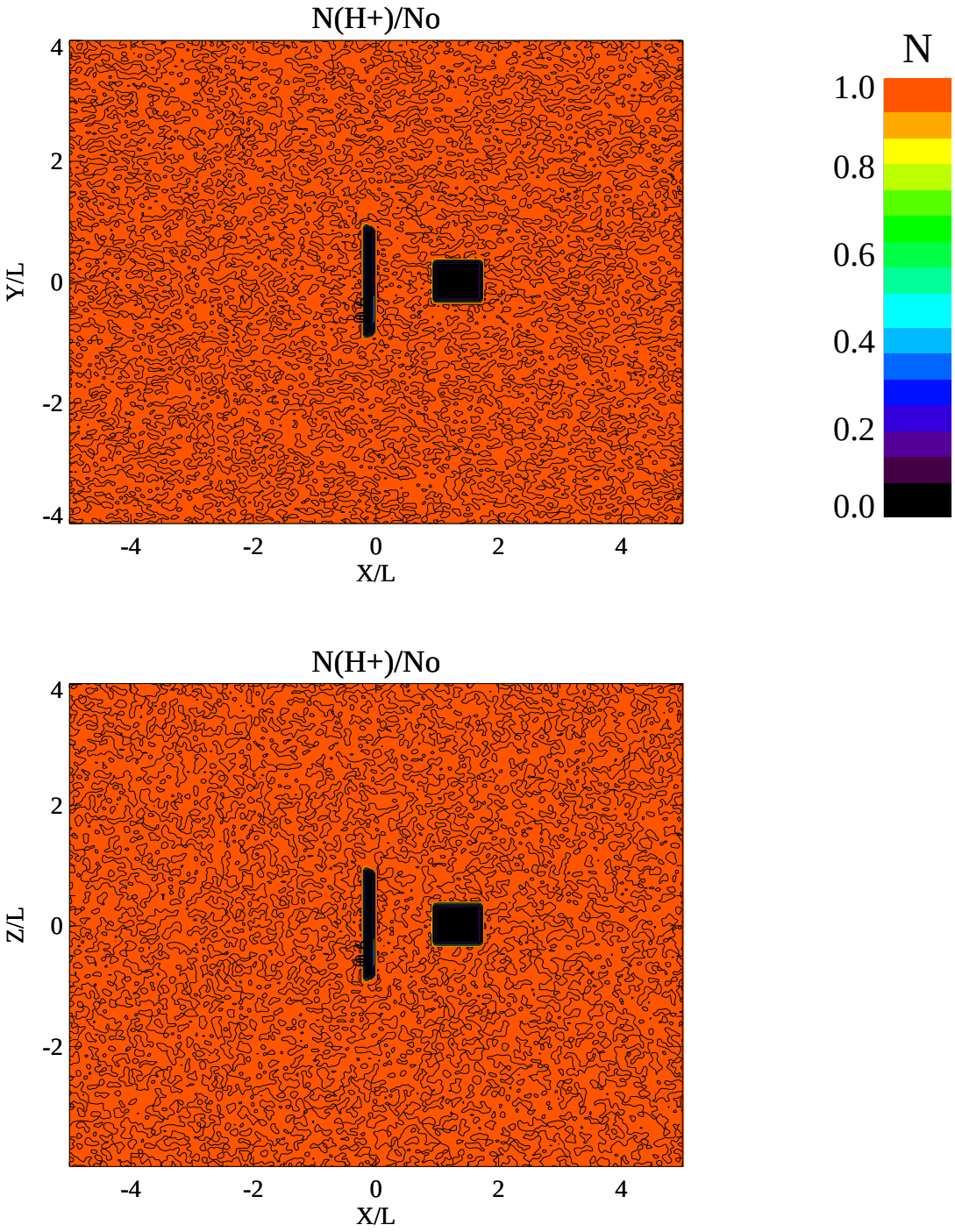

Figure 2. Solar wind ion density in the y-x ($z = 0$) and z-x ($y = 0$) planes. $U_0 = 200\,\mathrm{km/s}$, $M_A = 1.5$, $B_0 = 1500\,\mathrm{nT}$, $E_0 = U_0 B_0 = 0.3\,\mathrm{V/m}$, $n_{SW} = 5 \times 10^3\,\mathrm{cm}^{-3}$, $\beta_\mathrm{p} = 0.1$, $\beta_\mathrm{e} = 0.1$, $\theta_{bu} = 11^o$. Linear perturbations occur at the beginning of simulation, at $t = 0.014\,T_{ce}$, (case a).

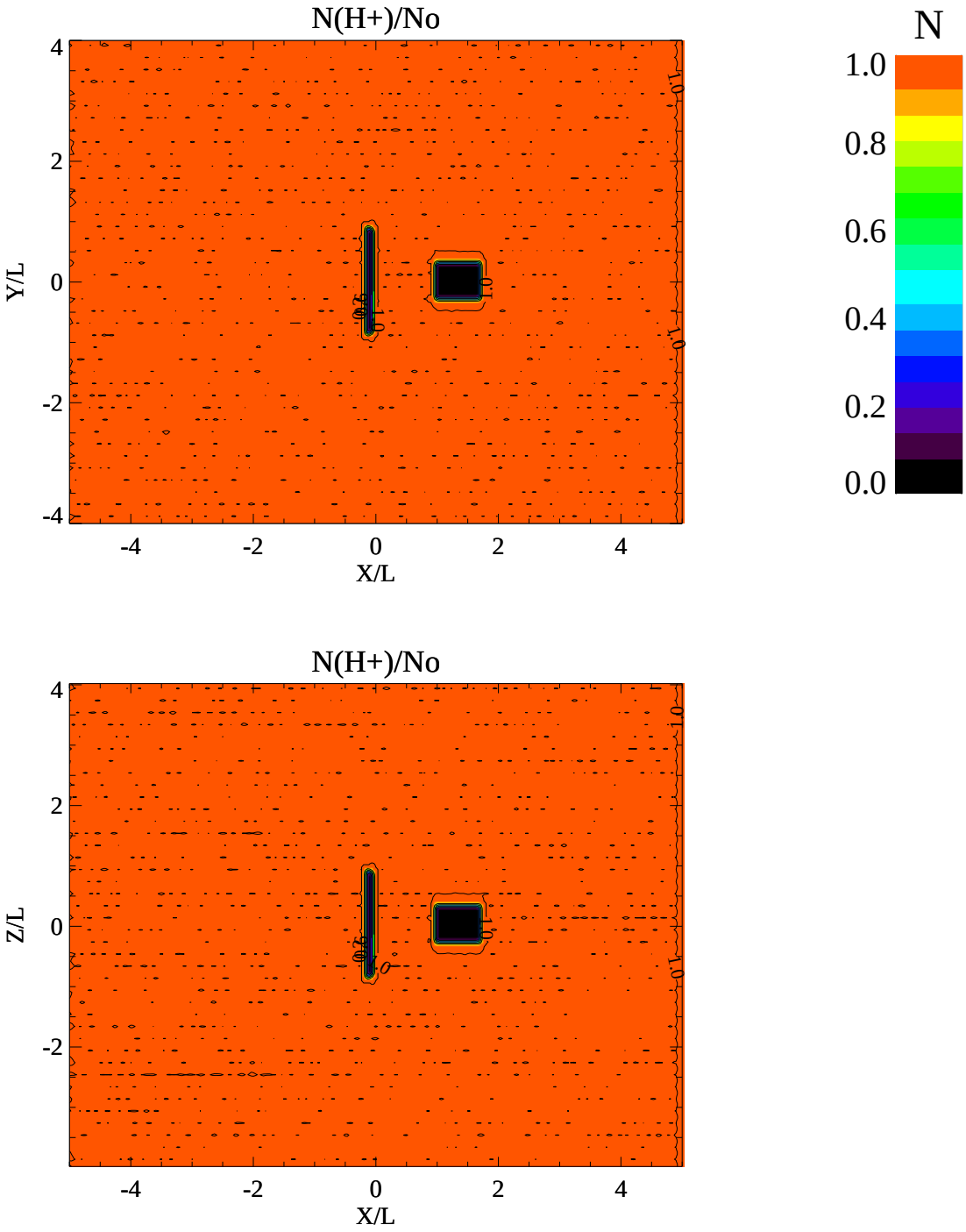

Figure 3. Solar wind ion density in the y-x ($z = 0$) and z-x ($y = 0$) planes. $U_0 = 200\,\mathrm{km/s}$, $M_A = 1.5$, $B_0 = 1500\,\mathrm{nT}$, $n = 5 \times 10^3\,\mathrm{cm}^{-3}$, $\beta_\mathrm{p} = 0.1$, $\beta_\mathrm{e} = 0.1$, $\theta_{bu} = 11^o$. Linear perturbations occur at the beginning of simulation, at $t = 0.014\,T_{ce}$, (case b).

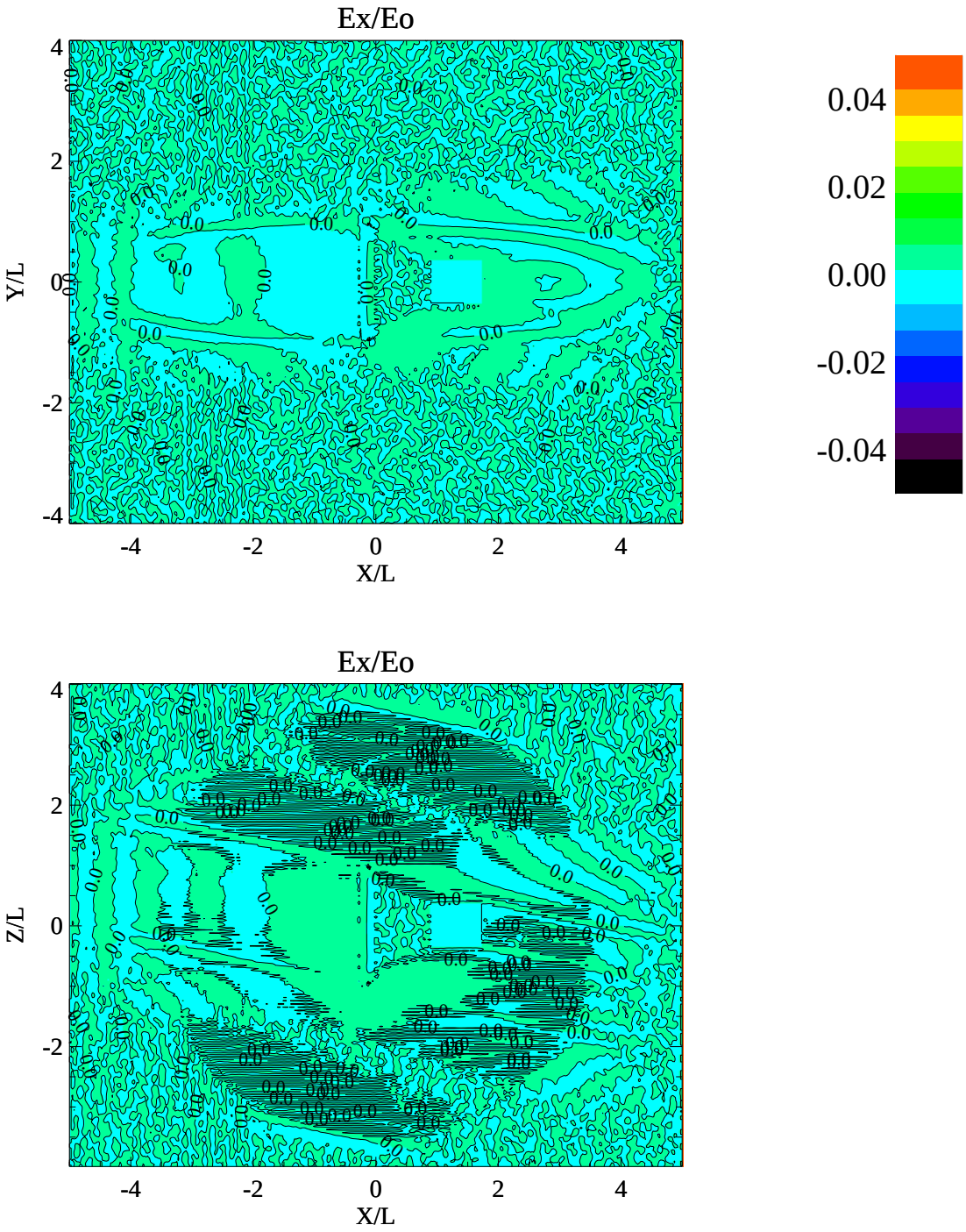

Figure 4. Electric field component $E_x(E_0)$ in the y-x ($z = 0$) and z-x ($y = 0$) planes. $U_0 = 200\,\mathrm{km/s}$, $M_A = 1.5$, $B_0 = 1500\,\mathrm{nT}$, $E_0 = U_0 B_0 = 0.3\,\mathrm{V/m}$, $n_{SW} = 5 \times 10^3\,\mathrm{cm}^{-3}$, $\beta_\mathrm{p} = 0.1$, $\beta_\mathrm{e} = 0.1$, $\theta_{bu} = 11^o$. Linear perturbations at the beginning of simulation, at $t = 0.014\,T_{ce}$, (case a).

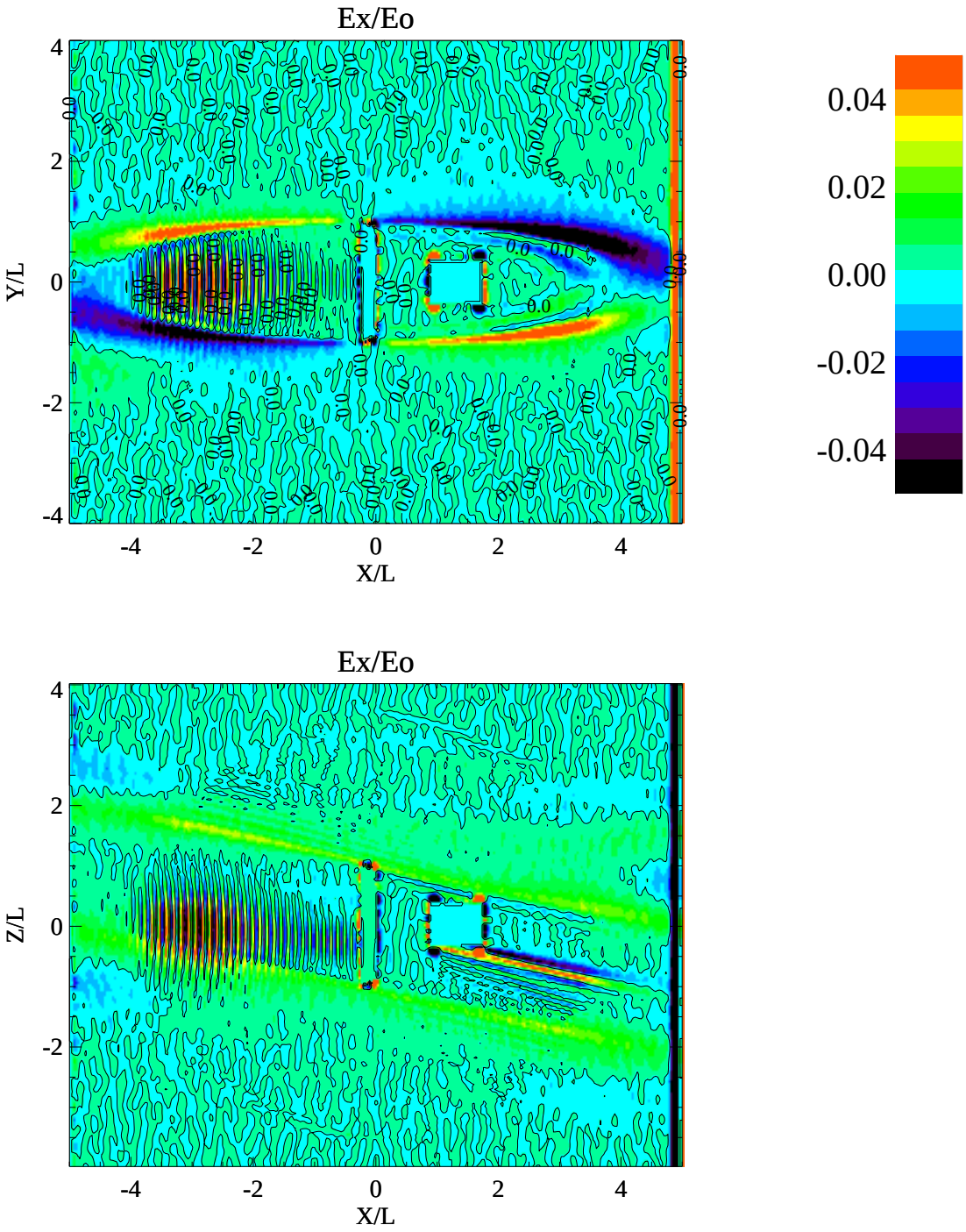

Figure 5. Electric field component $E_x(E_0)$ in the y-x ($z = 0$) and z-x ($y = 0$) planes. $U_0 = 200\,\mathrm{km/s}$, $M_A = 1.5$, $B_0 = 1500\,\mathrm{nT}$, $E_0 = U_0 B_0 = 0.3\,\mathrm{V/m}$, $n_{SW} = 5 \times 10^3\,\mathrm{cm}^{-3}$, $\beta_\mathrm{p} = 0.1$, $\beta_\mathrm{e} = 0.1$, $\theta_{bu} = 11^o$. Linear perturbations at the beginning of simulation, at $t = 0.014\,T_{ce}$ (case b).

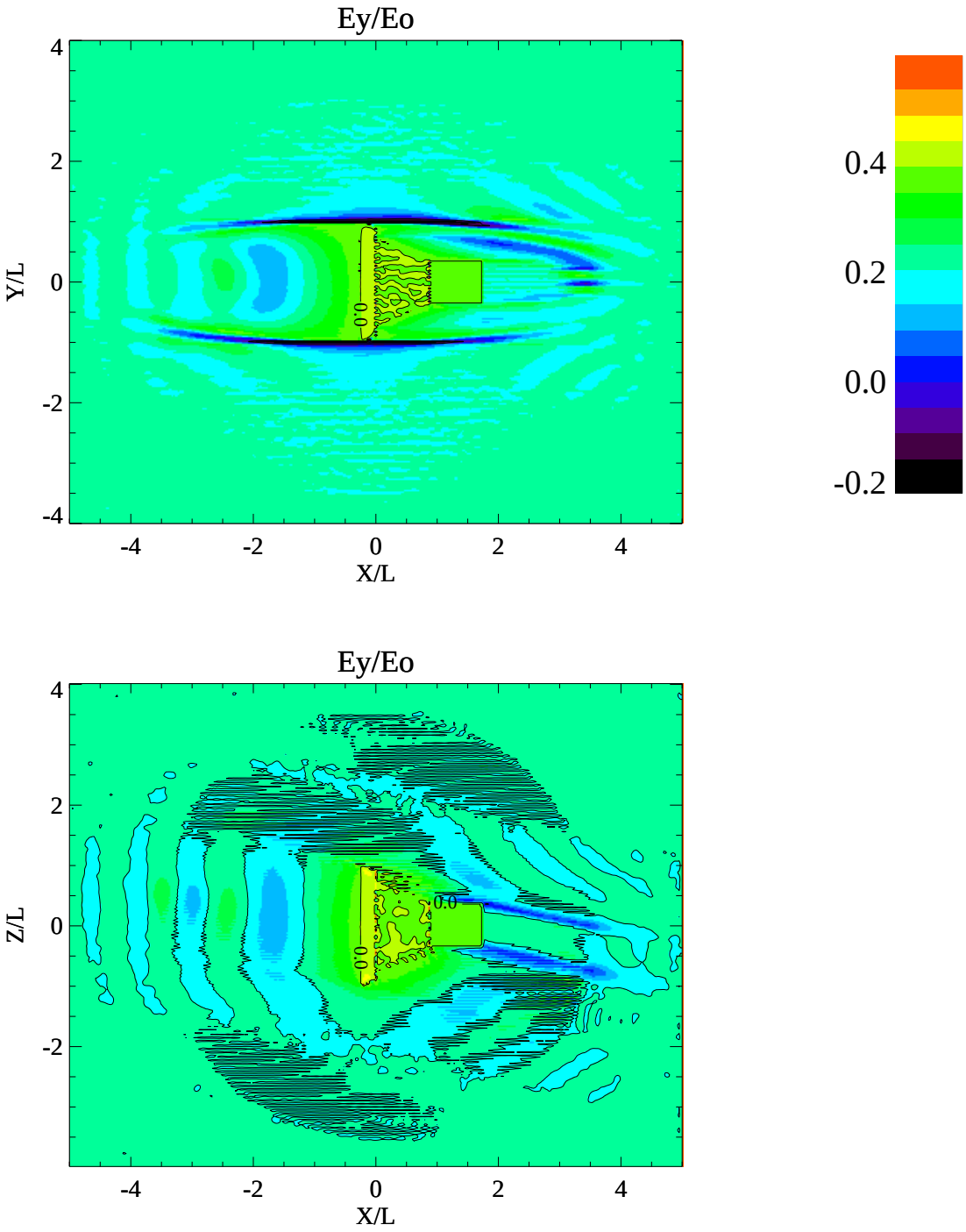

Figure 6. Electric field component $E_y(E_0)$ in the y-x ($z = 0$) and z-x ($y = 0$) planes. $U_0 = 200\,\mathrm{km/s}$, $M_A = 1.5$, $B_0 = 1500\,\mathrm{nT}$, $n = 5\times10^3\,\mathrm{cm}^{-3}$, $\beta_\mathrm{p} = 0.1$, $\beta_\mathrm{e} = 0.1$, $\theta_{bu} = 11^o$. Linear perturbations at the beginning of simulation, at $t = 0.014\,T_{ce}$, (case a).

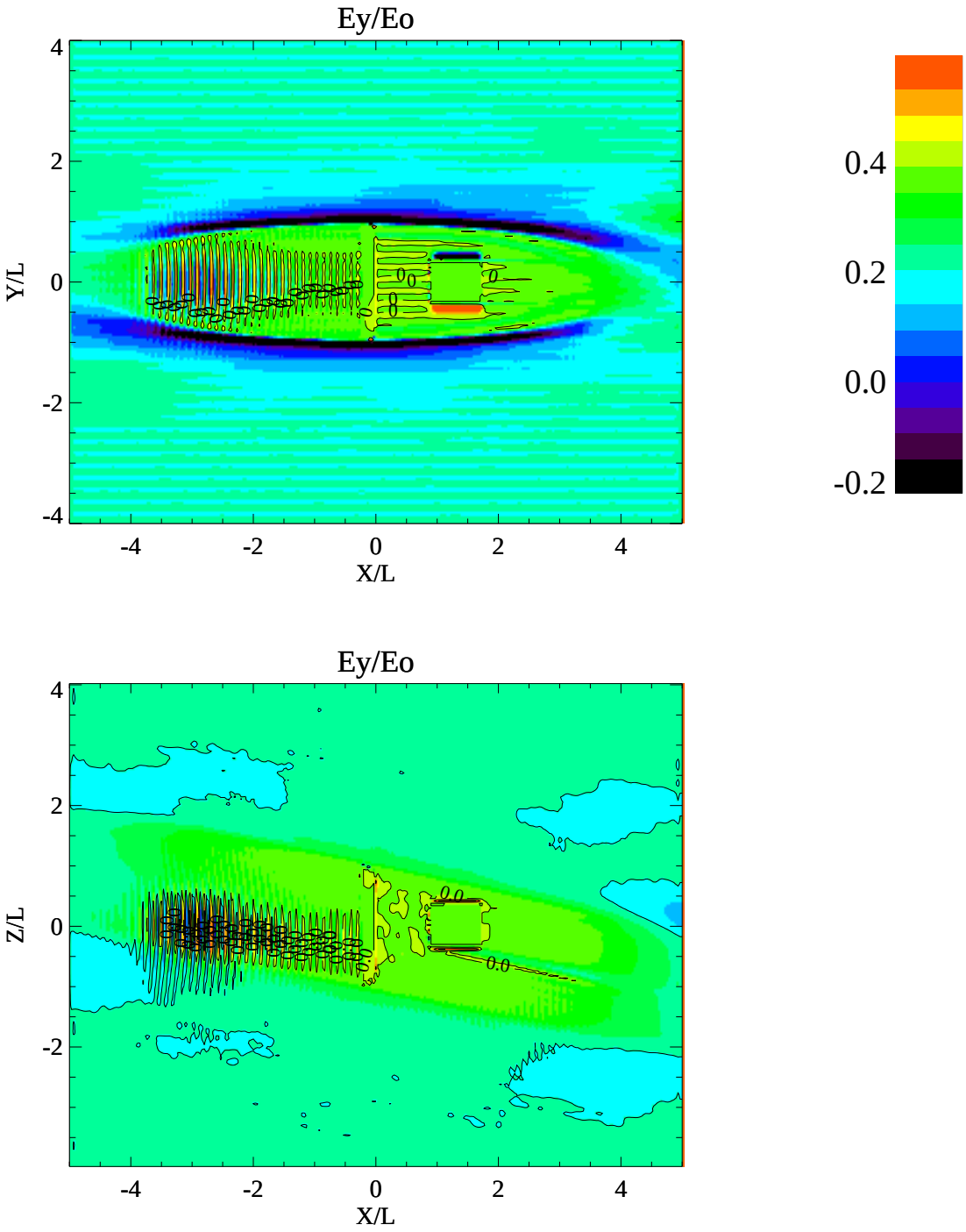

Figure 7. Electric field component $E_y(E_0)$ in the y-x ($z = 0$) and z-x ($y = 0$) planes. $U_0 = 200\,\mathrm{km/s}$, $M_A = 1.5$, $B_0 = 1500\,\mathrm{nT}$, $n = 5\times10^3\,\mathrm{cm}^{-3}$, $\beta_\mathrm{p} = 0.1$, $\beta_\mathrm{e} = 0.1$, $\theta_{bu} = 11^o$. Linear perturbations at the beginning of simulation, at $t = 0.014\,T_{ce}$ (case b).

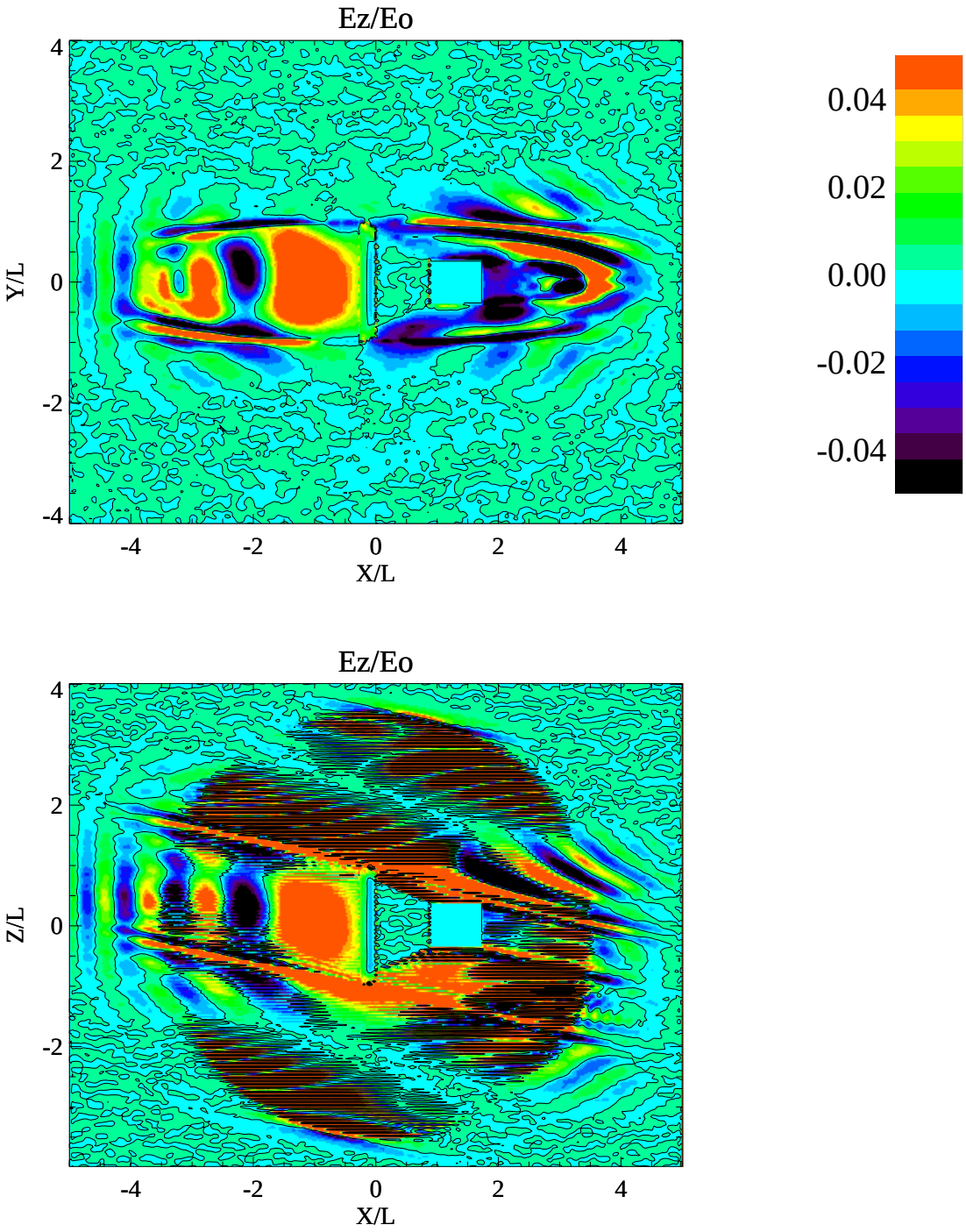

Figure 8. Electric field component $E_z(E_0)$ in the y-x ($z = 0$) and z-x ($y = 0$) planes. $U_0 = 200\,\mathrm{km/s}$, $M_A = 1.5$, $B_0 = 1500\,\mathrm{nT}$, $n = 5\times10^3\,\mathrm{cm}^{-3}$, $\beta_\mathrm{p} = 0.1$, $\beta_\mathrm{e} = 0.1$, $\theta_{bu} = 11^o$. Linear perturbations at the beginning of simulation, at $t = 0.014\,T_{ce}$, (case a).

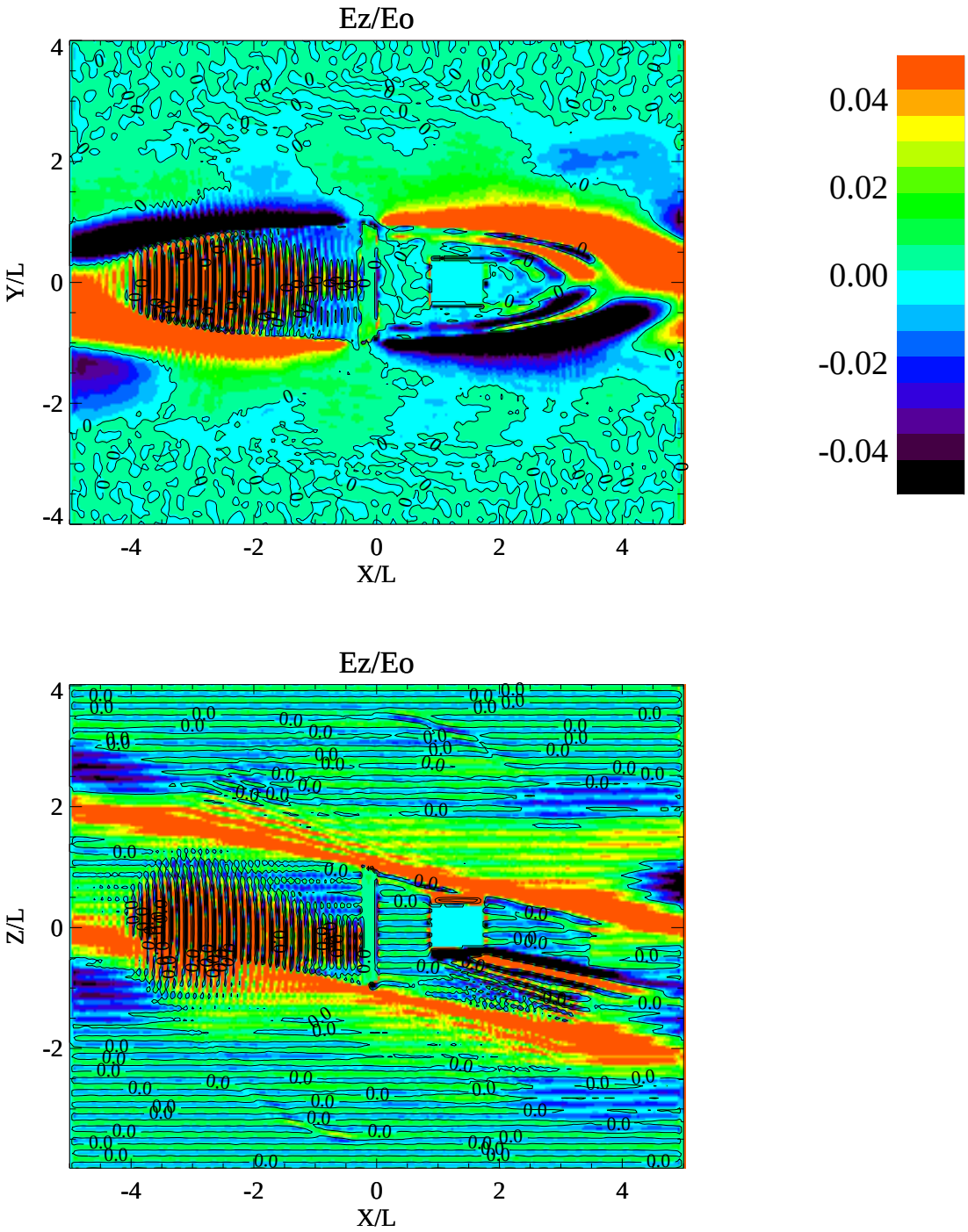

Figure 9. Electric field component $E_z(E_0)$ in the y-x ($z = 0$) and z-x ($y = 0$) planes. $U_0 = 200\,\mathrm{km/s}$, $M_A = 1.5$, $B_0 = 1500\,\mathrm{nT}$, $n = 5\times10^3\,\mathrm{cm}^{-3}$, $\beta_\mathrm{p} = 0.1$, $\beta_\mathrm{e} = 0.1$, $\theta_{bu} = 11^o$. Linear perturbations at the beginning of simulation, at $t = 0.014\,T_{ce}$ (case b).

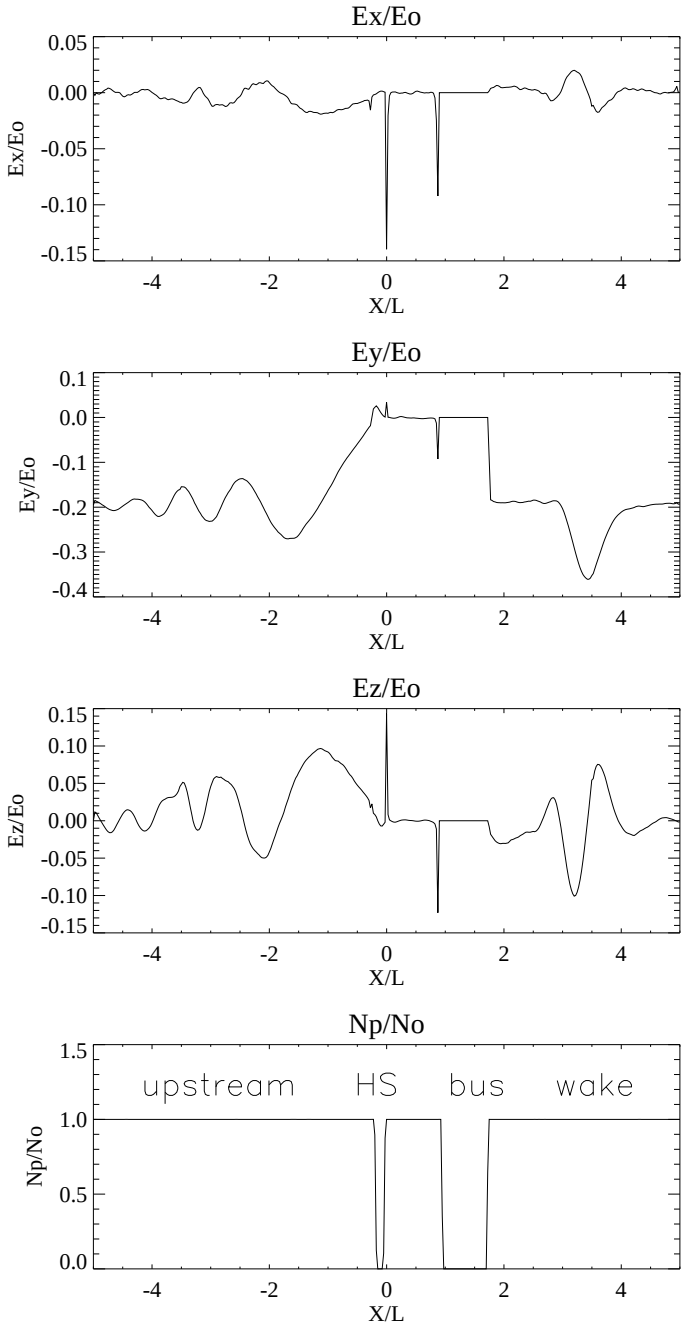

Figure 10. 1-D cuts for the electric field component $E_x(E_0)$, $E_y(E_0)$ and $E_z(E_0)$ ($y = 0$, $z = 0$). $U_0 = 200\,\mathrm{km/s}$, $M_A = 1.5$, $B_0 = 1500\,\mathrm{nT}$, $n = 5 \times 10^3\,\mathrm{cm}^{-3}$, $\beta_\mathrm{p} = 0.1$, $\beta_\mathrm{e} = 0.1$, $\theta_{bu} = 11^o$. Linear perturbations at the beginning of simulation, at $t = 0.014\,T_{ce}$, (case a).

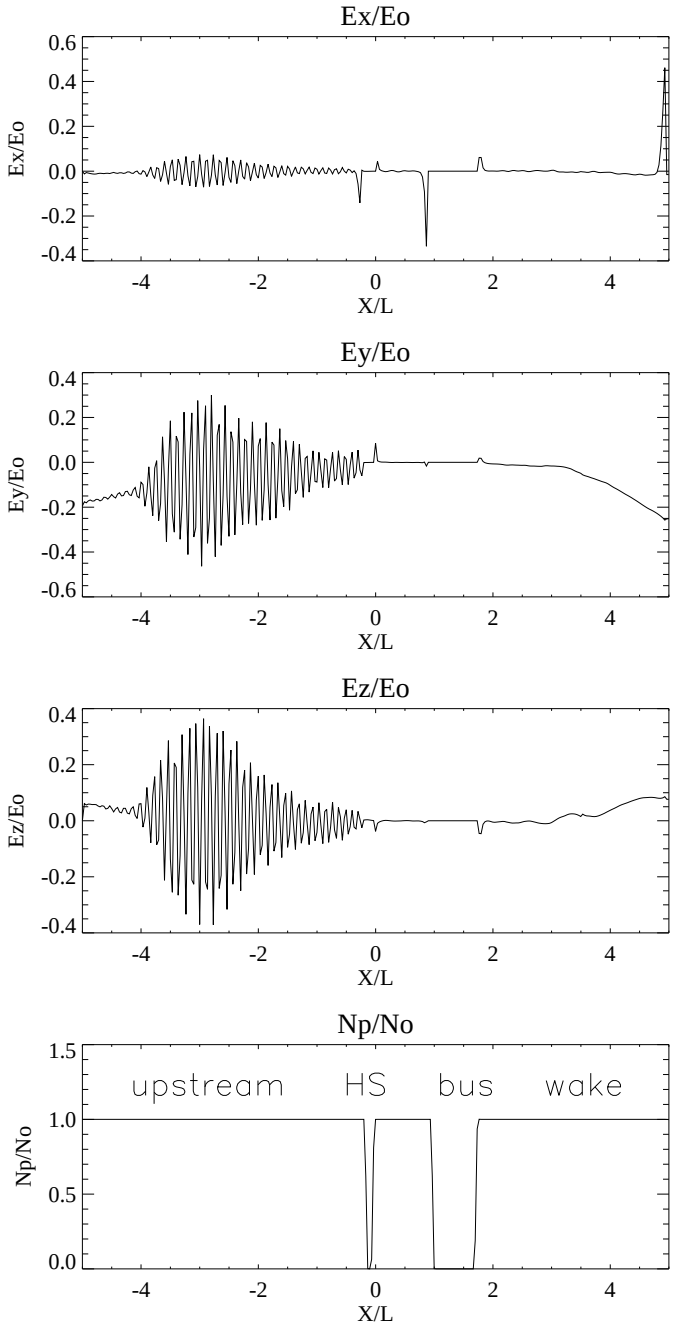

Figure 11. 1-D cuts for the electric field component $E_x(E_0)$, $E_y(E_0)$ and $E_z(E_0)$ ($y = 0$, $z = 0$). $U_0 = 200\,\mathrm{km/s}$, $M_A = 1.5$, $B_0 = 1500\,\mathrm{nT}$, $n = 5 \times 10^3\,\mathrm{cm}^{-3}$, $\beta_\mathrm{p} = 0.1$, $\beta_\mathrm{e} = 0.1$, $\theta_{bu} = 11^o$. Linear perturbations at the beginning of simulation, at $t = 0.014\,T_{ce}$ (case b).

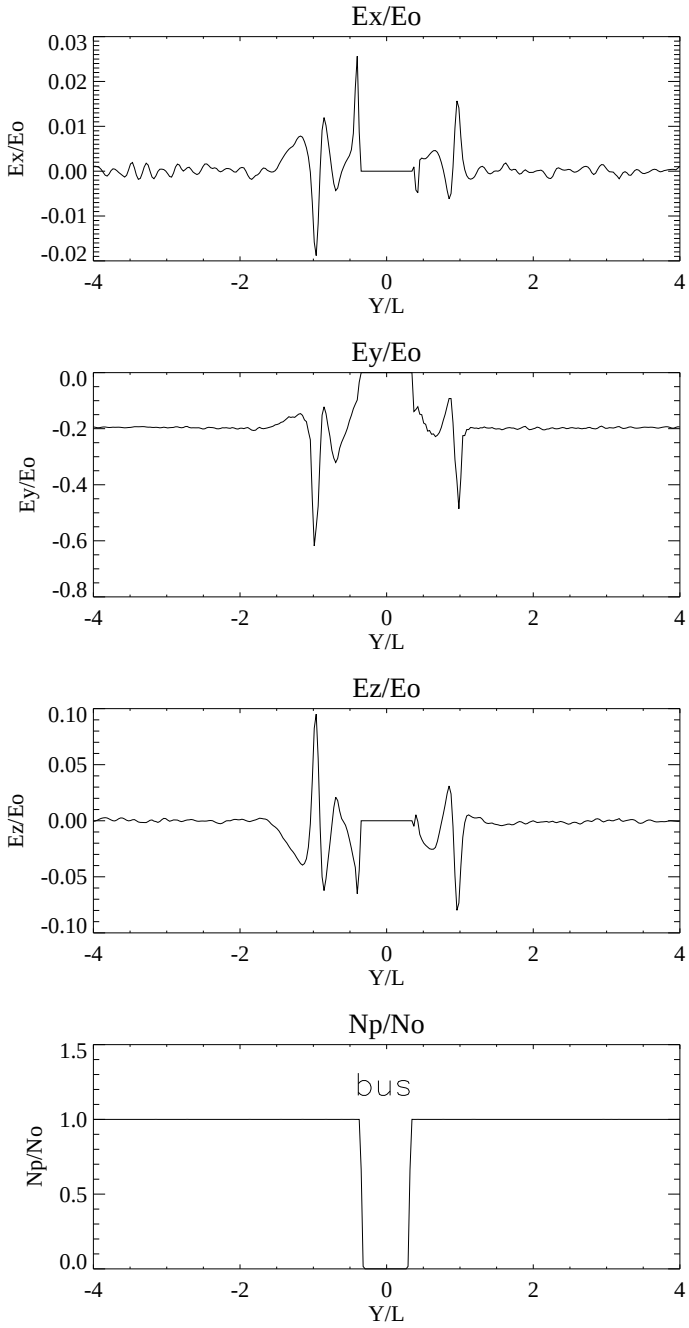

Figure 12. 1-D cuts for the electric field component $E_x(E_0)$, $E_y(E_0)$ and E_z (E_0) $(x = 1.5,\, z = 0)$. $U_0 = 200\,\mathrm{km/s}$, $M_A = 1.5$, $B_0 = 1500\,\mathrm{nT}$, $n = 5 \times 10^3\,\mathrm{cm}^{-3}$, $\beta_\mathrm{p} = 0.1$, $\beta_\mathrm{e} = 0.1$, $\theta_{bu} = 11^o$. Linear perturbations at the beginning of simulation, at $t = 0.014\,T_{ce}$, (case a).

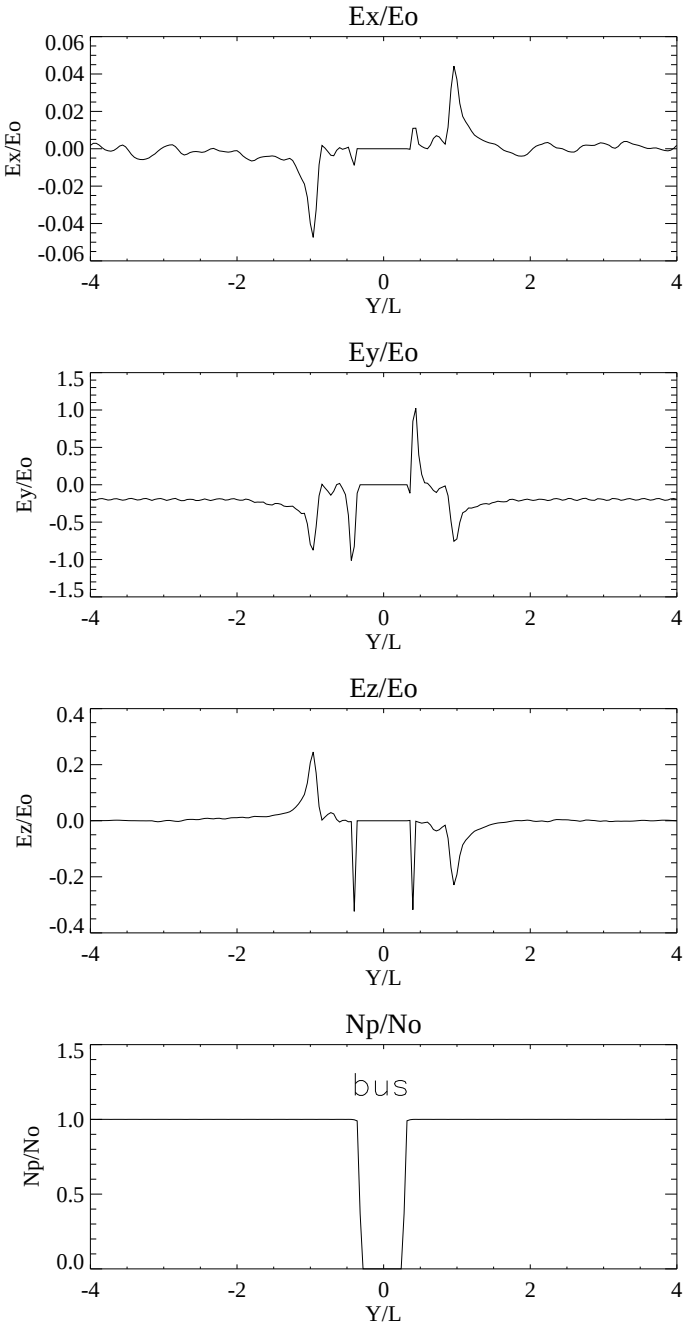

Figure 13. 1-D cuts for the electric field component $E_x(E_0)$, $E_y(E_0)$ and $E_z(E_0)$ ($x = 1.5$, $z = 0$). $U_0 = 200\,\mathrm{km/s}$, $M_A = 1.5$, $B_0 = 1500\,\mathrm{nT}$, $n = 5 \times 10^3\,\mathrm{cm}^{-3}$, $\beta_\mathrm{p} = 0.1$, $\beta_\mathrm{e} = 0.1$, $\theta_{bu} = 11^o$. Linear perturbations at the beginning of simulation, at $t = 0.014\,T_{ce}$ (case b).

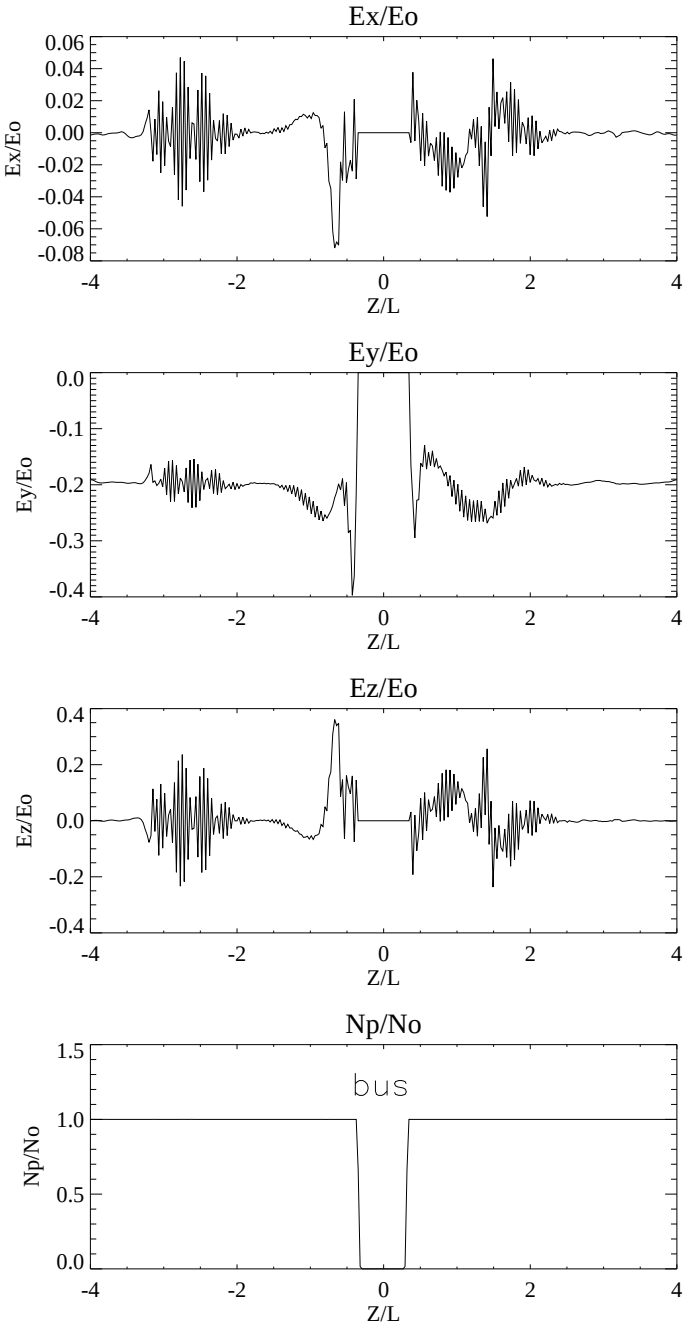

Figure 14. 1-D cuts for the electric field component $E_x(E_0)$, $E_y(E_0)$ and $E_z(E_0)$ ($x = 1.5$, $y = 0$). $U_0 = 200\,\mathrm{km/s}$, $M_A = 1.5$, $B_0 = 1500\,\mathrm{nT}$, $n = 5 \times 10^3\,\mathrm{cm}^{-3}$, $\beta_\mathrm{p} = 0.1$, $\beta_\mathrm{e} = 0.1$, $\theta_{bu} = 11^o$. Linear perturbations at the beginning of simulation, at $t = 0.014\,T_{ce}$, (case a).

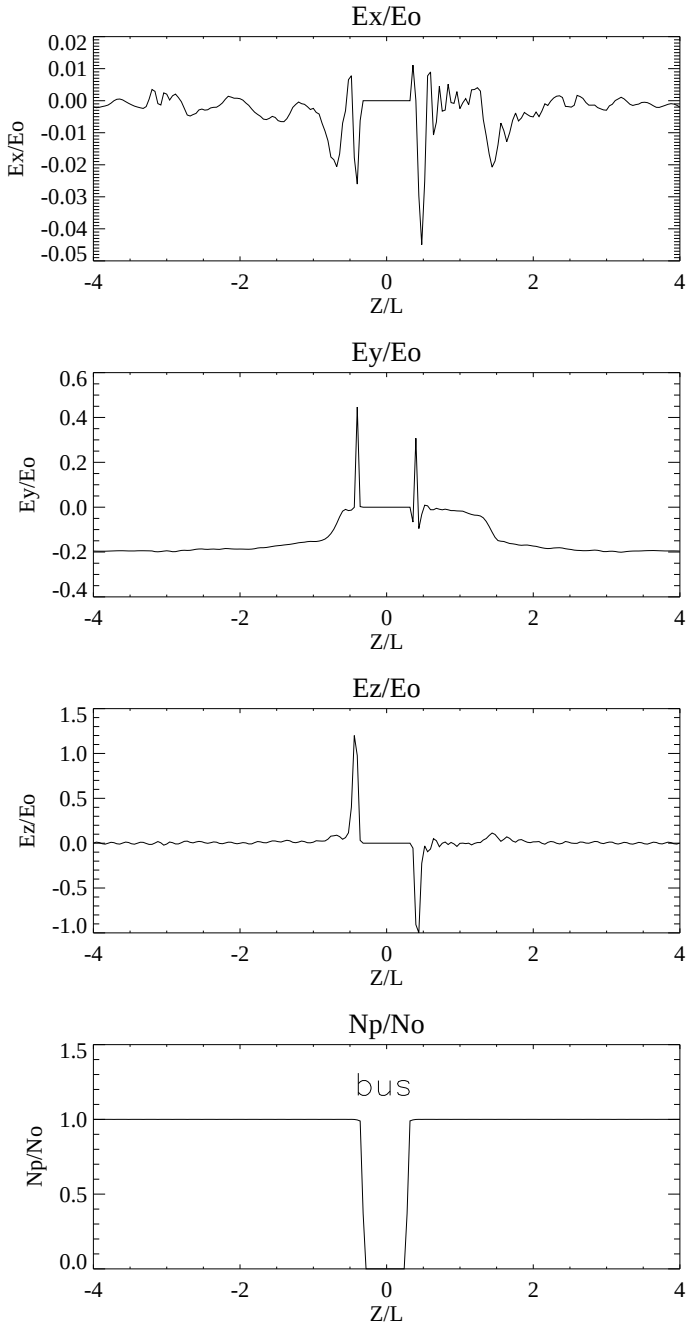

Figure 15. 1-D cuts for the electric field component $E_x(E_0)$, $E_y(E_0)$ and $E_z(E_0)$ ($x = 1.5$, $y = 0$). $U_0 = 200\,\mathrm{km/s}$, $M_A = 1.5$, $B_0 = 1500\,\mathrm{nT}$, $n = 5 \times 10^3\,\mathrm{cm}^{-3}$, $\beta_\mathrm{p} = 0.1$, $\beta_\mathrm{e} = 0.1$, $\theta_{bu} = 11^o$. Linear perturbations at the beginning of simulation, at $t = 0.014\,T_{ce}$ (case b).

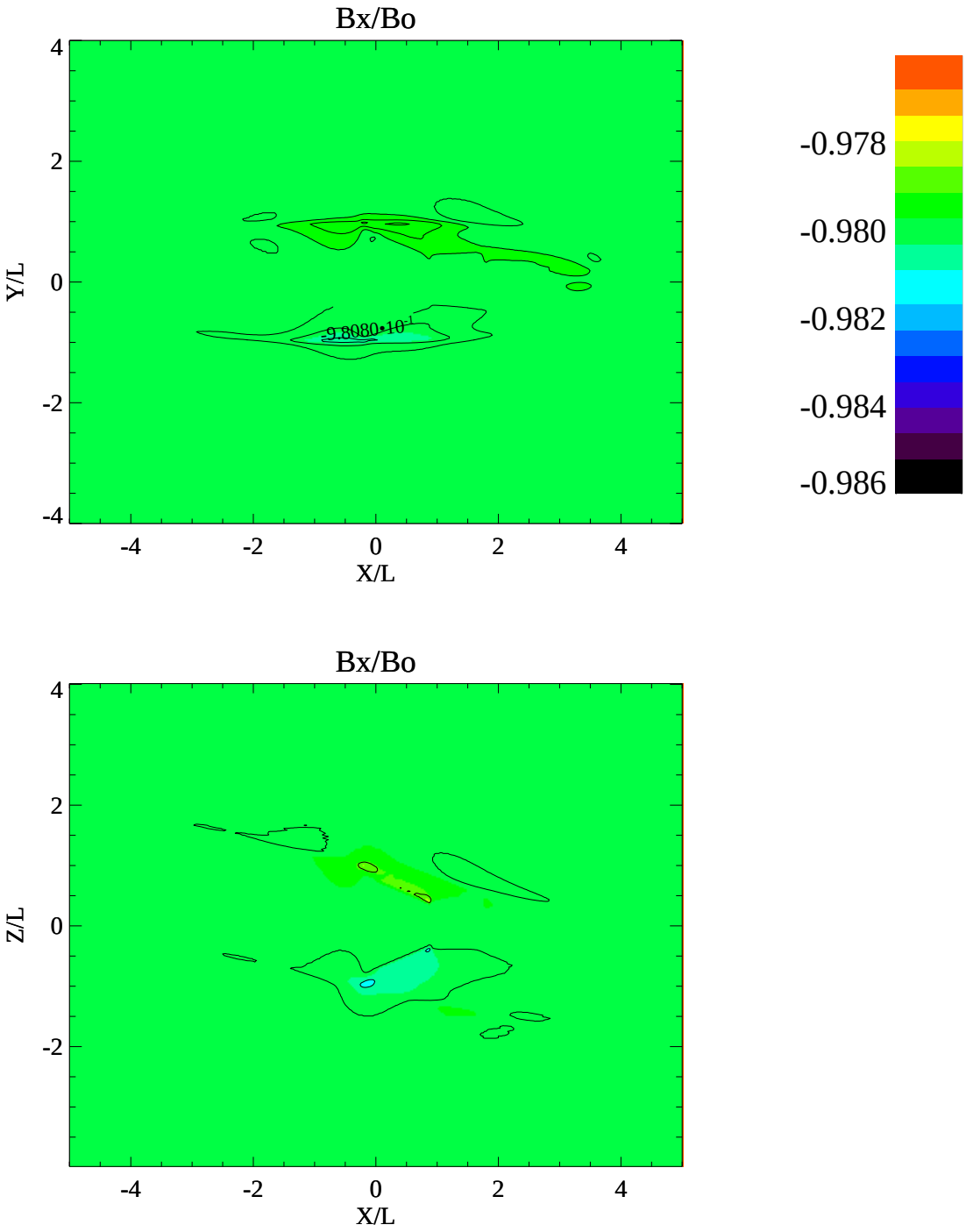

Figure 16. Magnetic field component $B_x(B_0)$ in the y-x ($z = 0$) and z-x ($y = 0$) planes. $U_0 = 200\,\mathrm{km/s}$, $M_A = 1.5$, $B_0 = 1500\,\mathrm{nT}$, $n = 5\times10^3\,\mathrm{cm}^{-3}$, $\beta_\mathrm{p} = 0.1$, $\beta_\mathrm{e} = 0.1$, $\theta_{bu} = 11^o$. Linear perturbations at the beginning of simulation, at $t = 0.014\,T_{ce}$, (case a).

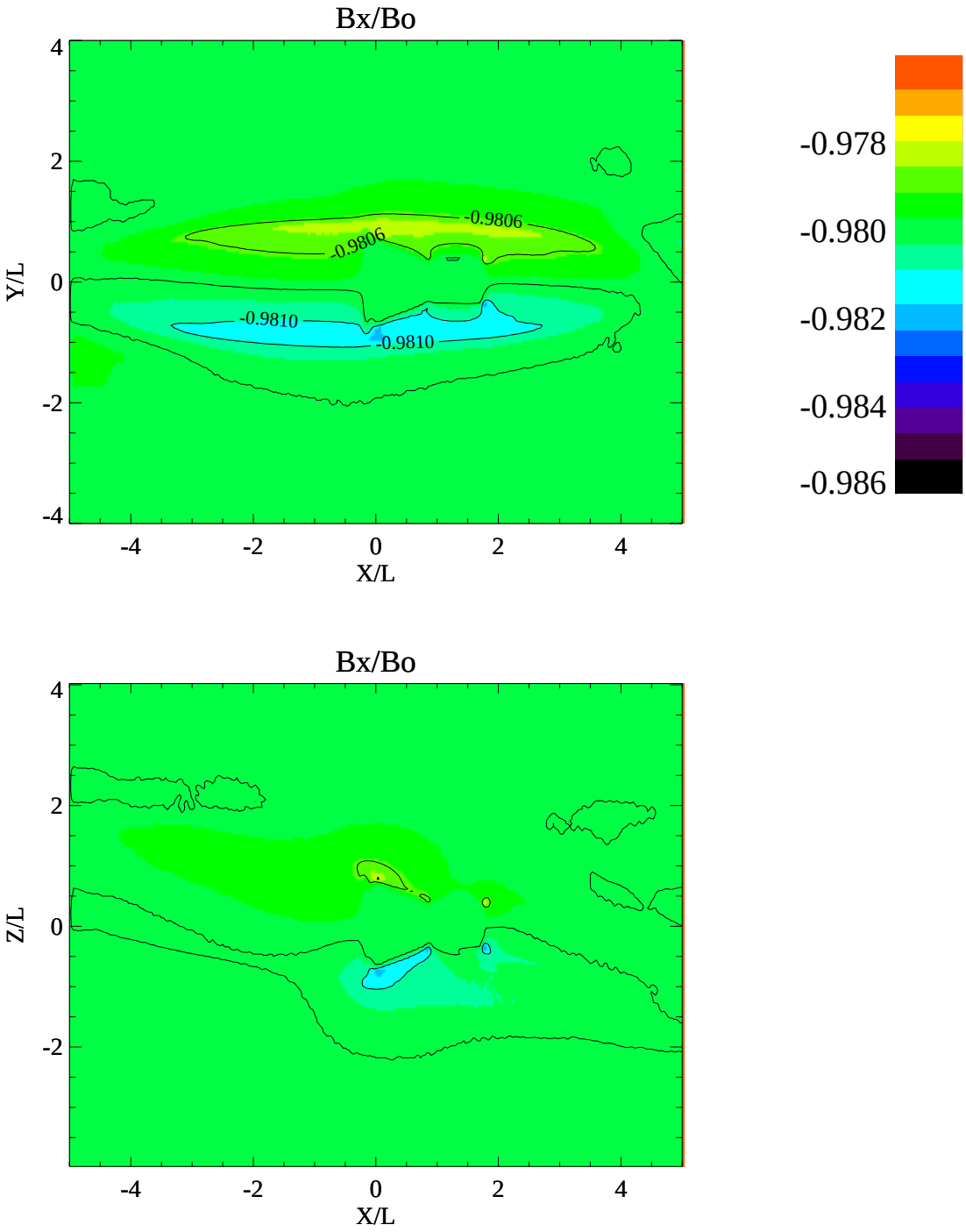

Figure 17. Magnetic field component $B_x(B_0)$ in the y-x ($z = 0$) and z-x ($y = 0$) planes. $U_0 = 200\,\mathrm{km/s}$, $M_A = 1.5$, $B_0 = 1500\,\mathrm{nT}$, $n = 5\times10^3\,\mathrm{cm}^{-3}$, $\beta_\mathrm{p} = 0.1$, $\beta_\mathrm{e} = 0.1$, $\theta_{bu} = 11^o$. Linear perturbations at the beginning of simulation, at $t = 0.014\,T_{ce}$ (case b).

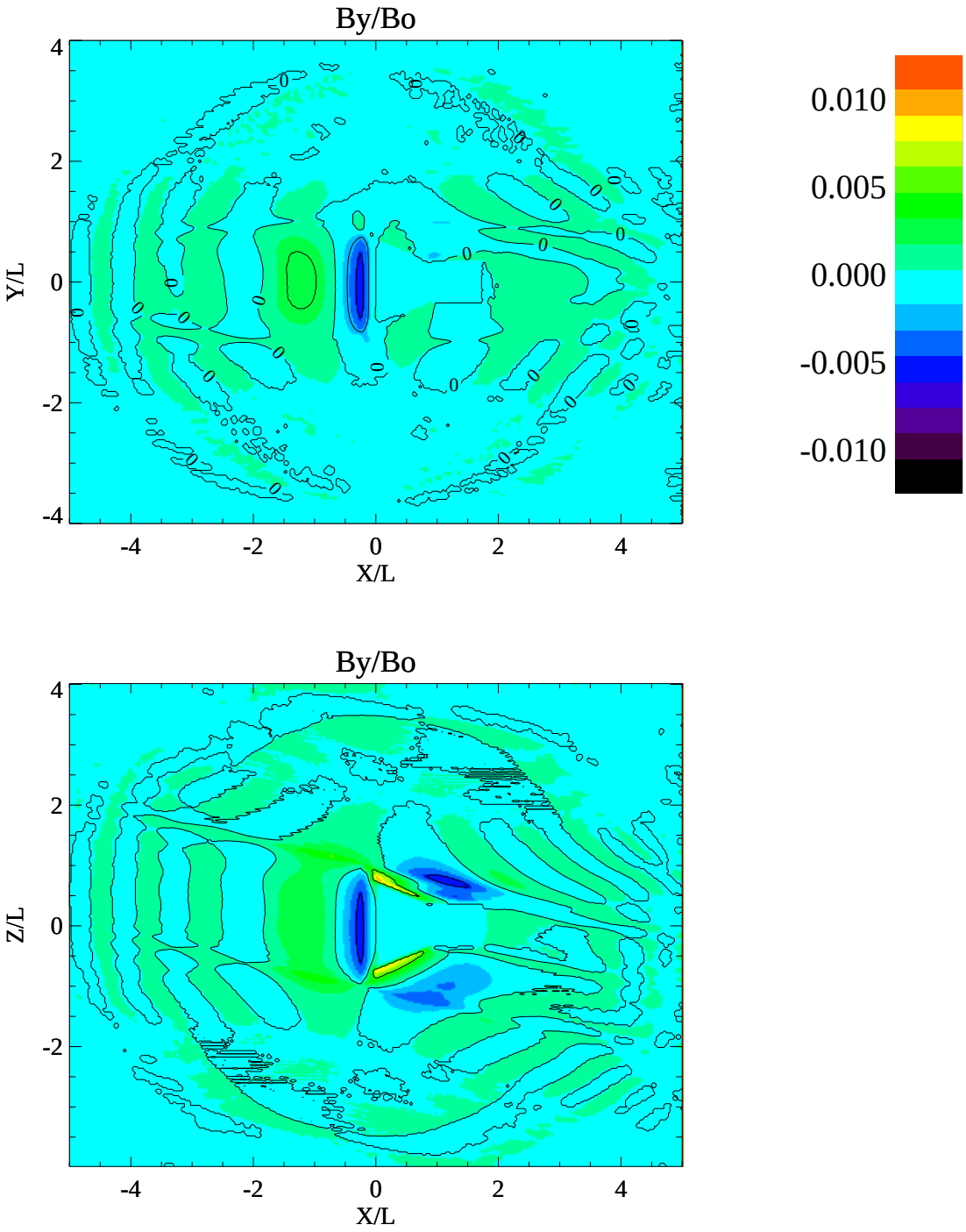

Figure 18. Magnetic field component $B_y(B_0)$ in the y-x ($z = 0$) and z-x ($y = 0$) planes. $U_0 = 200\,\mathrm{km/s}$, $M_A = 1.5$, $B_0 = 1500\,\mathrm{nT}$, $n = 5\times10^3\,\mathrm{cm}^{-3}$, $\beta_\mathrm{p} = 0.1$, $\beta_\mathrm{e} = 0.1$, $\theta_{bu} = 11^o$. Linear perturbations at the beginning of simulation, at $t = 0.014\,T_{ce}$, (case a).

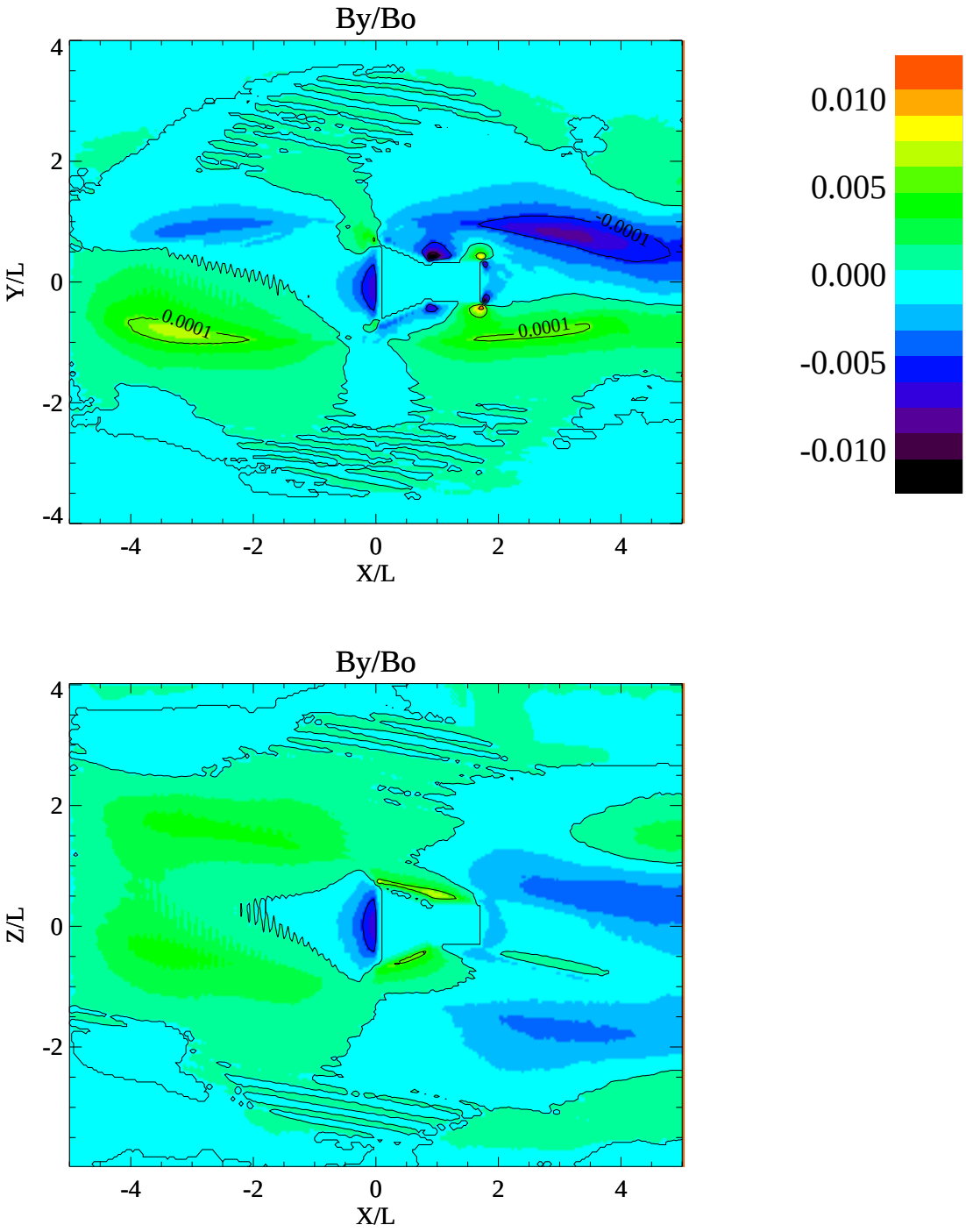

Figure 19. Magnetic field component $B_y(B_0)$ in the y-x ($z = 0$) and z-x ($y = 0$) planes. $U_0 = 200\,\mathrm{km/s}$, $M_A = 1.5$, $B_0 = 1500\,\mathrm{nT}$, $n = 5\times10^3\,\mathrm{cm}^{-3}$, $\beta_\mathrm{p} = 0.1$, $\beta_\mathrm{e} = 0.1$, $\theta_{bu} = 11^o$. Linear perturbations at the beginning of simulation, at $t = 0.014\,T_{ce}$ (case b).

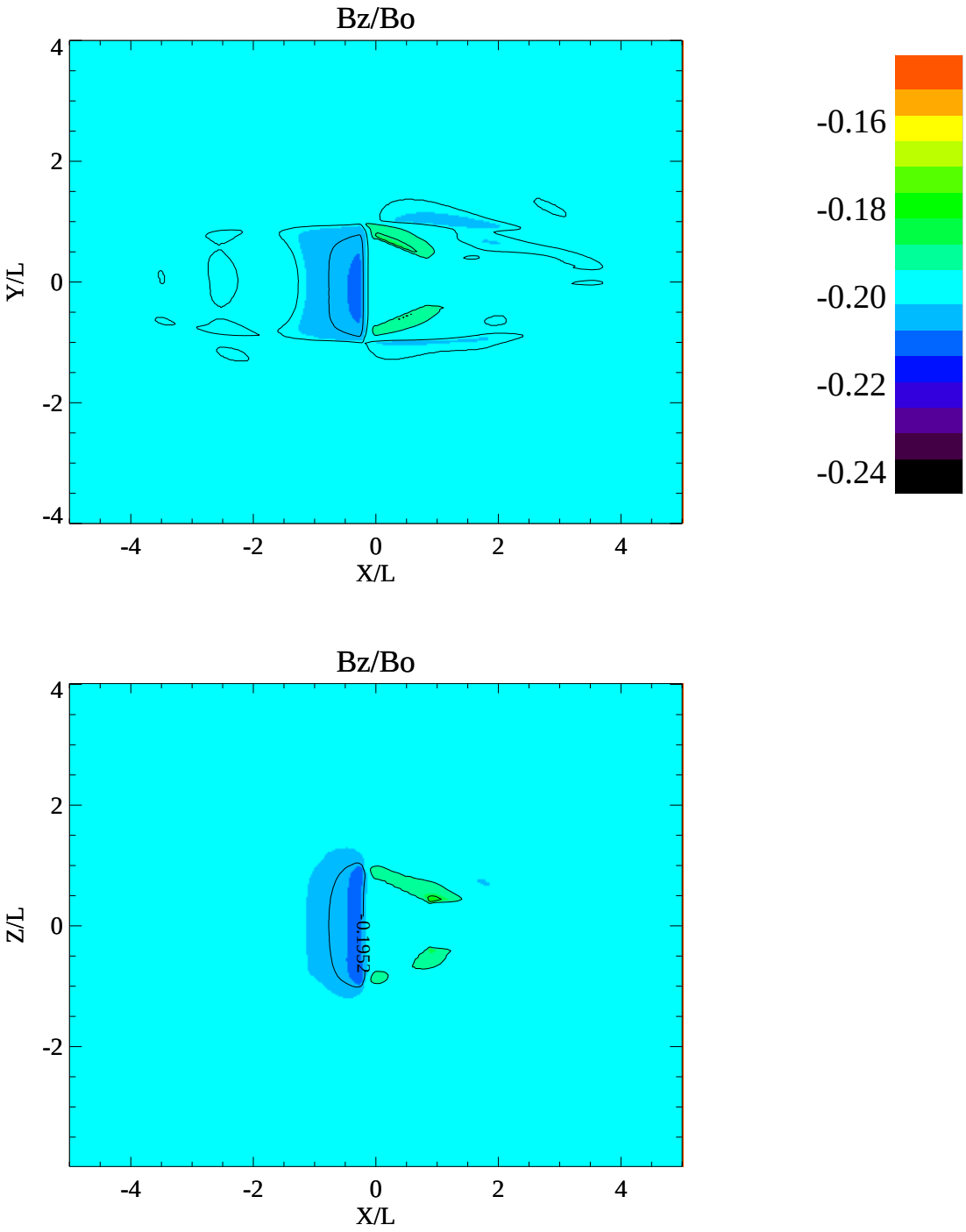

Figure 20. Magnetic field component $B_z(B_0)$ in the y-x ($z = 0$) and z-x ($y = 0$) planes. $U_0 = 200\,\mathrm{km/s}$, $M_A = 1.5$, $B_0 = 1500\,\mathrm{nT}$, $n = 5\times10^3\,\mathrm{cm}^{-3}$, $\beta_\mathrm{p} = 0.1$, $\beta_\mathrm{e} = 0.1$, $\theta_{bu} = 11^o$. Linear perturbations at the beginning of simulation, at $t = 0.014\,T_{ce}$, (case a).

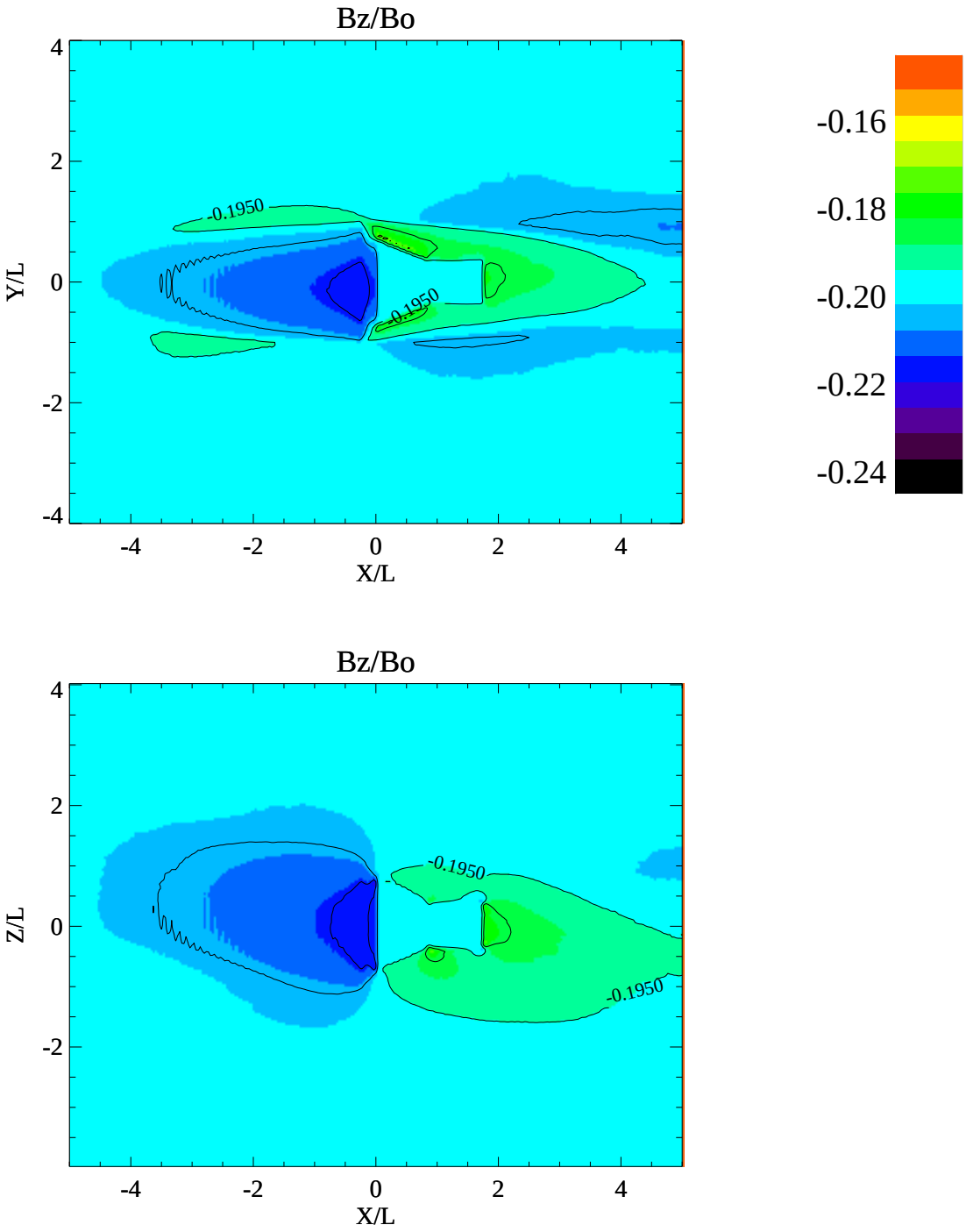

Figure 21. Magnetic field component $B_z(B_0)$ in the y-x ($z = 0$) and z-x ($y = 0$) planes. $U_0 = 200\,\mathrm{km/s}$, $M_A = 1.5$, $B_0 = 1500\,\mathrm{nT}$, $n = 5\times10^3\,\mathrm{cm}^{-3}$, $\beta_\mathrm{p} = 0.1$, $\beta_\mathrm{e} = 0.1$, $\theta_{bu} = 11^o$. Linear perturbations at the beginning of simulation, at $t = 0.014\,T_{ce}$ (case b).

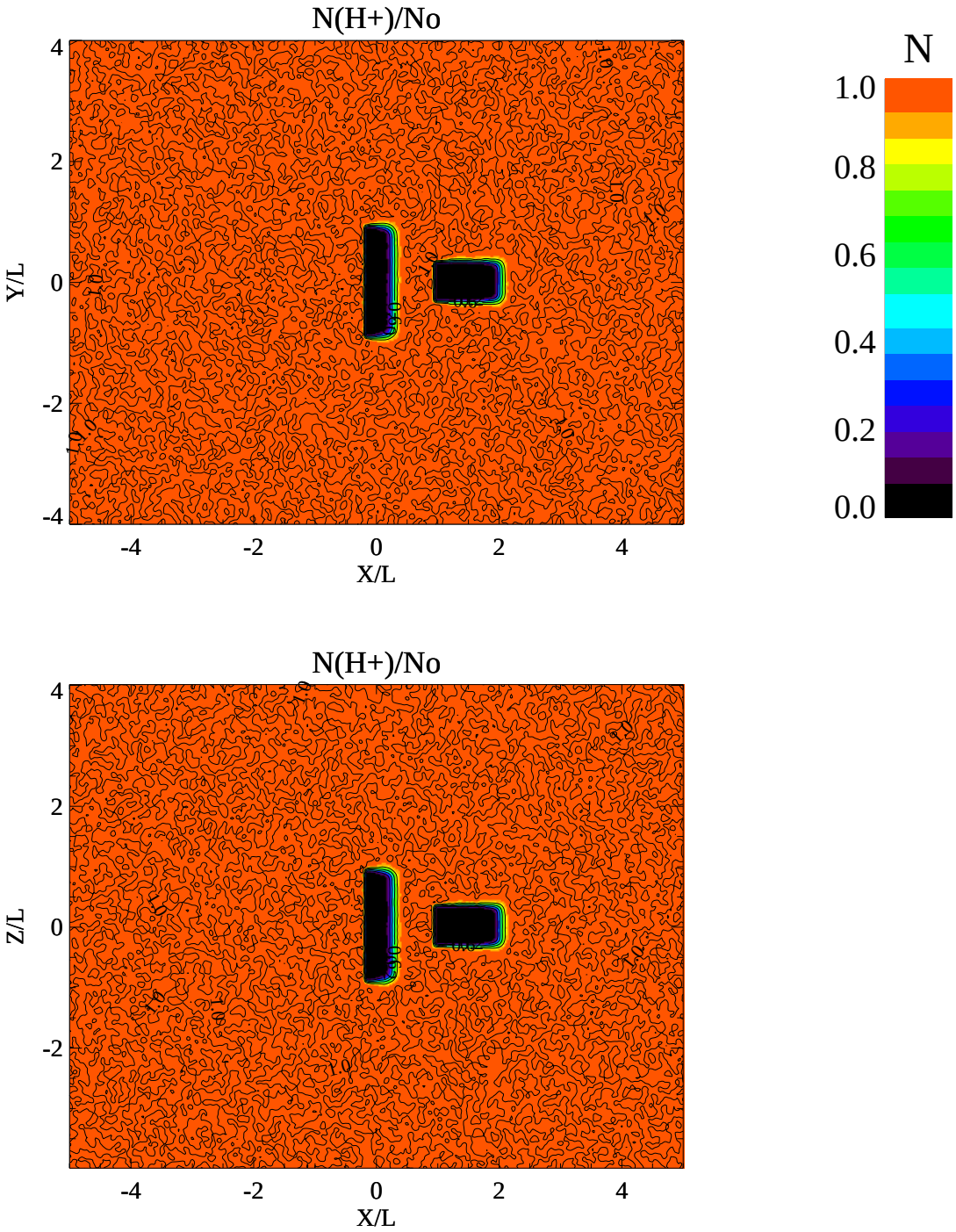

Figure 22. Solar wind ion density in the y-x ($z = 0$) and z-x ($y = 0$) planes. $U_0 = 200\,\mathrm{km/s}$, $M_A = 1.5$, $B_0 = 1500\,\mathrm{nT}$, $E_0 = U_0 B_0 = 0.3\,\mathrm{V/m}$, $n_{SW} = 5 \times 10^3\,\mathrm{cm}^{-3}$, $\beta_\mathrm{p} = 0.1$, $\beta_\mathrm{e} = 0.1$, $\theta_{bu} = 11^o$. Nonlinear saturation of the perturbations at $t = 0.104\,T_{ce}(0.013\,T_{transit})$, (case a).

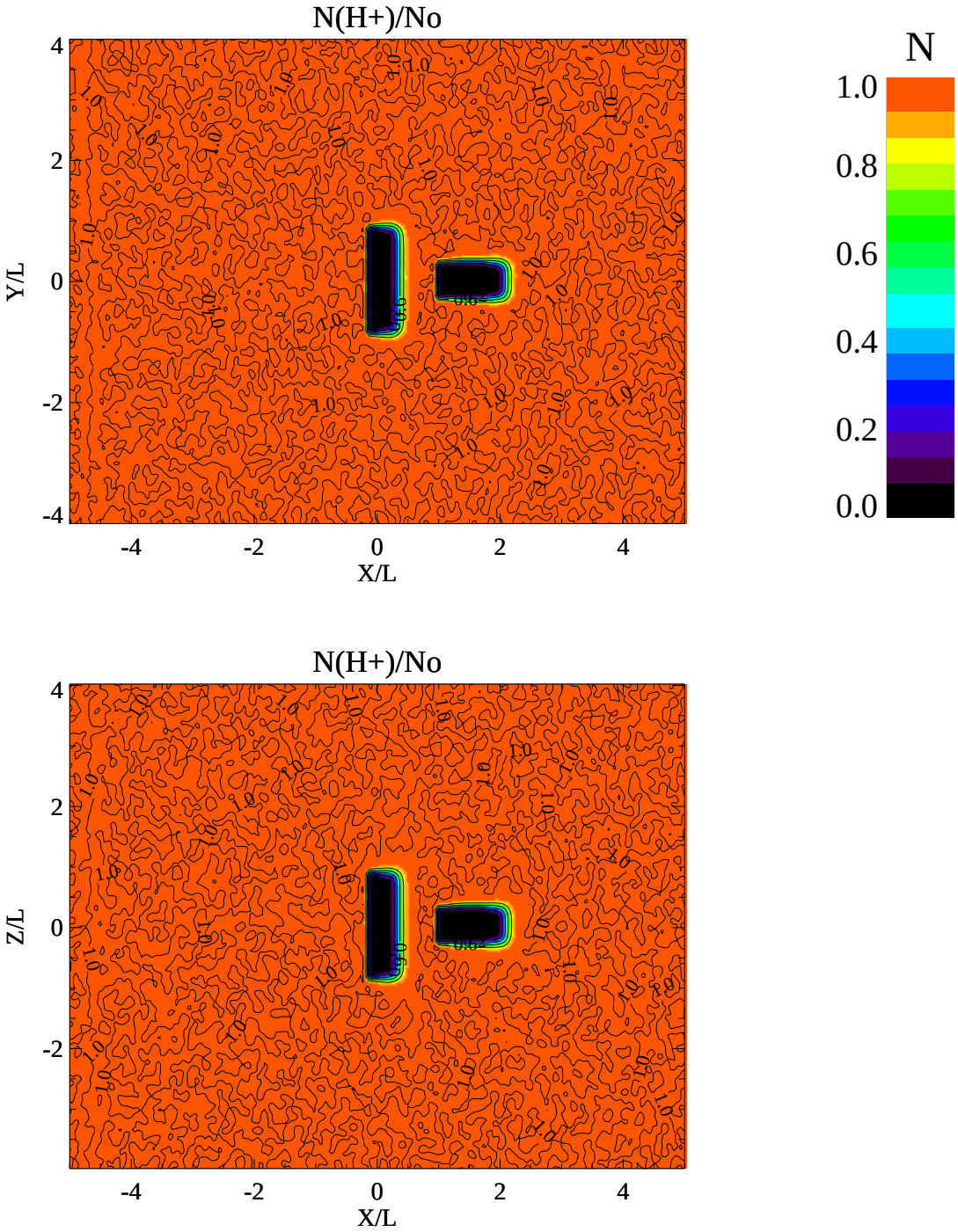

Figure 23. Solar wind ion density in the y-x ($z = 0$) and z-x ($y = 0$) planes. $U_0 = 200\,\mathrm{km/s}$, $M_A = 1.5$, $B_0 = 1500\,\mathrm{nT}$, $E_0 = U_0 B_0 = 0.3\,\mathrm{V/m}$, $n_{SW} = 5 \times 10^3\,\mathrm{cm}^{-3}$, $\beta_\mathrm{p} = 0.1$, $\beta_\mathrm{e} = 0.1$, $\theta_{bu} = 11^o$. Nonlinear saturation of the perturbations at $t = 0.15\,T_{ce}(0.02\,T_{transit})$ (case b).

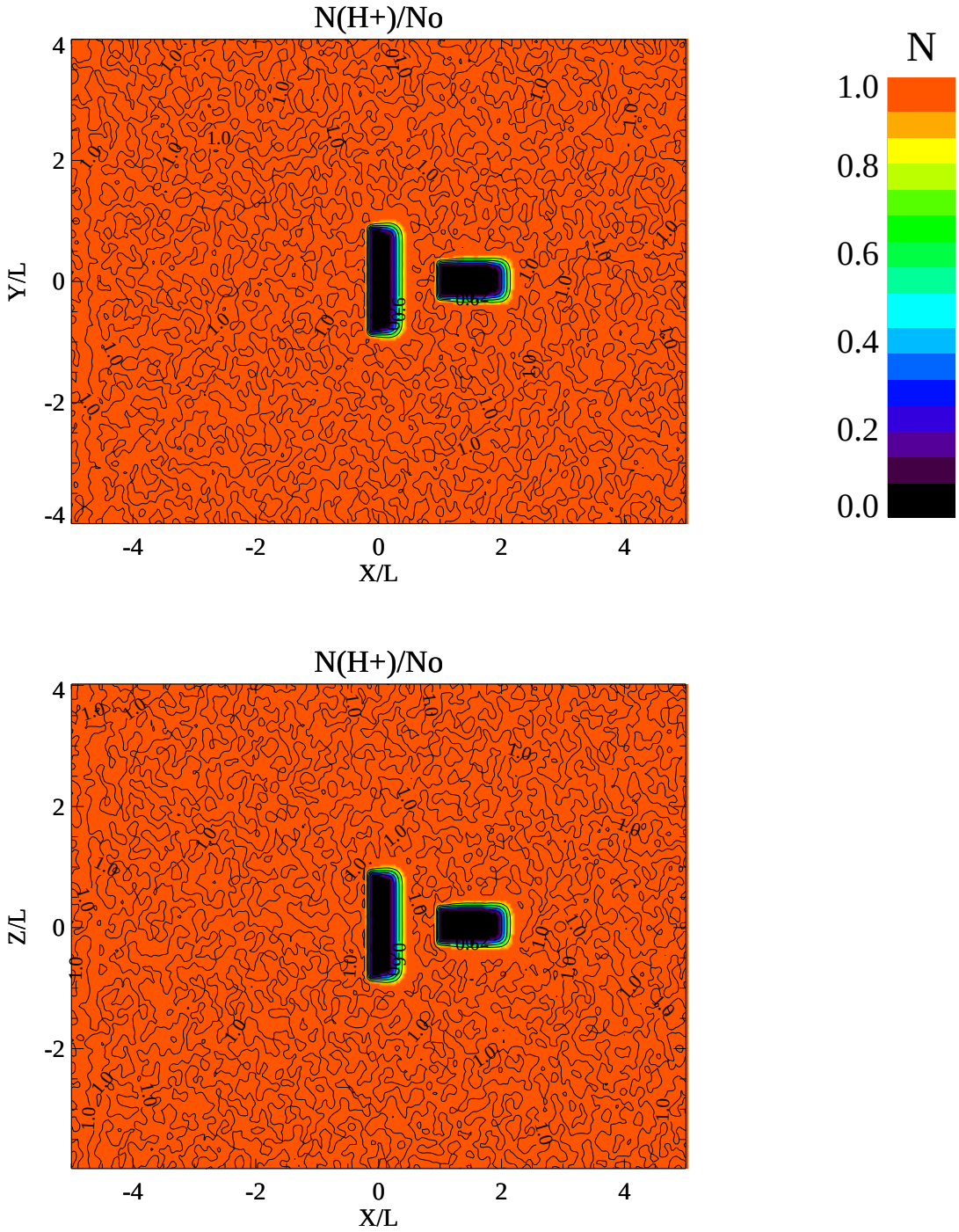

Figure 24. Solar wind ion density in the y-x ($z = 0$) and z-x ($y = 0$) planes. $U_0 = 200\,\mathrm{km/s}$, $M_A = 1.5$, $B_0 = 1500\,\mathrm{nT}$, $E_0 = U_0 B_0 = 0.3\,\mathrm{V/m}$, $n_{SW} = 5 \times 10^3\,\mathrm{cm}^{-3}$, $\beta_\mathrm{p} = 0.1$, $\beta_\mathrm{e} = 0.1$, $\theta_{bu} = 11^o$. Nonlinear saturation of the perturbations at $t = 0.29\,T_{ce}(0.04\,T_{transit})$ (case c).

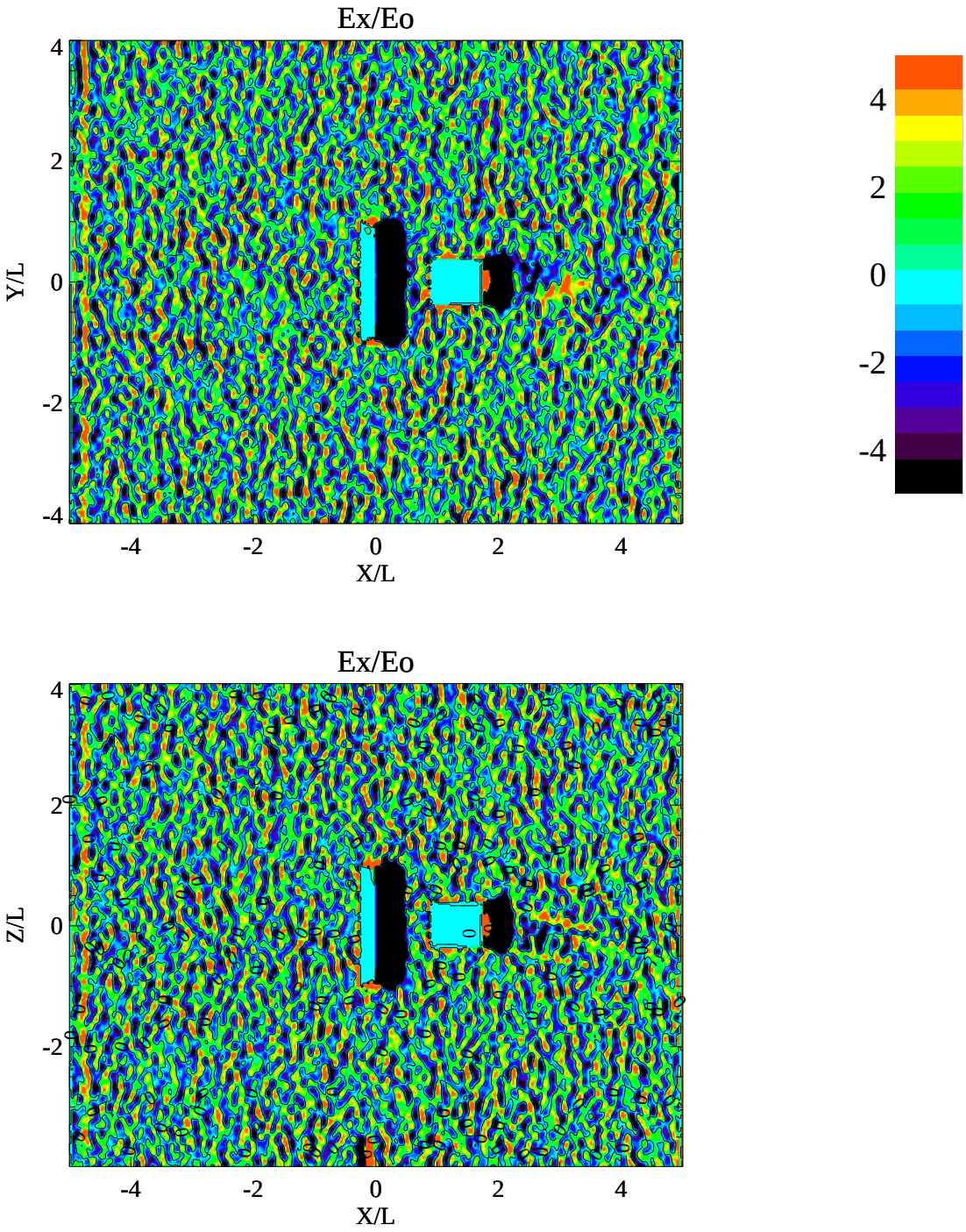

Figure 25. Electric field component $E_x(E_0)$ in the y-x ($z = 0$) and z-x ($y = 0$) planes. $U_0 = 200\,\mathrm{km/s}$, $M_A = 1.5$, $B_0 = 1500\,\mathrm{nT}$, $E_0 = U_0 B_0 = 0.3\,\mathrm{V/m}$, $n_{SW} = 5 \times 10^3\,\mathrm{cm}^{-3}$, $\beta_\mathrm{p} = 0.1$, $\beta_\mathrm{e} = 0.1$, $\theta_{bu} = 11^o$. Nonlinear saturation of the perturbations at $t = 0.104\,T_{ce}(0.013\,T_{transit})$ (case a).

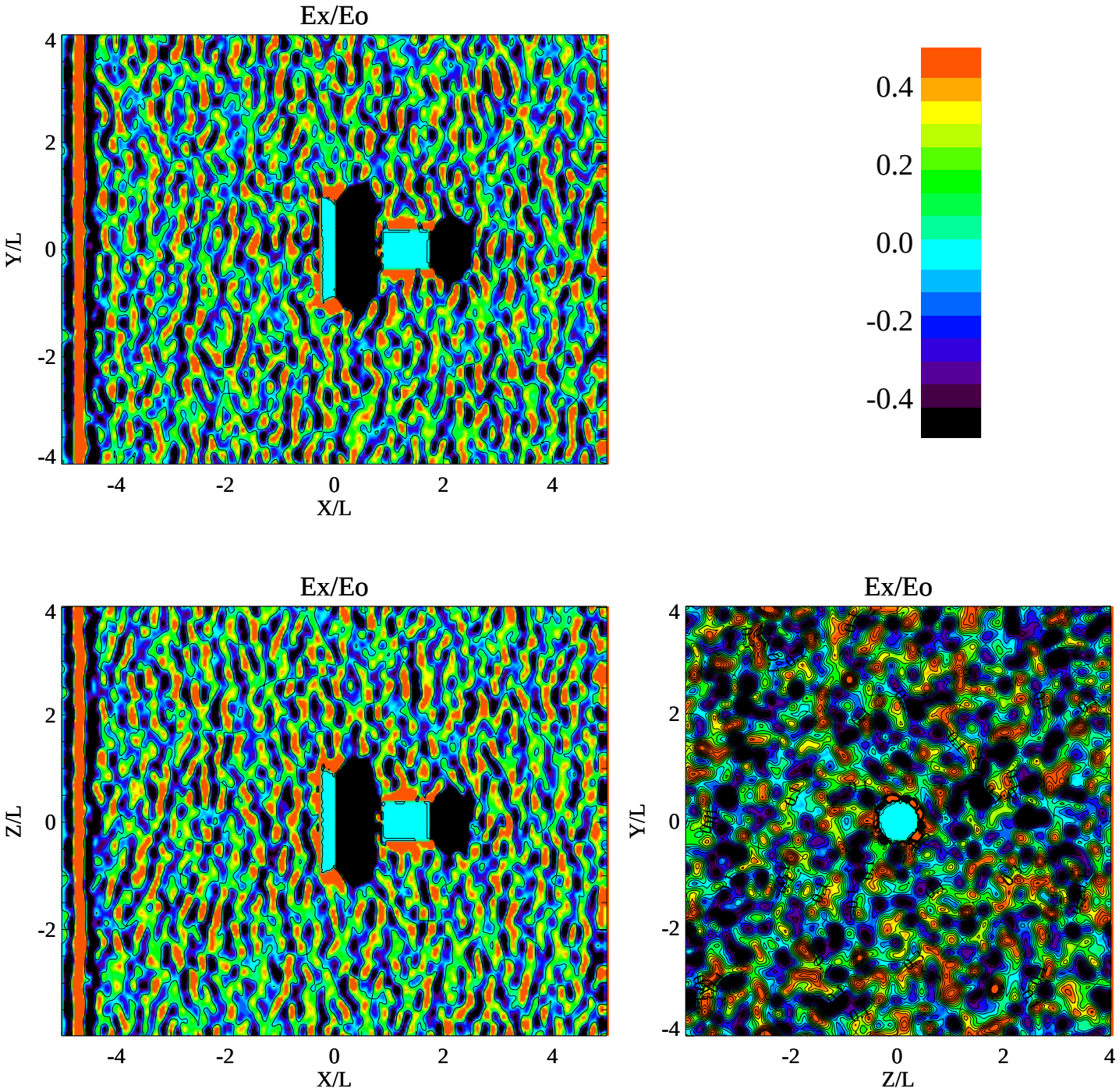

Figure 26. Electric field component $E_x(E_0)$ in the y-x ($z = 0$), z-x ($y = 0$) and y-z ($x = 0$) planes. $U_0 = 200\,\mathrm{km/s}$, $M_A = 1.5$, $B_0 = 1500\,\mathrm{nT}$, $E_0 = U_0 B_0 = 0.3\,\mathrm{V/m}$, $n_{SW} = 5 \times 10^3\,\mathrm{cm}^{-3}$, $\beta_\mathrm{p} = 0.1$, $\beta_\mathrm{e} = 0.1$, $\theta_{bu} = 11^o$. Nonlinear saturation of the perturbations at $t = 0.15\,T_{ce}(0.02\,T_{transit})$ (case b).

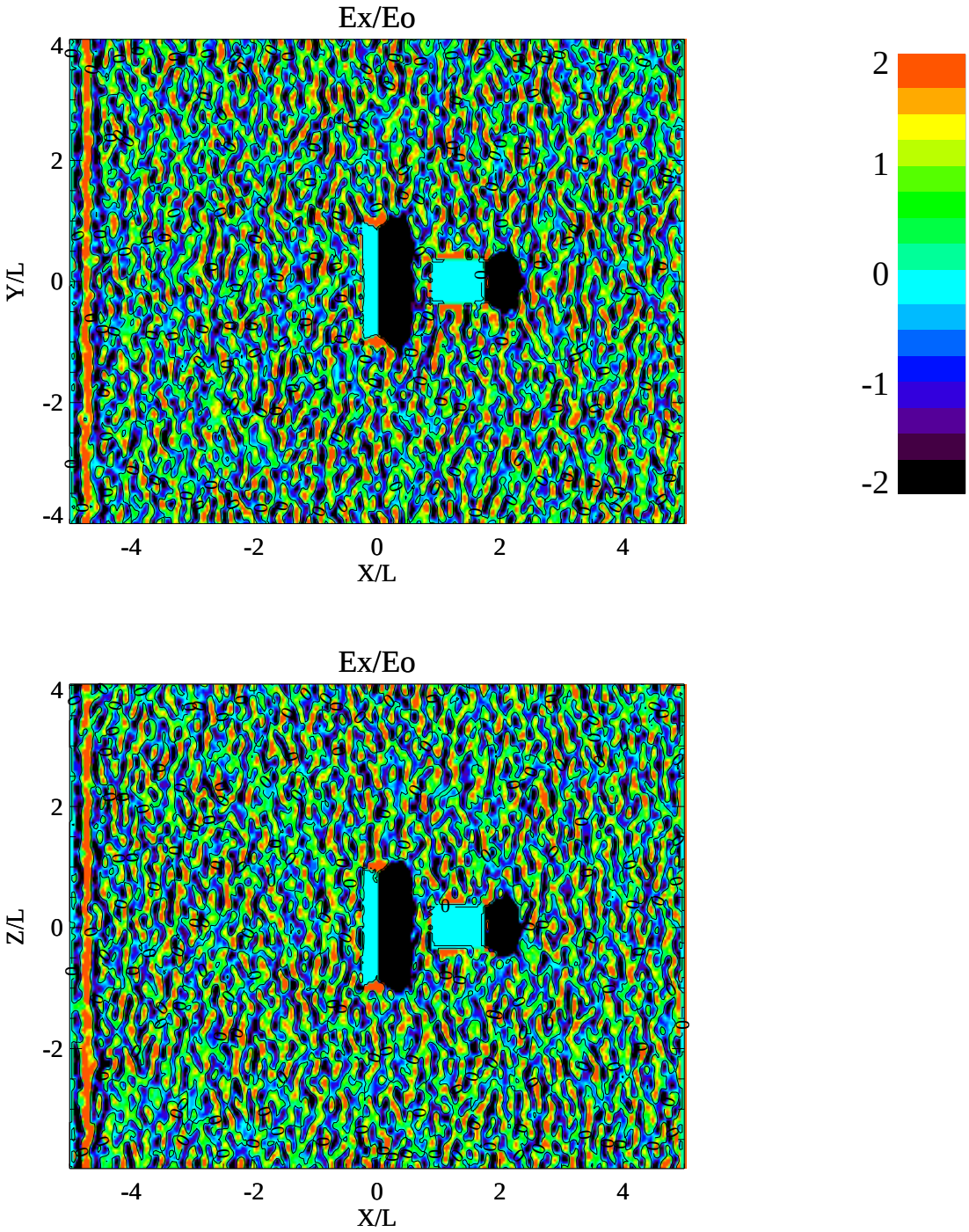

Figure 27. Electric field component $E_x(E_0)$ in the y-x ($z = 0$) and z-x ($y = 0$) planes. $U_0 = 200\,\mathrm{km/s}$, $M_A = 1.5$, $n_{SW} = 5 \times 10^3\,\mathrm{cm}^{-3}$, $\beta_\mathrm{p} = 0.1$, $\beta_\mathrm{e} = 0.1$, $\theta_{bu} = 11^o$. Nonlinear saturation of the perturbations at $t = 0.29\,T_{ce}(0.04\,T_{transit})$ (case c).

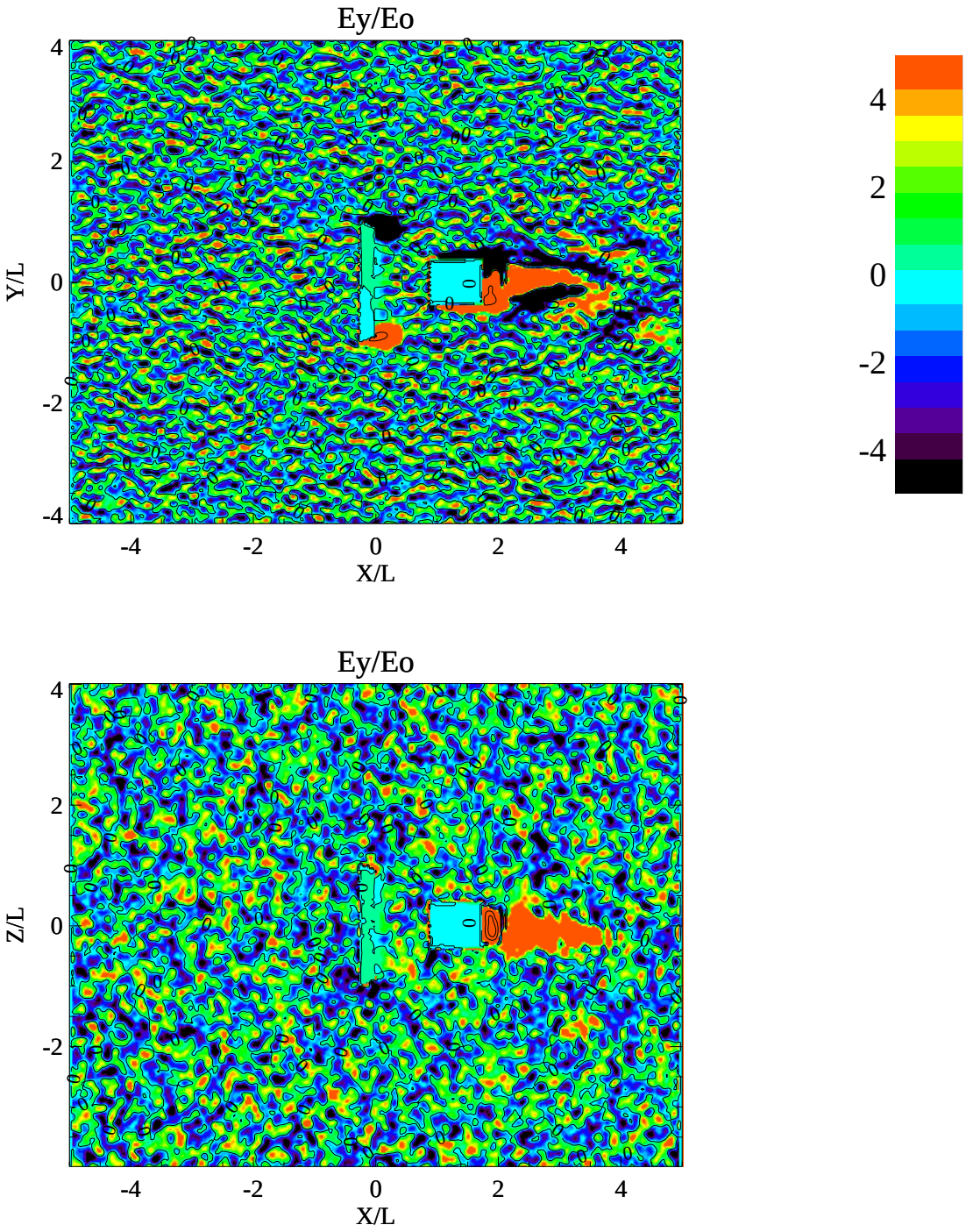

Figure 28. Electric field component $E_y(E_0)$ in the y-x ($z = 0$) and z-x ($y = 0$) planes. $U_0 = 200\,\mathrm{km/s}$, $M_A = 1.5$, $B_0 = 1500\,\mathrm{nT}$, $n = 5\times10^3\,\mathrm{cm}^{-3}$, $\beta_\mathrm{p} = 0.1$, $\beta_\mathrm{e} = 0.1$, $\theta_{bu} = 11^o$. Nonlinear saturation of the perturbations at $t = 0.104\,T_{ce}(0.013\,T_{transit})$ (case a).

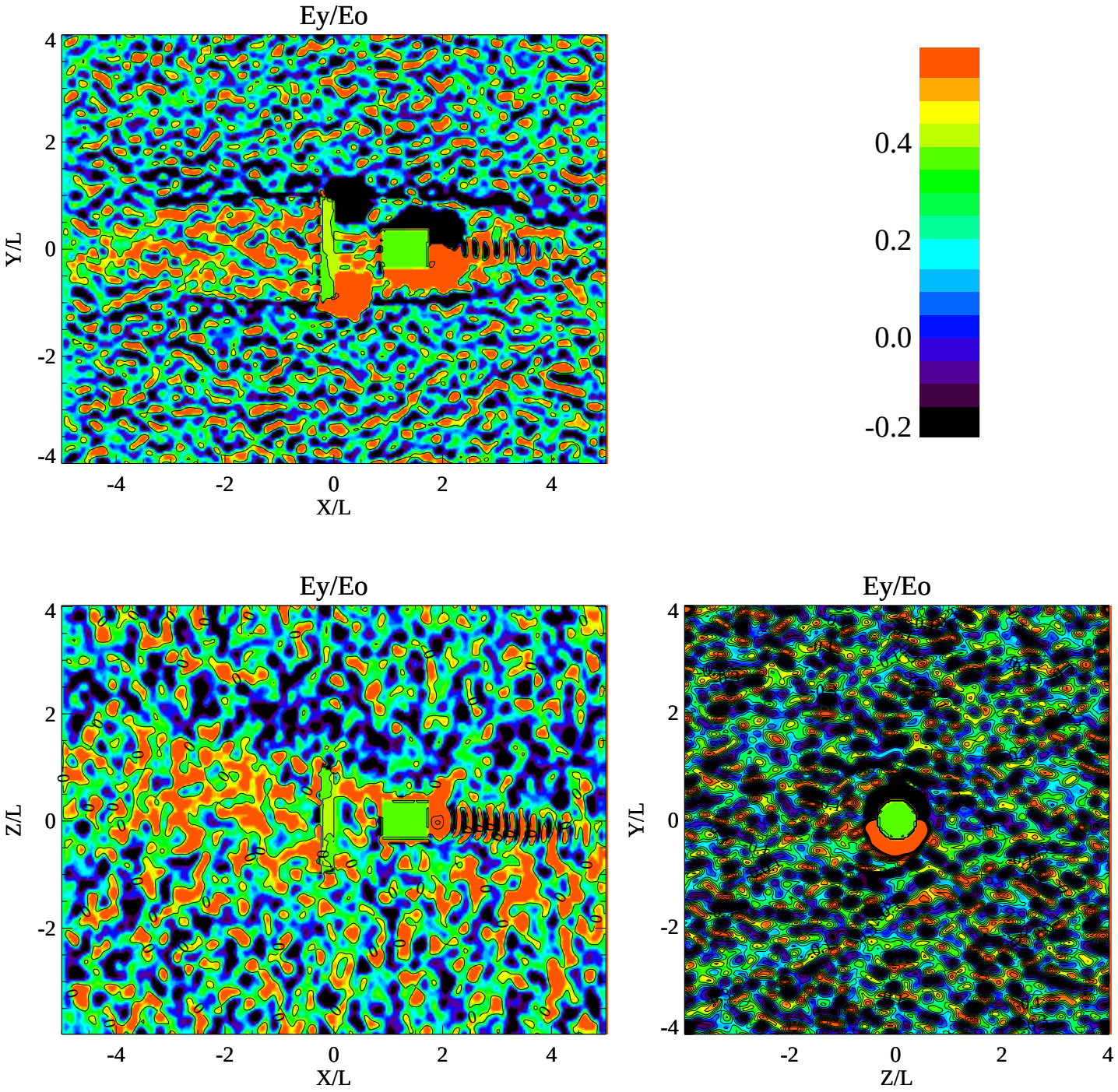

Figure 29. Electric field component $E_y(E_0)$ in the y-x ($z = 0$), z-x ($y = 0$) and y-z ($x = 0$) planes. $U_0 = 200\,\mathrm{km/s}$, $M_A = 1.5$, $B_0 = 1500\,\mathrm{nT}$, $n = 5 \times 10^3\,\mathrm{cm}^{-3}$, $\beta_\mathrm{p} = 0.1$, $\beta_\mathrm{e} = 0.1$, $\theta_{bu} = 11^o$. Nonlinear saturation of the perturbations at $t = 0.15\,T_{ce}(0.02\,T_{transit})$ (case b).

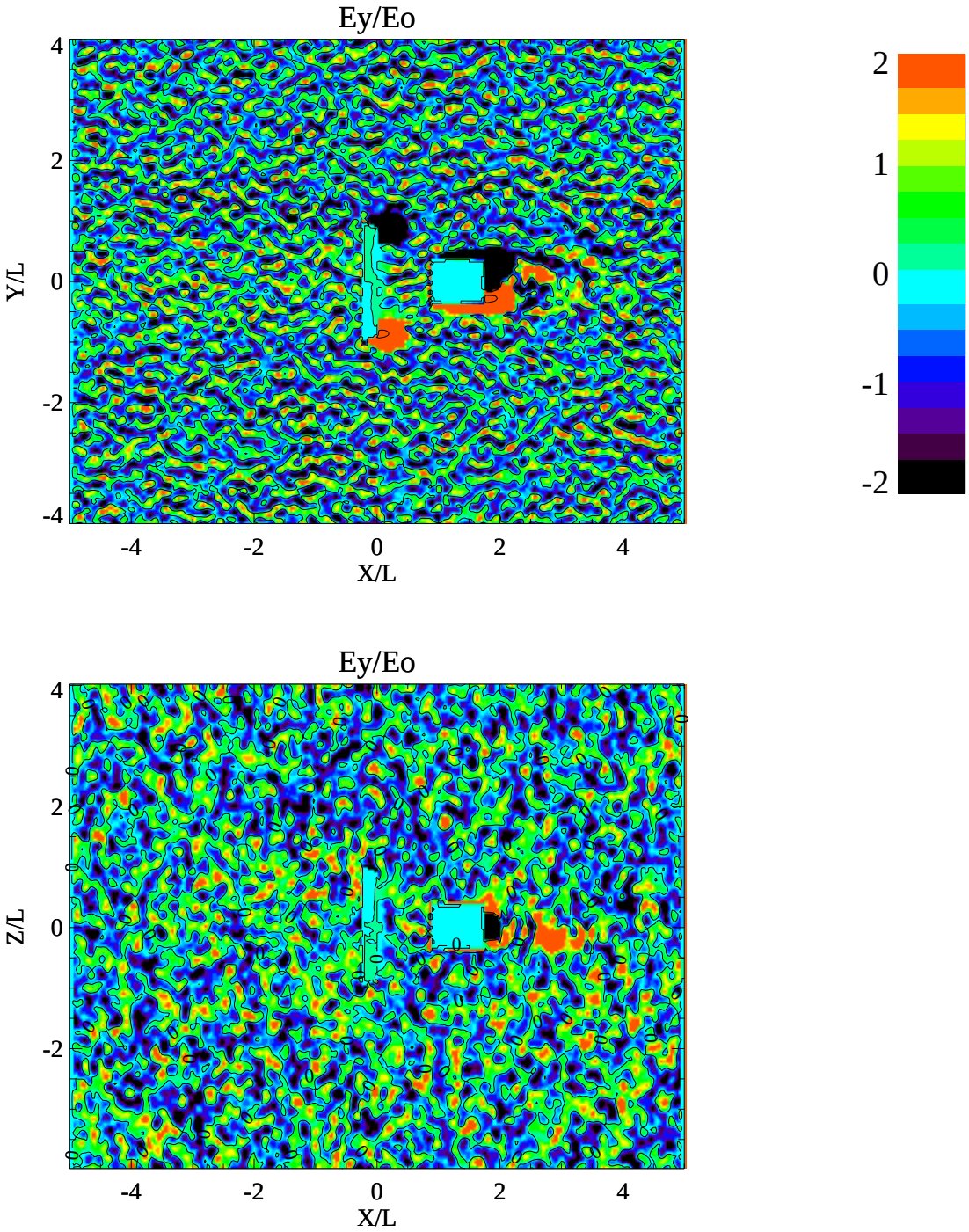

Figure 30. Electric field component $E_y(E_0)$ in the y-x ($z = 0$) and z-x ($y = 0$) planes. $U_0 = 200\,\mathrm{km/s}$, $M_A = 1.5$, $B_0 = 1500\,\mathrm{nT}$, $n = 5\times10^3\,\mathrm{cm}^{-3}$, $\beta_\mathrm{p} = 0.1$, $\beta_\mathrm{e} = 0.1$, $\theta_{bu} = 11^o$. Nonlinear saturation of the perturbations at $t = 0.29\,T_{ce}(0.04\,T_{transit})$ (case c).

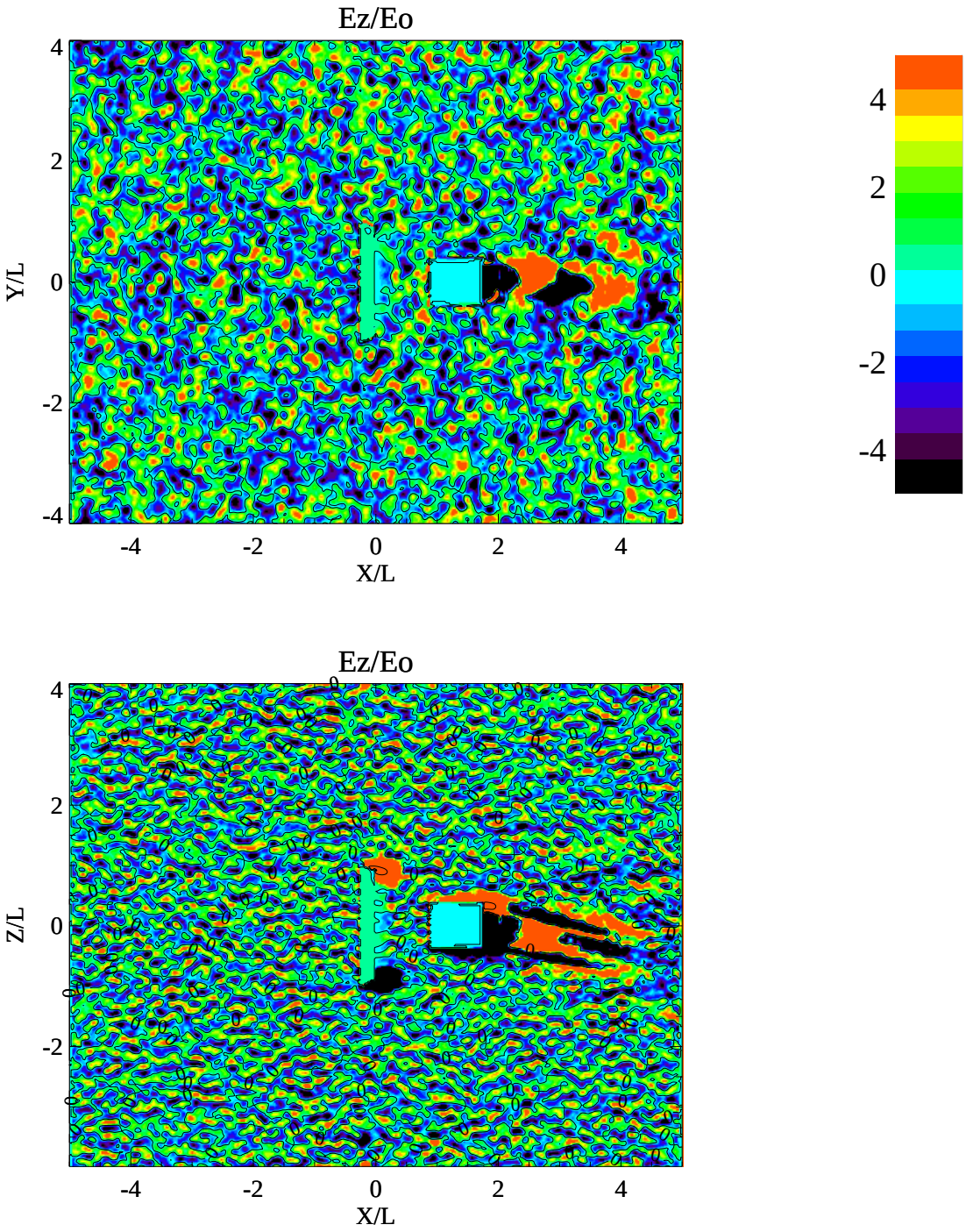

Figure 31. Electric field component $E_z(E_0)$ in the y-x ($z = 0$) and z-x ($y = 0$) planes. $U_0 = 200\,\mathrm{km/s}$, $M_A = 1.5$, $B_0 = 1500\,\mathrm{nT}$, $n = 5\times10^3\,\mathrm{cm}^{-3}$, $\beta_\mathrm{p} = 0.1$, $\beta_\mathrm{e} = 0.1$, $\theta_{bu} = 11^o$. Nonlinear saturation of the perturbations at $t = 0.104\,T_{ce}(0.013\,T_{transit})$ (case a).

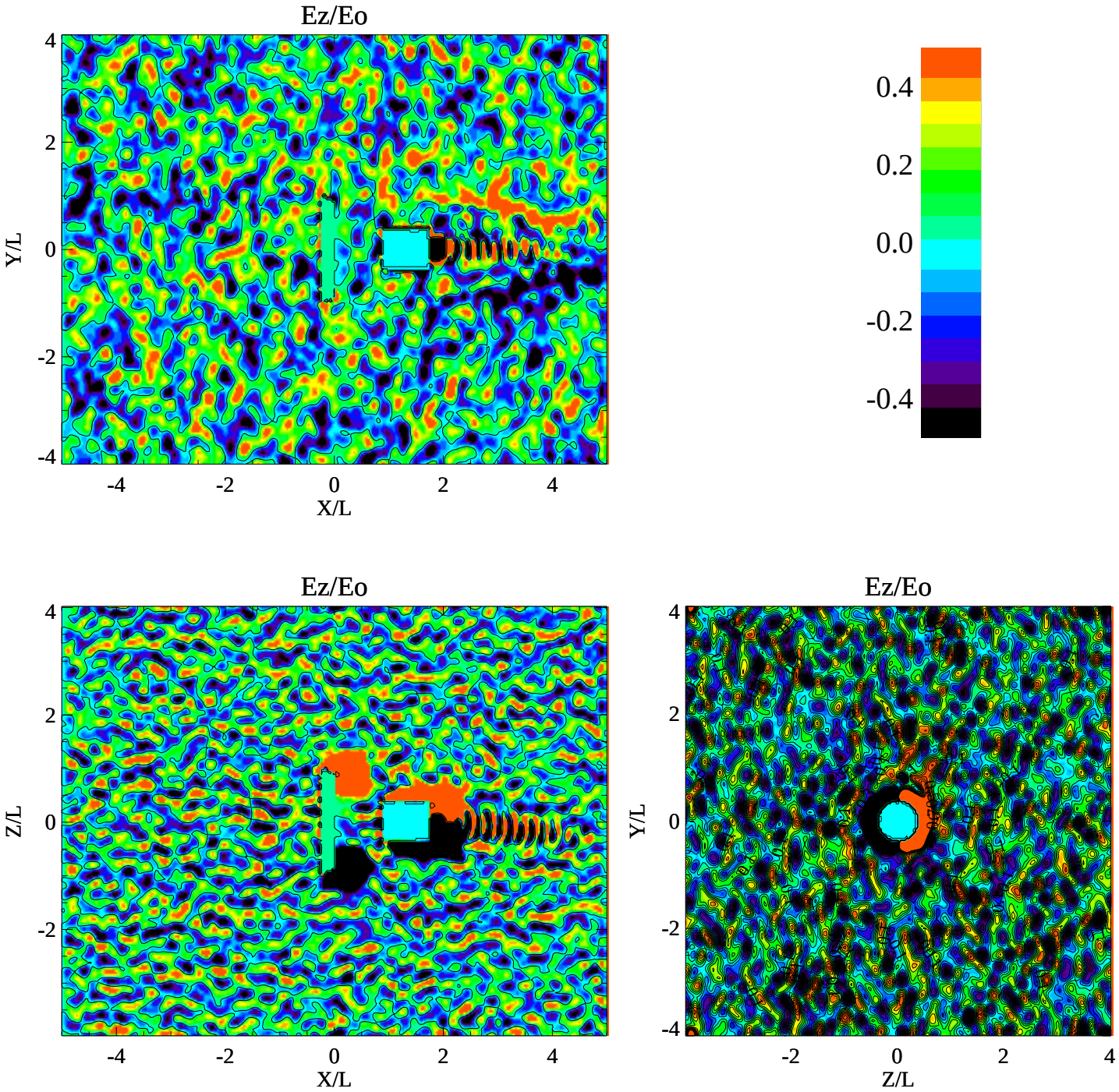

Figure 32. Electric field component $E_z(E_0)$ in the y-x ($z = 0$), z-x ($y = 0$) and y-z ($x = 0$) planes. $U_0 = 200\,\mathrm{km/s}$, $M_A = 1.5$, $n = 5 \times 10^3\,\mathrm{cm}^{-3}$, $\beta_\mathrm{p} = 0.1$, $\beta_\mathrm{e} = 0.1$, $\theta_{bu} = 11^o$. Nonlinear saturation of the perturbations at $t = 0.15\,T_{ce}(0.02\,T_{transit})$ (case b).

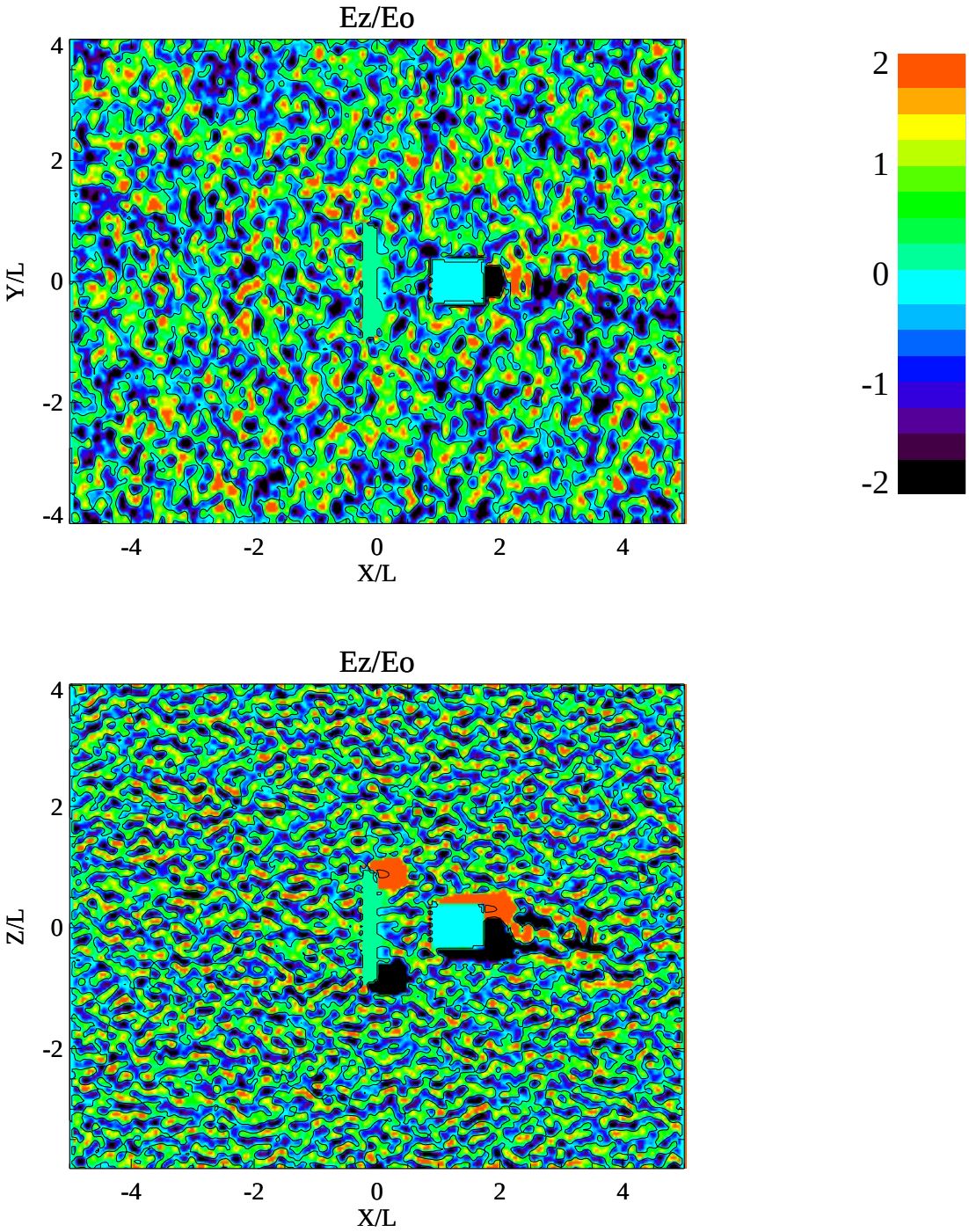

Figure 33. Electric field component $E_z(E_0)$ in the y-x ($z = 0$) and z-x ($y = 0$) planes. $U_0 = 200\,\mathrm{km/s}$, $M_A = 1.5$, $B_0 = 1500\,\mathrm{nT}$, $n = 5\times10^3\,\mathrm{cm}^{-3}$, $\beta_\mathrm{p} = 0.1$, $\beta_\mathrm{e} = 0.1$, $\theta_{bu} = 11^o$. Nonlinear saturation of the perturbations at $t = 0.29\,T_{ce}(0.04\,T_{transit})$ (case c).

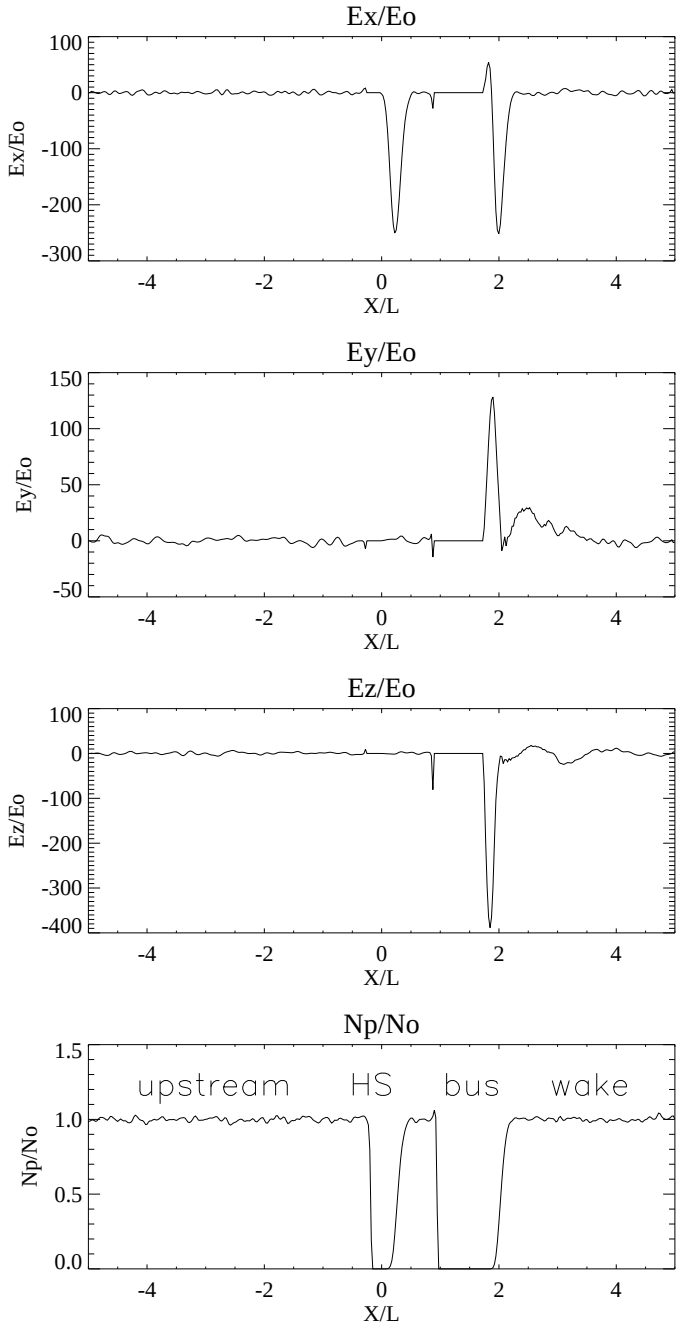

Figure 34. 1-D cuts for the electric field component $E_x(E_0)$, $E_y(E_0)$ and $E_z(E_0)$ ($y = 0$, $z = 0$). $U_0 = 200\,\mathrm{km/s}$, $M_A = 1.5$, $B_0 = 1500\,\mathrm{nT}$, $n = 5 \times 10^3\,\mathrm{cm}^{-3}$, $\beta_\mathrm{p} = 0.1$, $\beta_\mathrm{e} = 0.1$, $\theta_{bu} = 11^o$. Nonlinear saturation of the perturbations at $t = 0.104\,T_{ce}(0.013\,T_{transit})$ (case a).

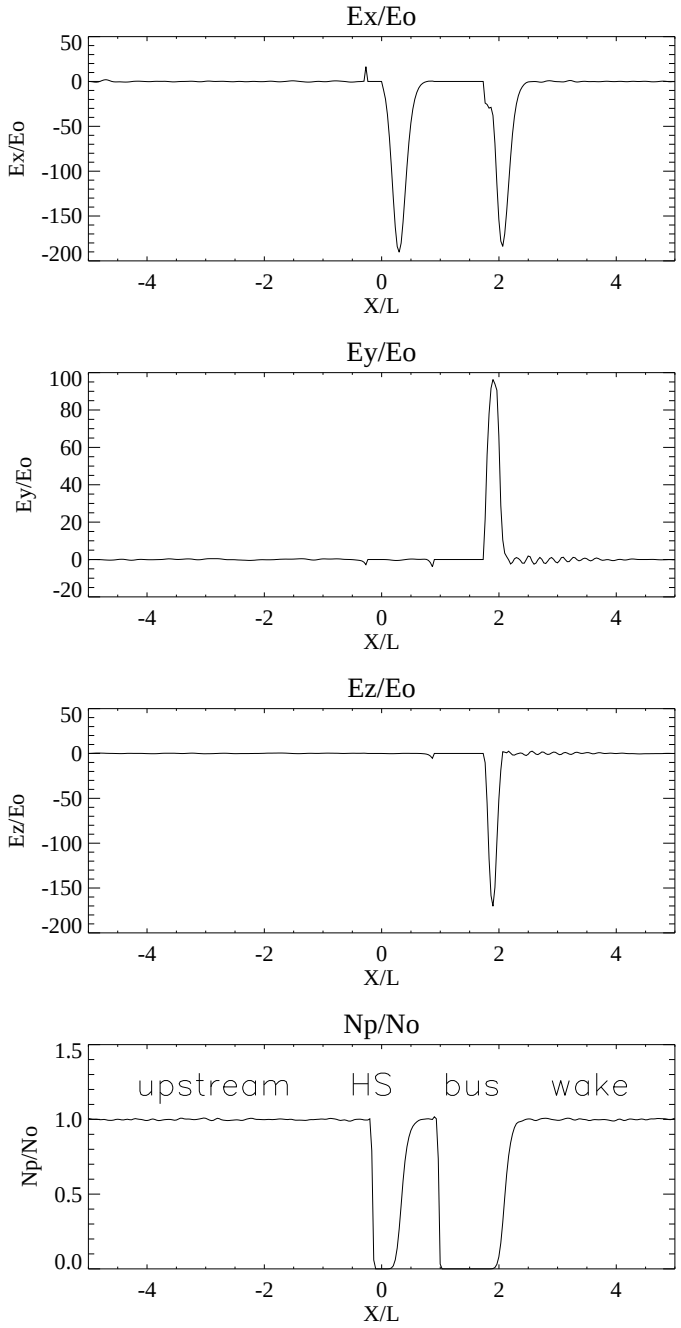

Figure 35. 1-D cuts for the electric field component $E_x(E_0)$, $E_y(E_0)$ and $E_z(E_0)$ ($y = 0$, $z = 0$). $U_0 = 200\,\mathrm{km/s}$, $M_A = 1.5$, $n = 5 \times 10^3\,\mathrm{cm}^{-3}$, $\beta_\mathrm{p} = 0.1$, $\beta_\mathrm{e} = 0.1$, $\theta_{bu} = 11^o$. Nonlinear saturation of the perturbations at $t = 0.15\,T_{ce}(0.02\,T_{transit})$ (case b).

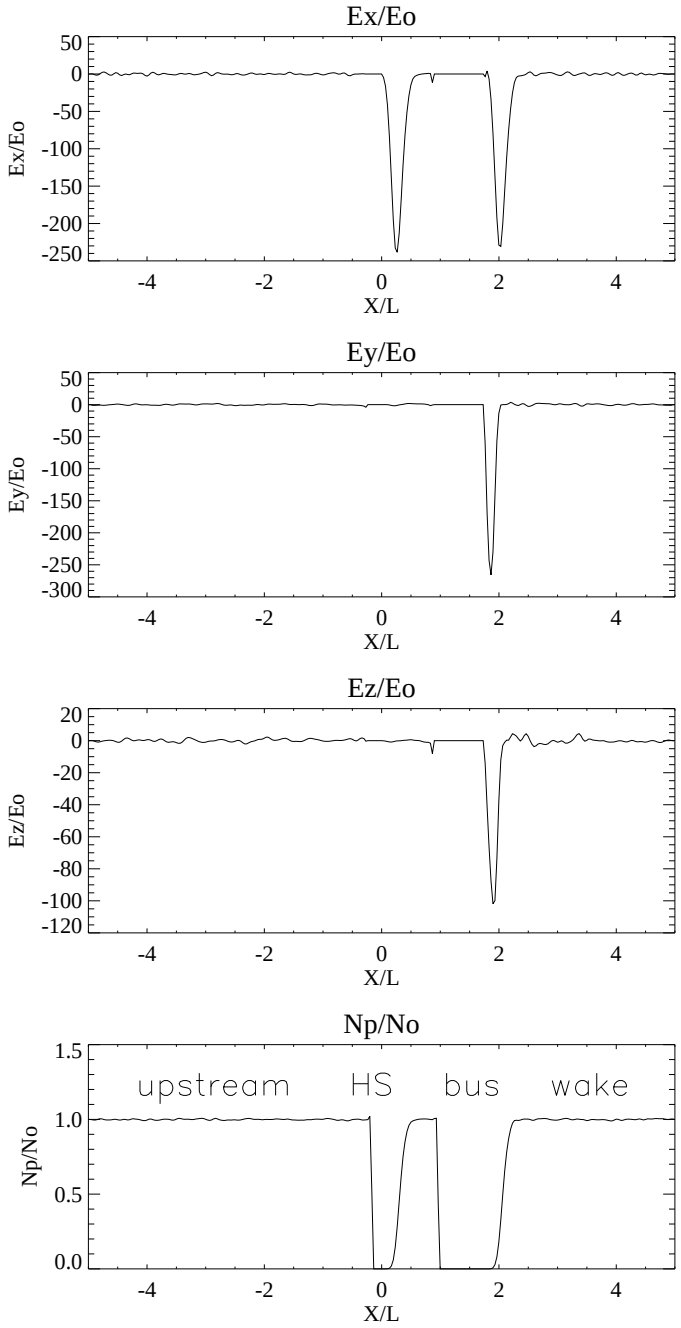

Figure 36. 1-D cuts for the electric field component $E_x(E_0)$, $E_y(E_0)$ and $E_z(E_0)$ ($y = 0$, $z = 0$). $U_0 = 200\,\mathrm{km/s}$, $M_A = 1.5$, $B_0 = 1500\,\mathrm{nT}$, $n = 5 \times 10^3\,\mathrm{cm}^{-3}$, $\beta_\mathrm{p} = 0.1$, $\beta_\mathrm{e} = 0.1$, $\theta_{bu} = 11^o$. Nonlinear saturation of the perturbations at $t = 0.29\,T_{ce}(0.04\,T_{transit})$ (case c).

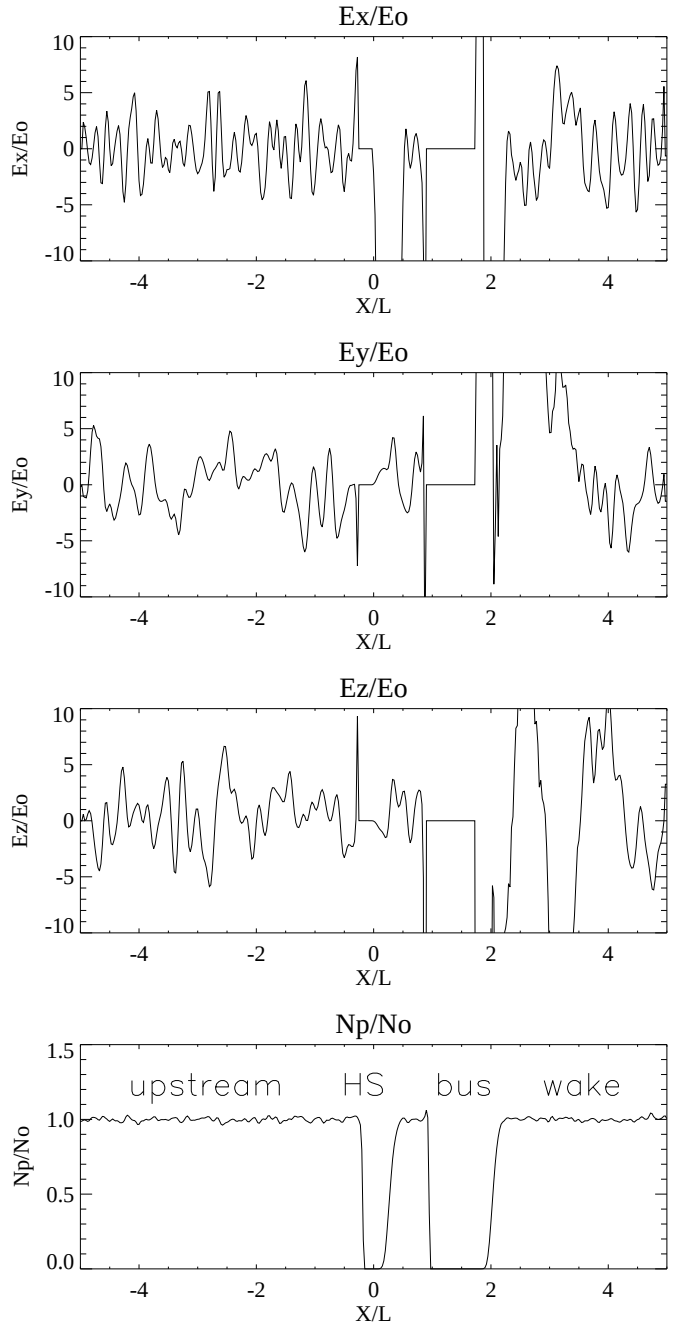

Figure 37. 1-D cuts for the electric field component $E_x(E_0)$, $E_y(E_0)$ and $E_z(E_0)$ ($y = 0$, $z = 0$). $U_0 = 200\,\mathrm{km/s}$, $M_A = 1.5$, $B_0 = 1500\,\mathrm{nT}$, $n = 5 \times 10^3\,\mathrm{cm}^{-3}$, $\beta_\mathrm{p} = 0.1$, $\beta_\mathrm{e} = 0.1$, $\theta_{bu} = 11^o$. Nonlinear saturation of the perturbations at $t = 0.104\,T_{ce}(0.013\,T_{transit})$ (case a).

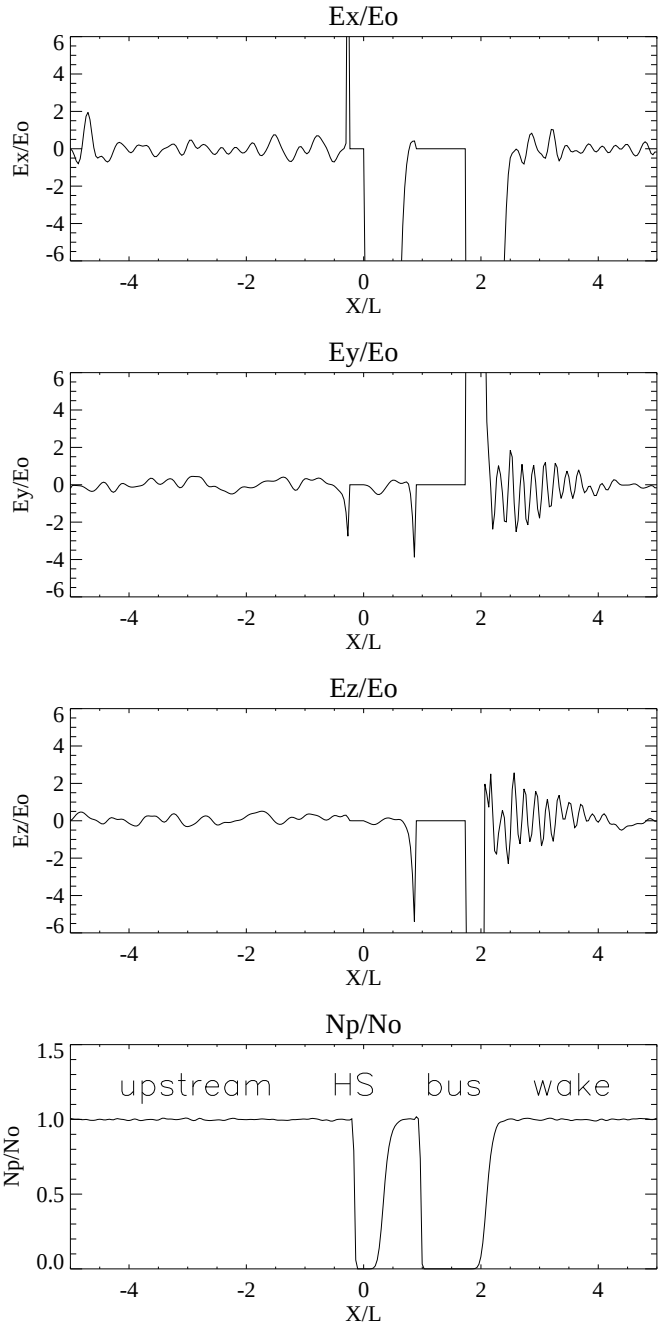

Figure 38. 1-D cuts for the electric field component $E_x(E_0)$, $E_y(E_0)$ and $E_z(E_0)$ ($y = 0$, $z = 0$). $U_0 = 200\,\mathrm{km/s}$, $M_A = 1.5$, $n = 5 \times 10^3\,\mathrm{cm}^{-3}$, $\beta_\mathrm{p} = 0.1$, $\beta_\mathrm{e} = 0.1$, $\theta_{bu} = 11^o$. Nonlinear saturation of the perturbations at $t = 0.15\,T_{ce}(0.02\,T_{transit})$ (case b).

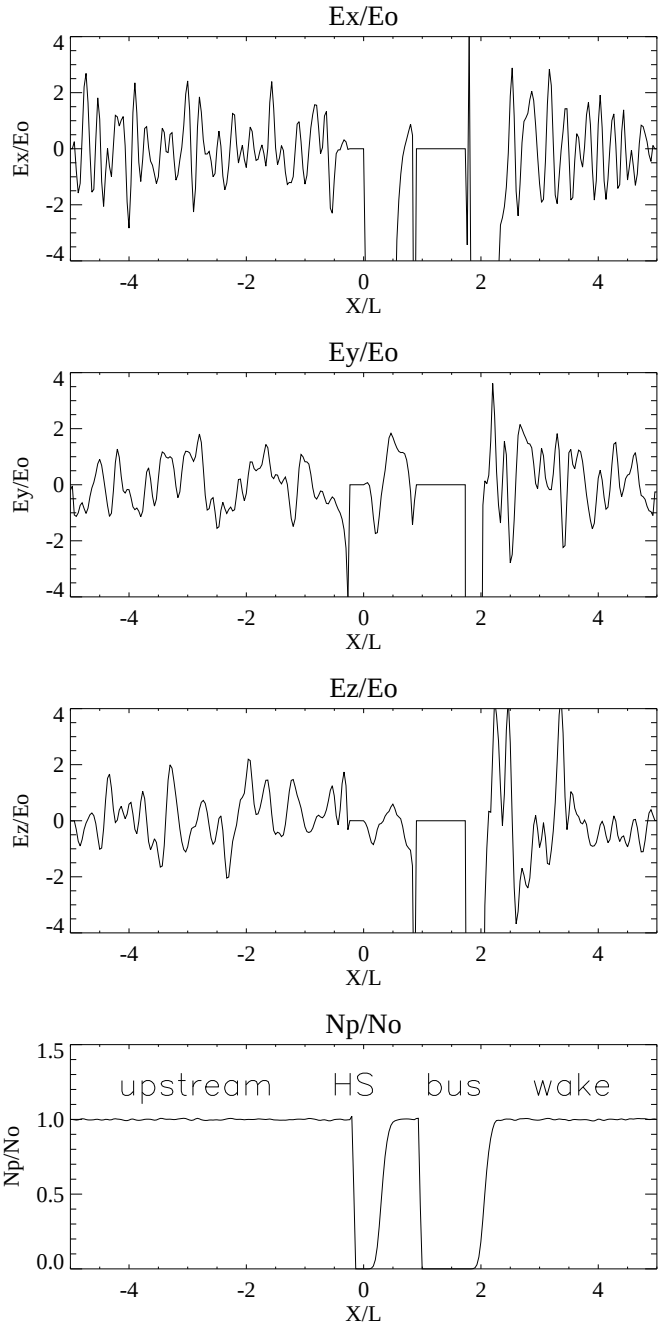

Figure 39. 1-D cuts for the electric field component $E_x(E_0)$, $E_y(E_0)$ and $E_z(E_0)$ ($y = 0$, $z = 0$). $U_0 = 200\,\mathrm{km/s}$, $M_A = 1.5$, $B_0 = 1500\,\mathrm{nT}$, $n = 5 \times 10^3\,\mathrm{cm}^{-3}$, $\beta_\mathrm{p} = 0.1$, $\beta_\mathrm{e} = 0.1$, $\theta_{bu} = 11^o$. Nonlinear saturation of the perturbations at $t = 0.29\,T_{ce}(0.04\,T_{transit})$ (case c).

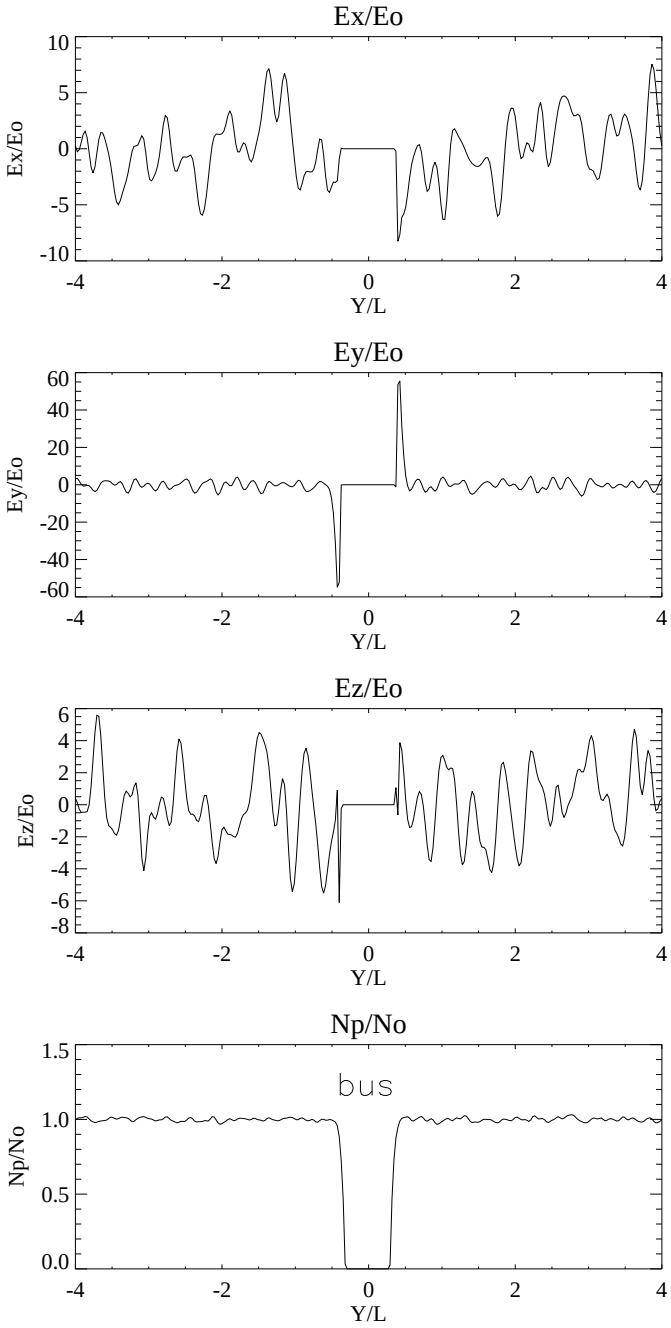

Figure 40. 1-D cuts for the electric field component $E_x(E_0$, $E_y(E_0)$ and $E_z(E_0)$ ($x = 1.5$, $z = 0$). $U_0 = 200\,\mathrm{km/s}$, $M_A = 1.5$, $B_0 = 1500\,\mathrm{nT}$, $n = 5 \times 10^3\,\mathrm{cm}^{-3}$, $\beta_\mathrm{p} = 0.1$, $\beta_\mathrm{e} = 0.1$, $\theta_{bu} = 11^o$. Nonlinear saturation of the perturbations at $t = 0.104\,T_{ce}(0.013\,T_{transit})$ (case a).

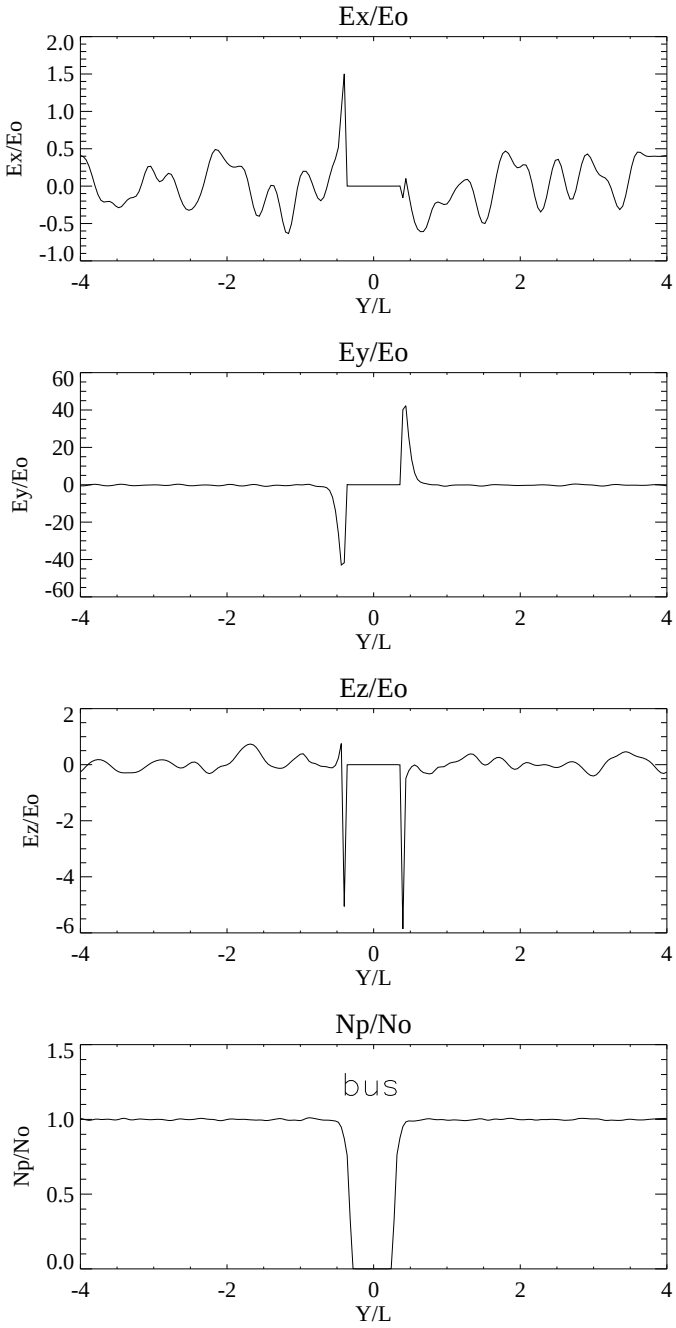

Figure 41. 1-D cuts for the electric field component $E_x(E_0)$, $E_y(E_0)$ and $E_z(E_0)$ ($x = 1.5$, $z = 0$). $U_0 = 200\,\mathrm{km/s}$, $M_A = 1.5$, $n = 5 \times 10^3\,\mathrm{cm}^{-3}$, $\beta_\mathrm{p} = 0.1$, $\beta_\mathrm{e} = 0.1$, $\theta_{bu} = 11^o$. Nonlinear saturation of the perturbations at $t = 0.15\,T_{ce}(0.02\,T_{transit})$ (case b).

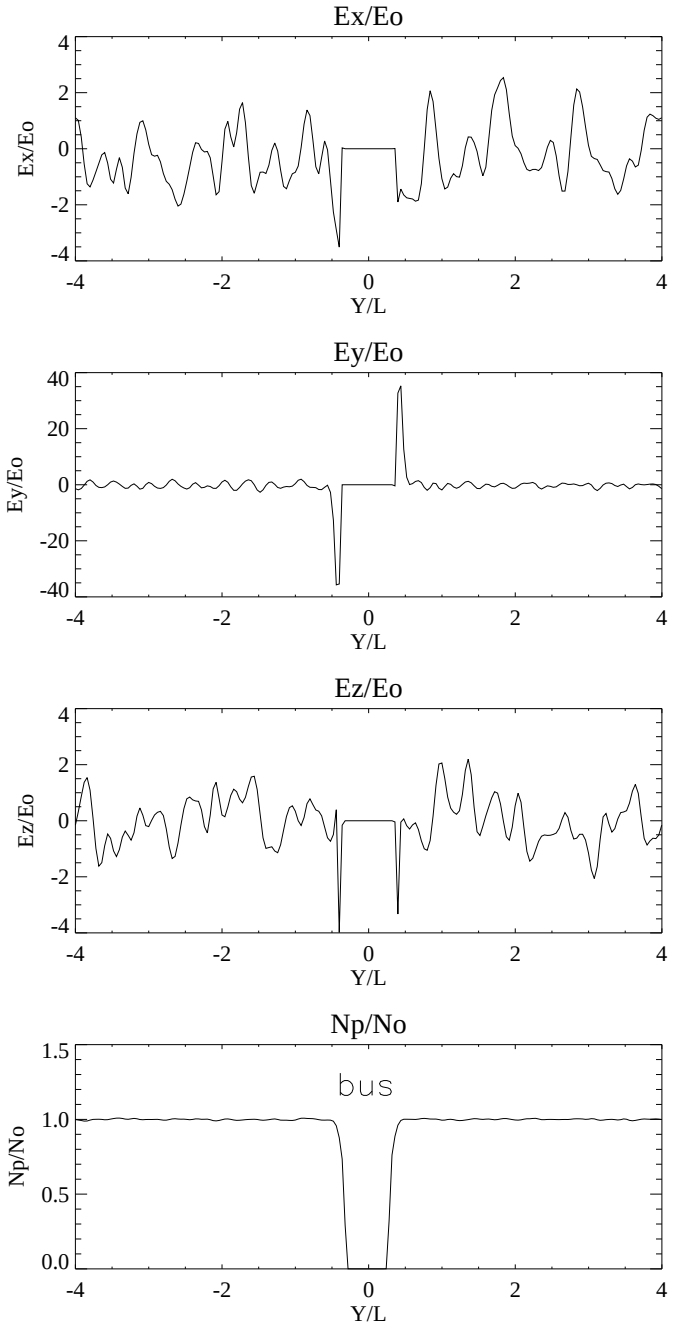

Figure 42. 1-D cuts for the electric field component $E_x(E_0)$, $E_y(E_0)$ and $E_z(E_0)$ ($x = 1.5,\ z = 0$). $U_0 = 200\,\mathrm{km/s},\ M_A = 1.5,\ B_0 = 1500\,\mathrm{nT},\ n = 5 \times 10^3\,\mathrm{cm}^{-3},\ \beta_\mathrm{p} = 0.1,\ \beta_\mathrm{e} = 0.1,\ \theta_{bu} = 11^o$. Nonlinear saturation of the perturbations at $t = 0.29\,T_{ce}(0.04\,T_{transit})$ (case c).

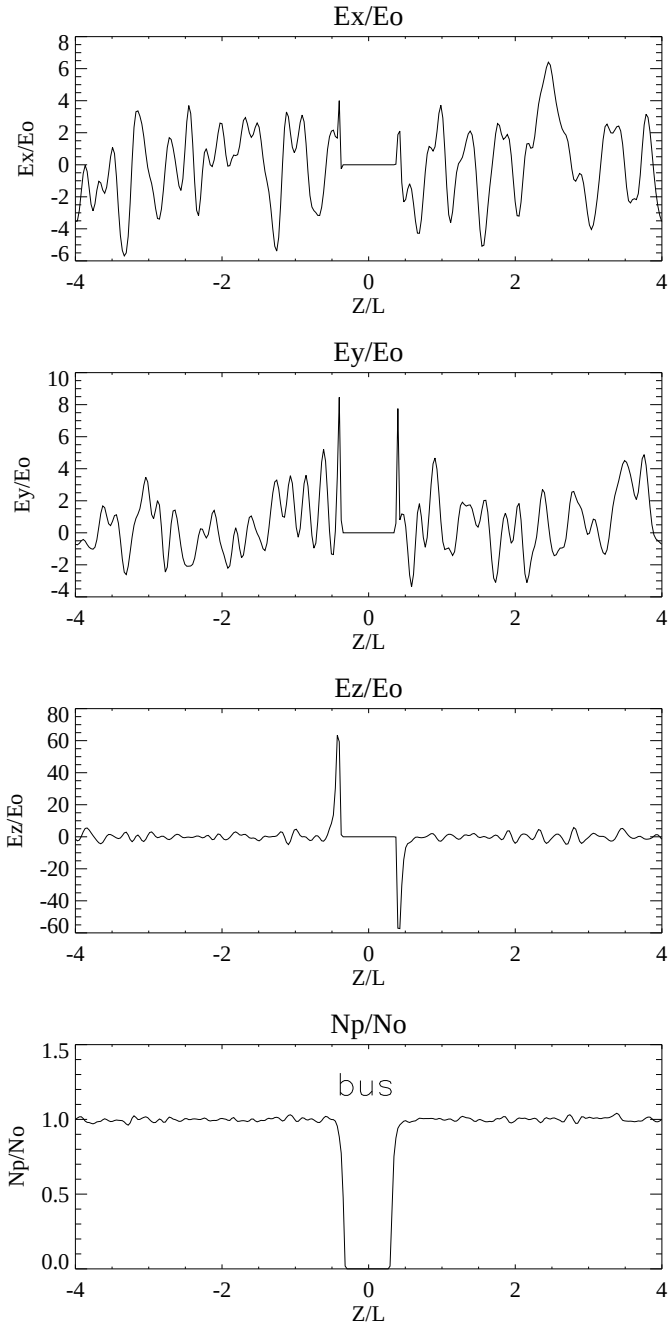

Figure 43. 1-D cuts for the electric field component $E_x(E_0)$, $E_y(E_0)$ and $E_z(E_0)$ ($x = 1.5$, $y = 0$). $U_0 = 200\,\mathrm{km/s}$, $M_A = 1.5$, $B_0 = 1500\,\mathrm{nT}$, $n = 5 \times 10^3\,\mathrm{cm}^{-3}$, $\beta_\mathrm{p} = 0.1$, $\beta_\mathrm{e} = 0.1$, $\theta_{bu} = 11^o$. Nonlinear saturation of the perturbations at $t = 0.104\,T_{ce}(0.013\,T_{transit})$ (case a).

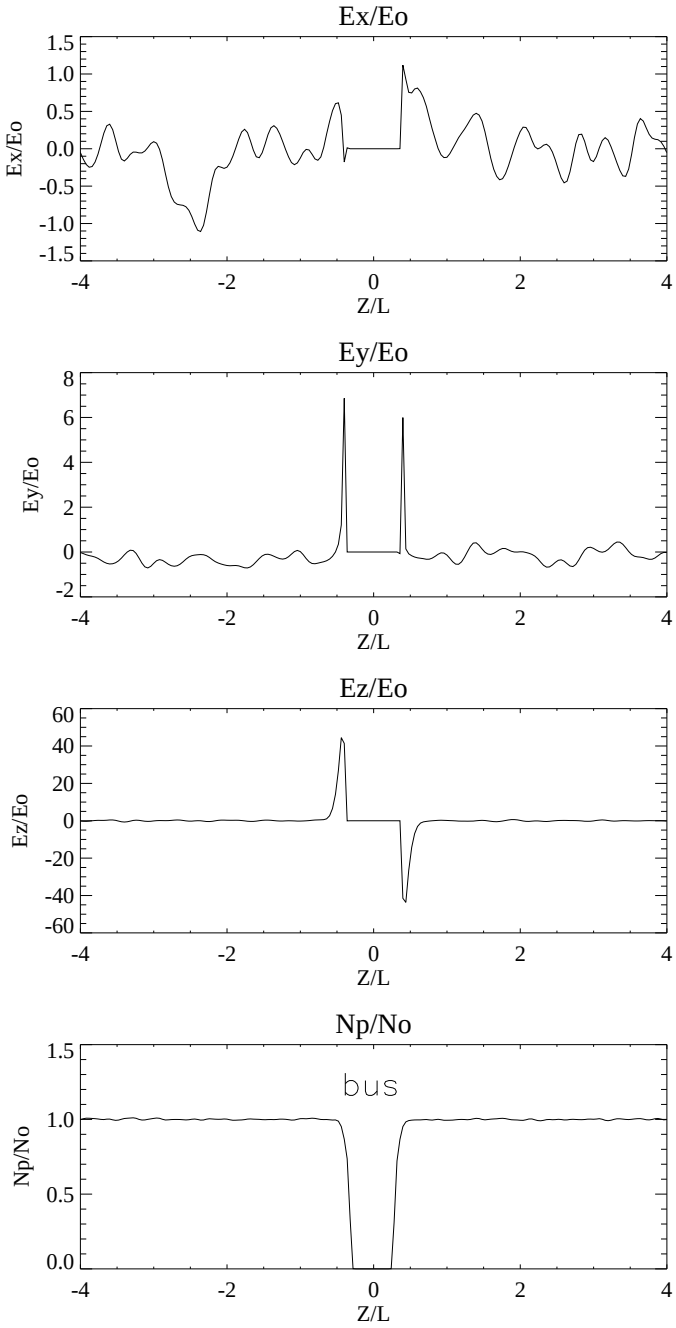

Figure 44. 1-D cuts for the electric field component $E_x(E_0)$, $E_y(E_0)$ and $E_z(E_0)$ ($x = 1.5$, $y = 0$). $U_0 = 200\,\mathrm{km/s}$, $M_A = 1.5$, $n = 5 \times 10^3\,\mathrm{cm}^{-3}$, $\beta_\mathrm{p} = 0.1$, $\beta_\mathrm{e} = 0.1$, $\theta_{bu} = 11^o$. Nonlinear saturation of the perturbations at $t = 0.15\,T_{ce}(0.02\,T_{transit})$ (case b).

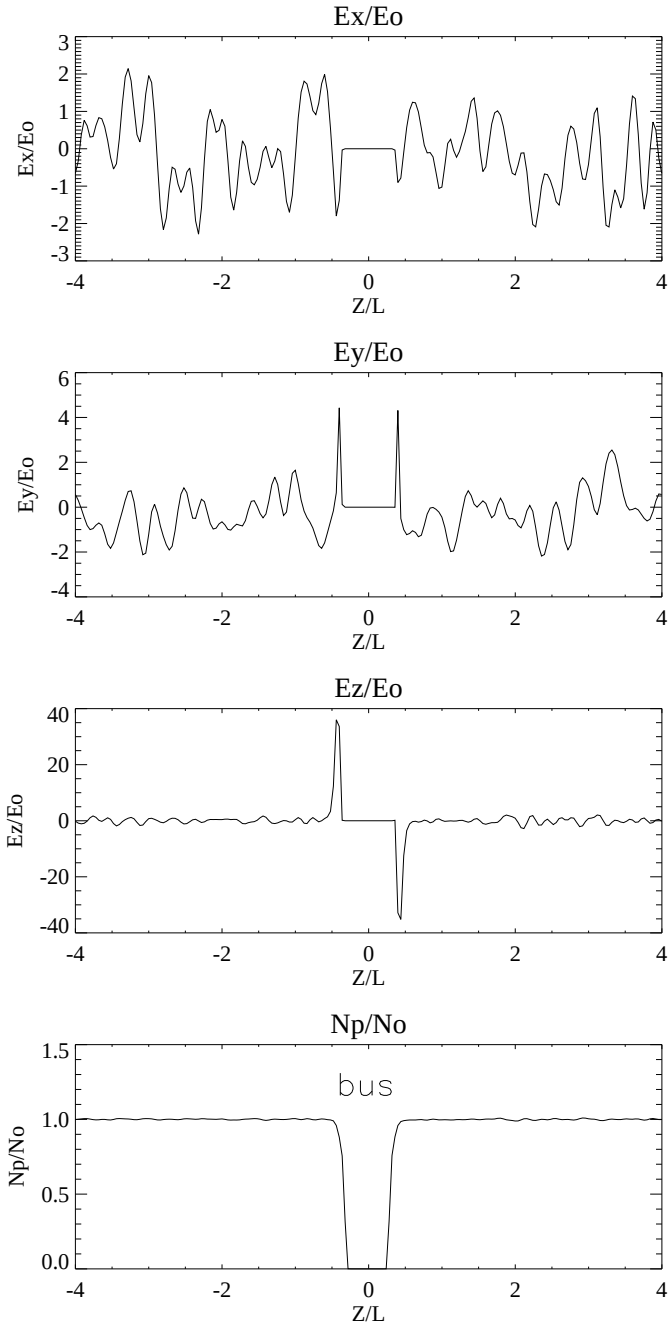

Figure 45. 1-D cuts for the electric field component $E_x(E_0)$, $E_y(E_0$ and $E_z(E_0)$ ($x = 1.5$, $y = 0$). $U_0 = 200\,\mathrm{km/s}$, $M_A = 1.5$, $B_0 = 1500\,\mathrm{nT}$, $n = 5 \times 10^3\,\mathrm{cm}^{-3}$, $\beta_\mathrm{p} = 0.1$, $\beta_\mathrm{e} = 0.1$, $\theta_{bu} = 11^o$. Nonlinear saturation of the perturbations at $t = 0.29\,T_{ce}(0.04\,T_{transit})$ (case c).

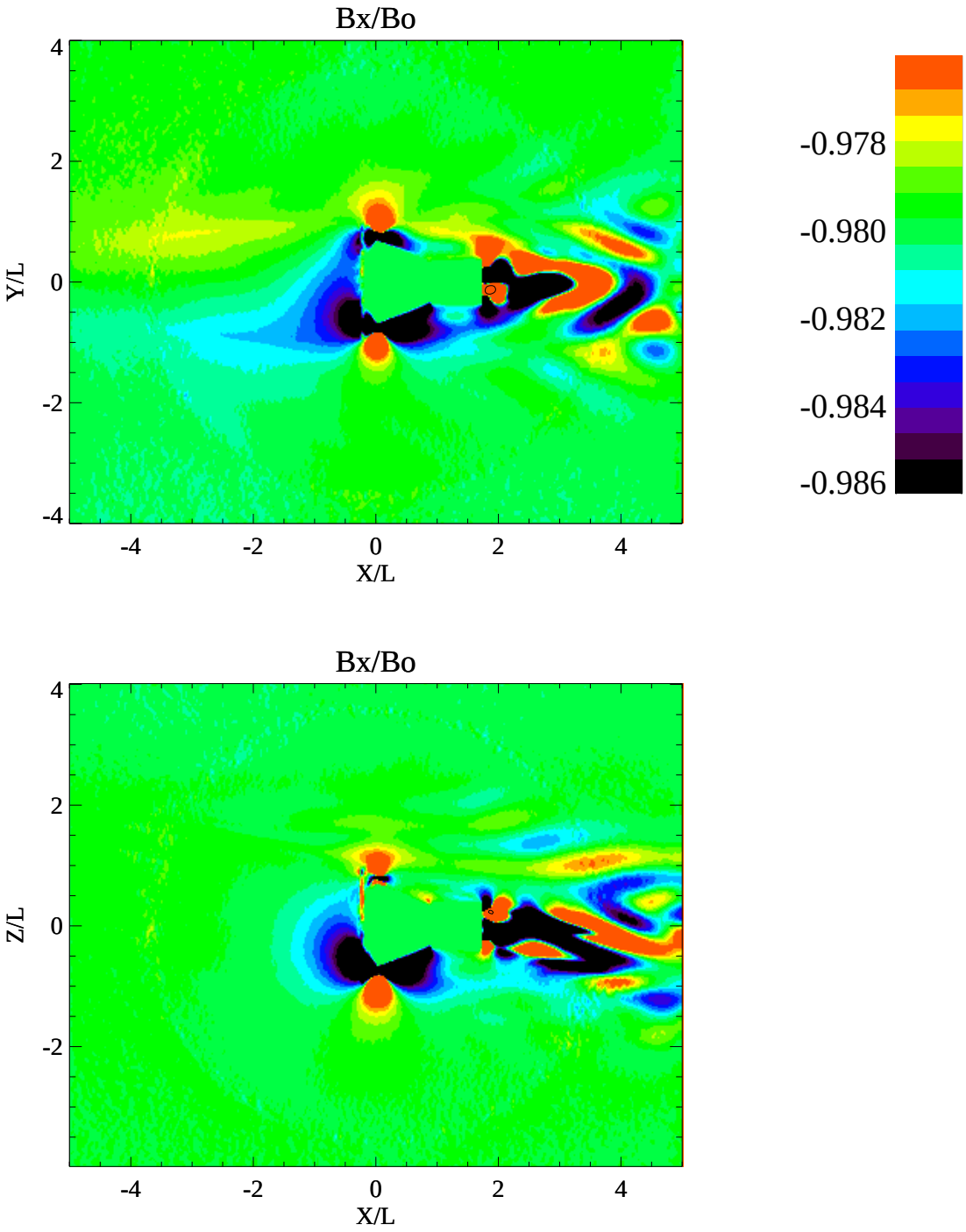

Figure 46. Magnetic field component $B_x(B_0)$ in the y-x ($z = 0$) and z-x ($y = 0$) planes. $U_0 = 200\,\mathrm{km/s}$, $M_A = 1.5$, $B_0 = 1500\,\mathrm{nT}$, $n = 5\times10^3\,\mathrm{cm}^{-3}$, $\beta_\mathrm{p} = 0.1$, $\beta_\mathrm{e} = 0.1$, $\theta_{bu} = 11^o$. Nonlinear saturation of the perturbations at $t = 0.104\,T_{ce}(0.013\,T_{transit})$ (case a).

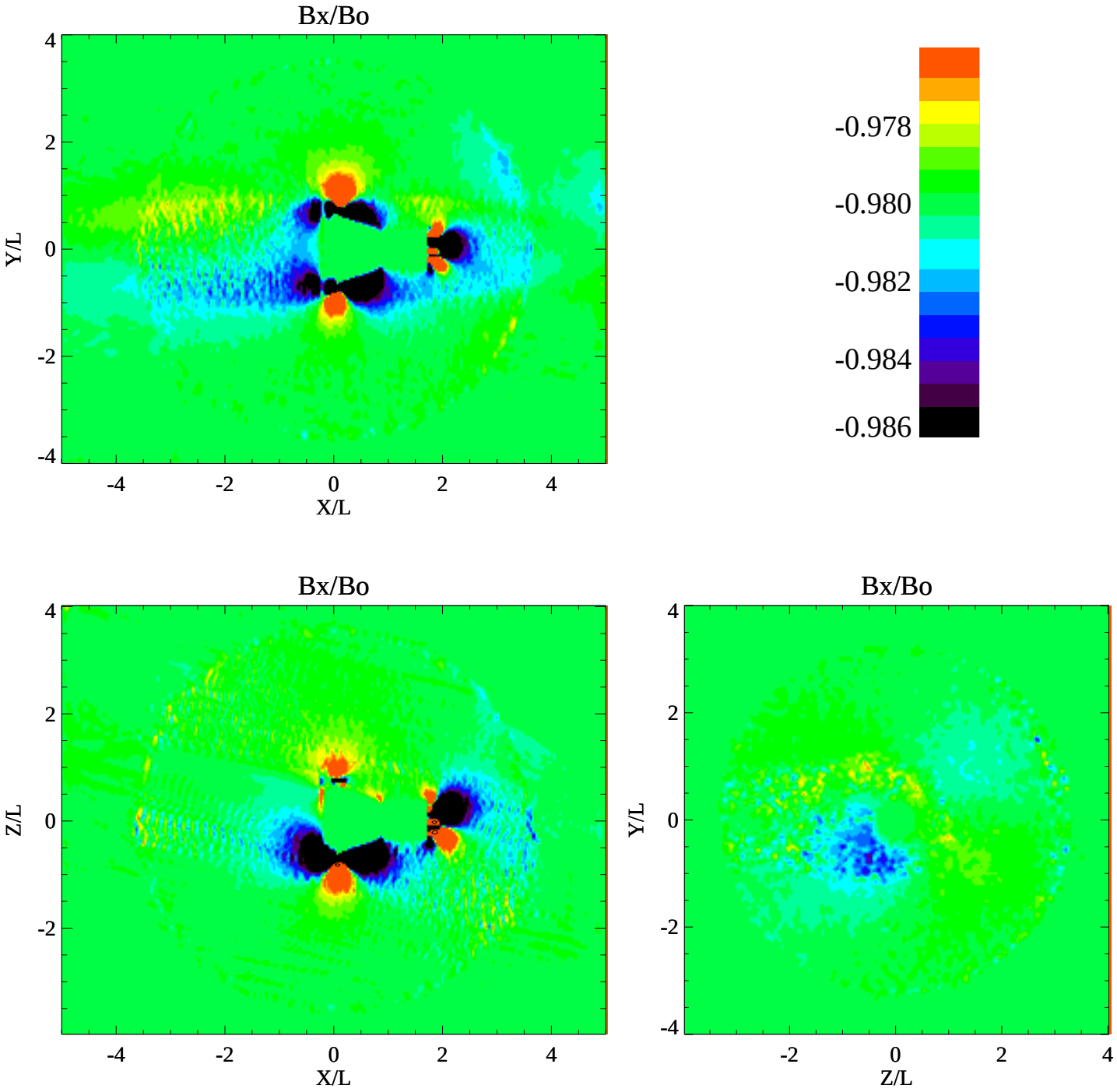

Figure 47. Magnetic field component $B_x(B_0)$ in the y-x ($z = 0$), z-x ($y = 0$) and y-z ($x = 0$) planes. $U_0 = 200\,\mathrm{km/s}$, $M_A = 1.5$, $n = 5 \times 10^3\,\mathrm{cm}^{-3}$, $\beta_\mathrm{p} = 0.1$, $\beta_\mathrm{e} = 0.1$, $\theta_{bu} = 11^o$. Nonlinear saturation of the perturbations at $t = 0.15\,T_{ce}(0.02\,T_{transit})$ (case b).

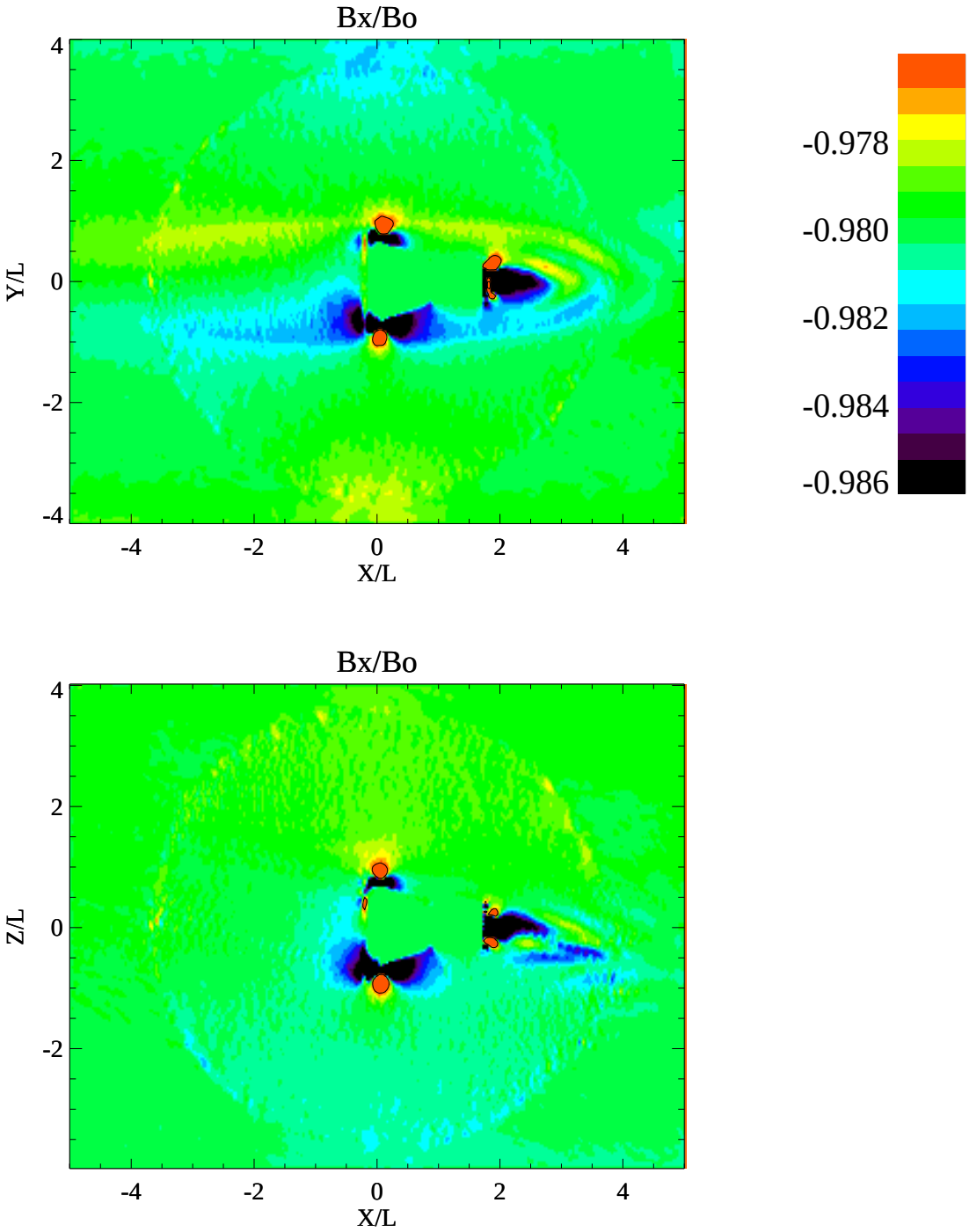

Figure 48. Magnetic field component $B_x(B_0)$ in the y-x ($z = 0$) and z-x ($y = 0$) planes. $U_0 = 200\,\mathrm{km/s}$, $M_A = 1.5$, $B_0 = 1500\,\mathrm{nT}$, $n = 5\times10^3\,\mathrm{cm}^{-3}$, $\beta_\mathrm{p} = 0.1$, $\beta_\mathrm{e} = 0.1$, $\theta_{bu} = 11^o$. Nonlinear saturation of the perturbations at $t = 0.29\,T_{ce}(0.04\,T_{transit})$ (case c).

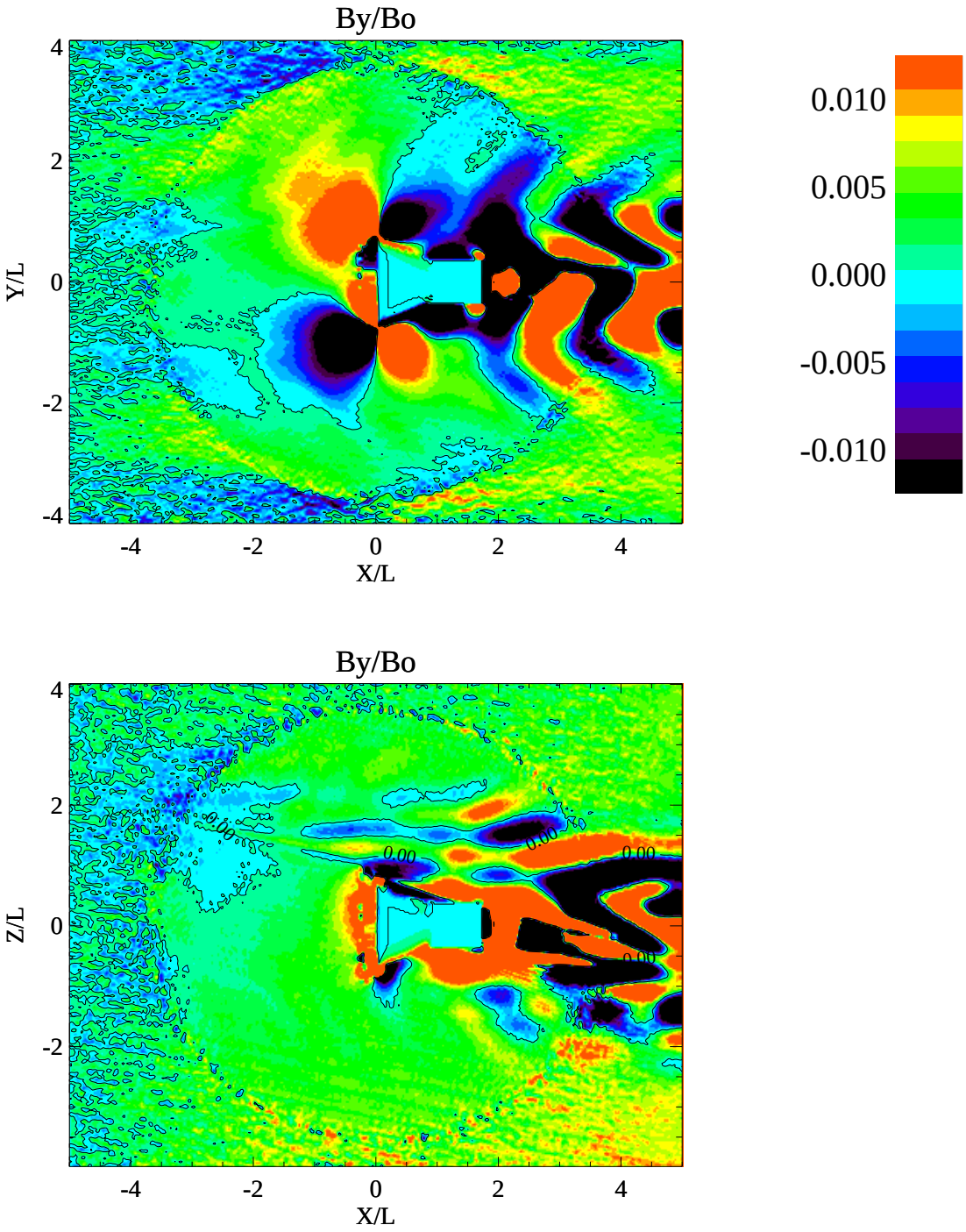

Figure 49. Magnetic field component $B_y(B_0)$ in the y-x ($z = 0$) and z-x ($y = 0$) planes. $U_0 = 200\,\mathrm{km/s}$, $M_A = 1.5$, $B_0 = 1500\,\mathrm{nT}$, $n = 5\times10^3\,\mathrm{cm}^{-3}$, $\beta_\mathrm{p} = 0.1$, $\beta_\mathrm{e} = 0.1$, $\theta_{bu} = 11^o$. Nonlinear saturation of the perturbations at $t = 0.104\,T_{ce}(0.013\,T_{transit})$ (case a).

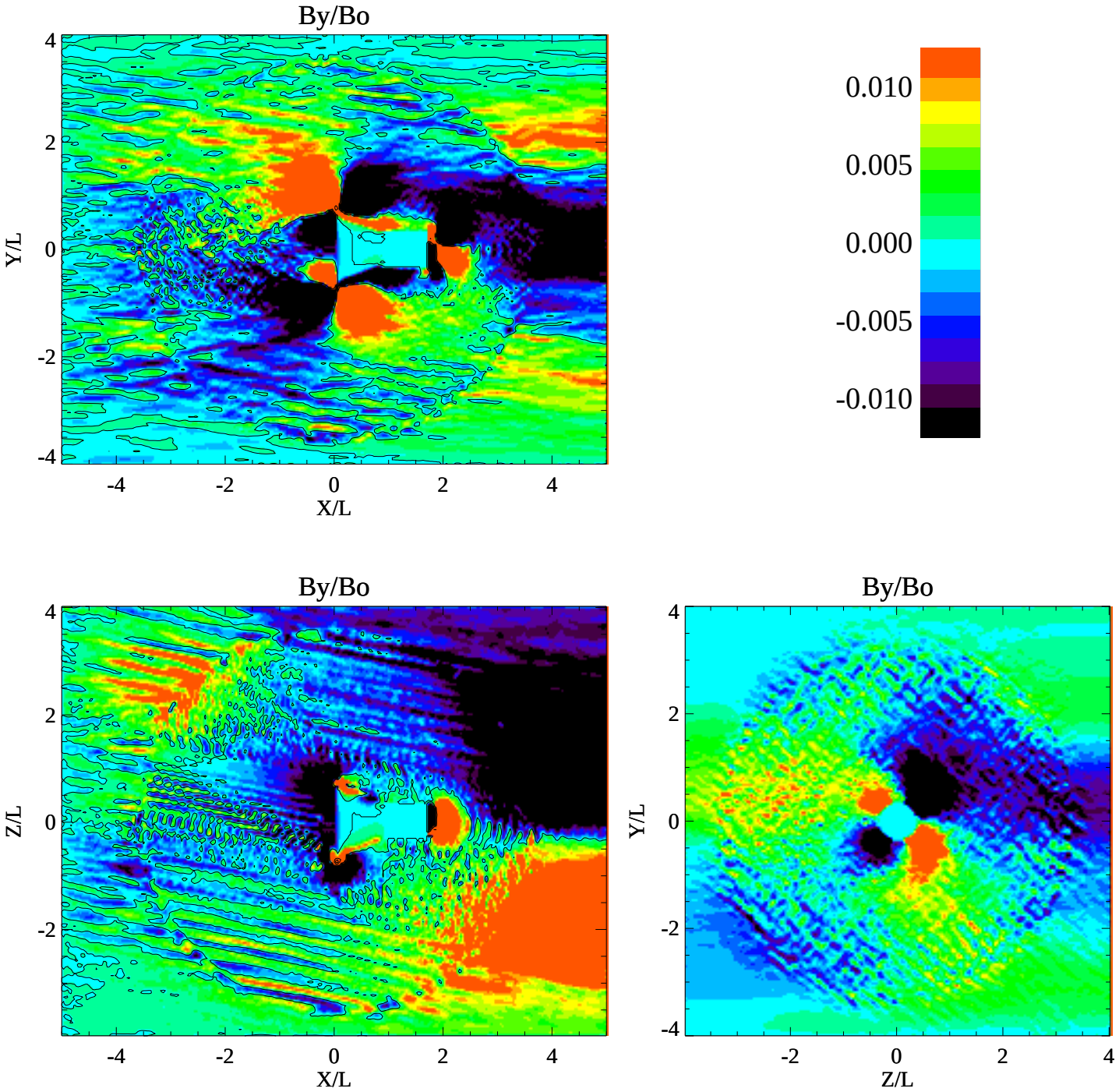

Figure 50. Magnetic field component $B_y(B_0)$ in the y-x ($z = 0$), z-x ($y = 0$) and y-z ($x = 0$) planes. $U_0 = 200\,\mathrm{km/s}$, $M_A = 1.5$, $n = 5 \times 10^3\,\mathrm{cm}^{-3}$, $\beta_\mathrm{p} = 0.1$, $\beta_\mathrm{e} = 0.1$, $\theta_{bu} = 11^o$. Nonlinear saturation of the perturbations at $t = 0.15\,T_{ce}(0.02\,T_{transit})$ (case b).

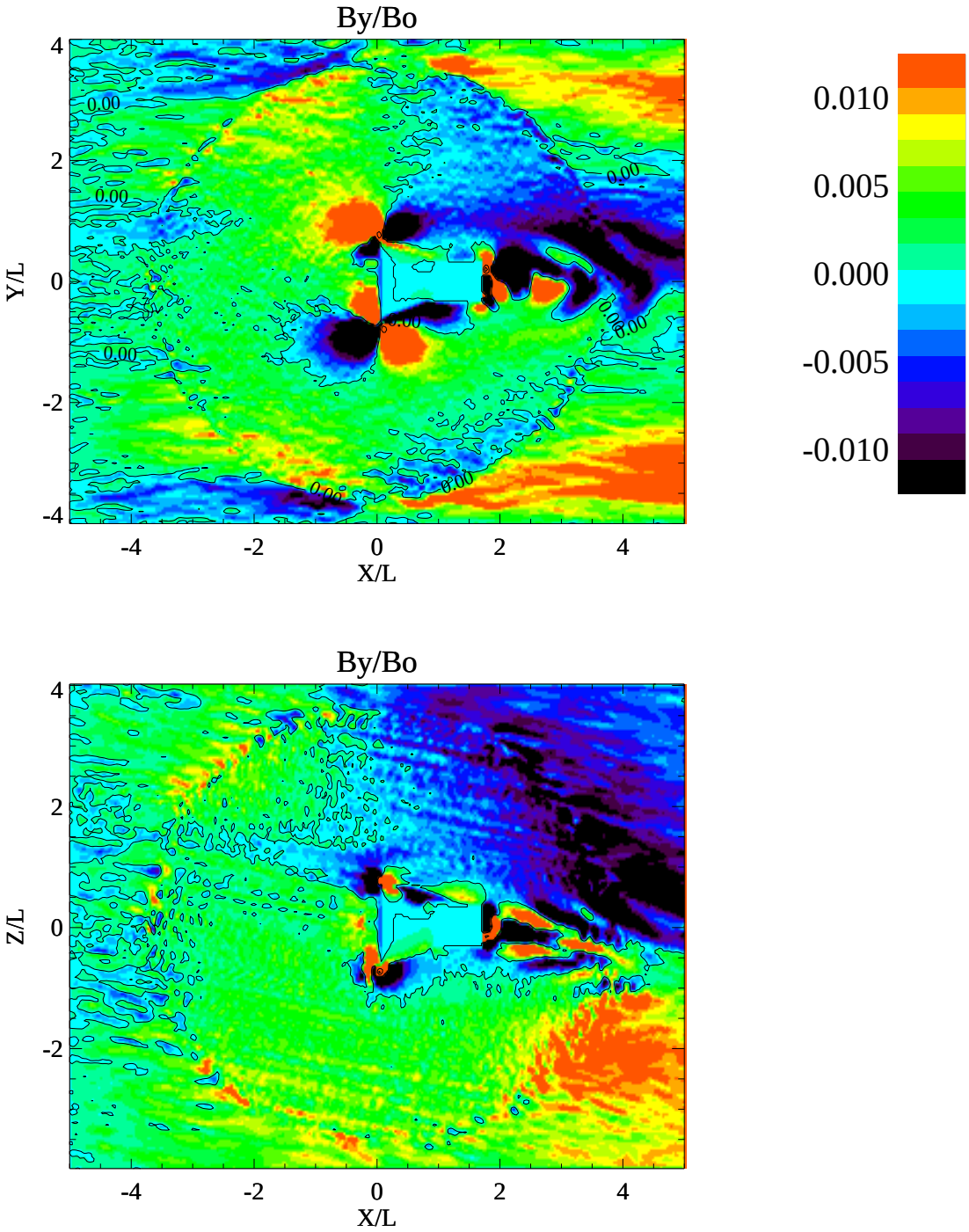

Figure 51. Magnetic field component $B_y(B_0)$ in the y-x ($z = 0$) and z-x ($y = 0$) planes. $U_0 = 200\,\mathrm{km/s}$, $M_A = 1.5$, $B_0 = 1500\,\mathrm{nT}$, $n = 5\times10^3\,\mathrm{cm}^{-3}$, $\beta_\mathrm{p} = 0.1$, $\beta_\mathrm{e} = 0.1$, $\theta_{bu} = 11^o$. Nonlinear saturation of the perturbations at $t = 0.29\,T_{ce}(0.04\,T_{transit})$ (case c).

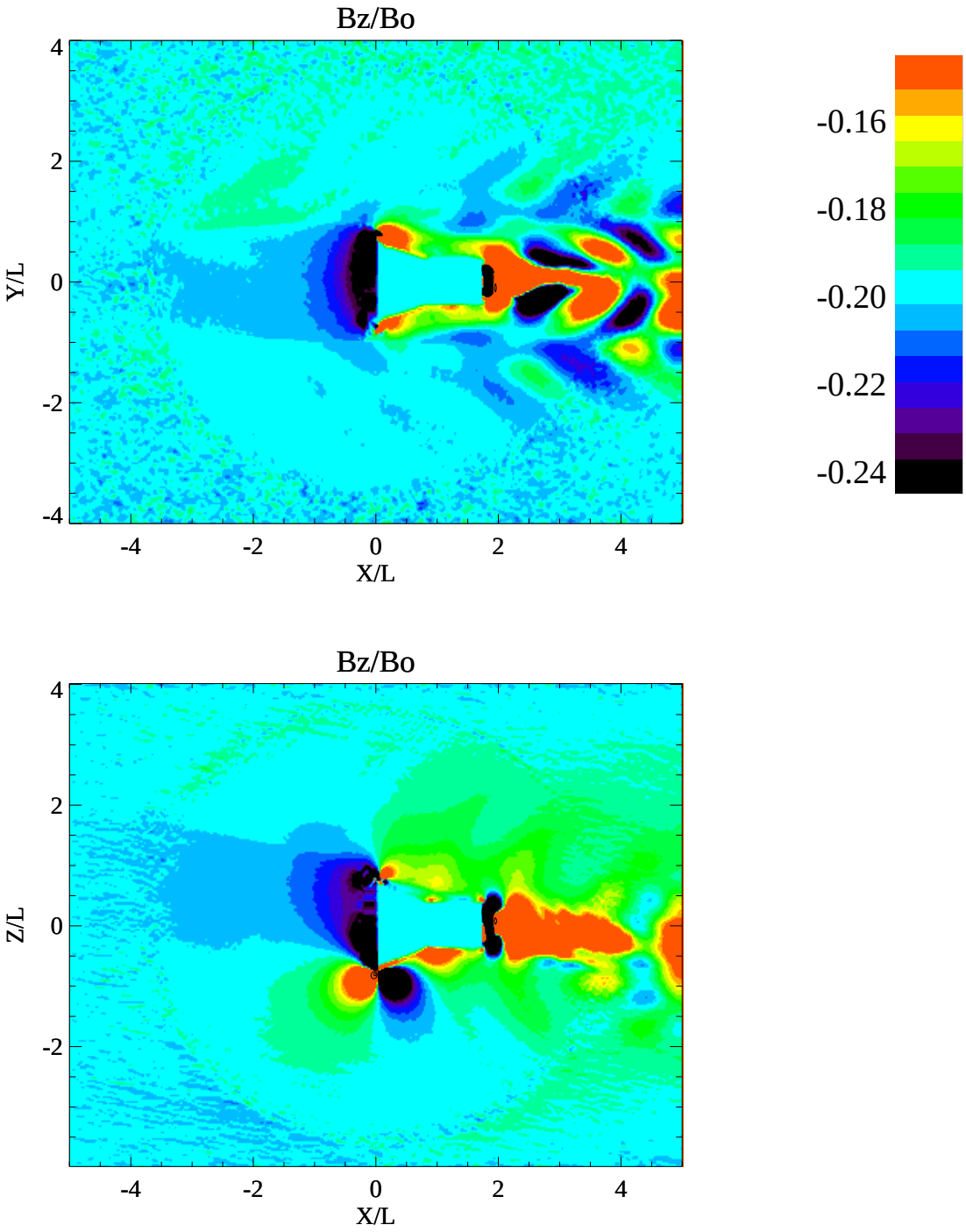

Figure 52. Magnetic field component $B_z(B_0)$ in the y-x ($z = 0$) and z-x ($y = 0$) planes. $U_0 = 200\,\mathrm{km/s}$, $M_A = 1.5$, $B_0 = 1500\,\mathrm{nT}$, $n = 5\times10^3\,\mathrm{cm}^{-3}$, $\beta_\mathrm{p} = 0.1$, $\beta_\mathrm{e} = 0.1$, $\theta_{bu} = 11^o$. Nonlinear saturation of the perturbations at $t = 0.104\,T_{ce}(0.013\,T_{transit})$ (case a).

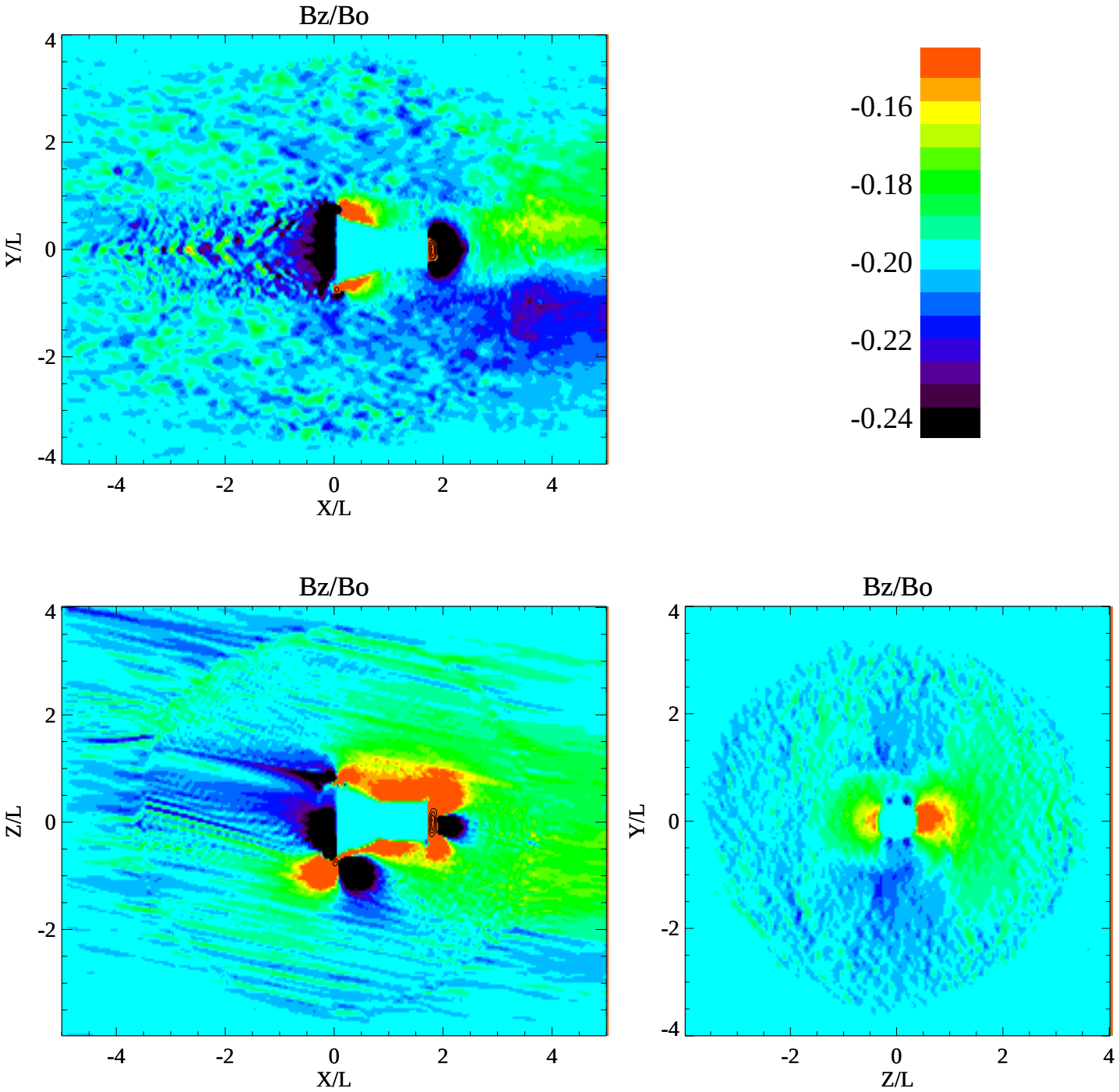

Figure 53. Magnetic field component $B_z(B_0)$ in the y-x ($z = 0$), z-x ($y = 0$) and y-z ($x = 0$) planes. $U_0 = 200\,\mathrm{km/s}$, $M_A = 1.5$, $n = 5 \times 10^3\,\mathrm{cm}^{-3}$, $\beta_\mathrm{p} = 0.1$, $\beta_\mathrm{e} = 0.1$, $\theta_{bu} = 11^o$. Nonlinear saturation of the perturbations at $t = 0.15\,T_{ce}(0.02\,T_{transit})$ (case b).

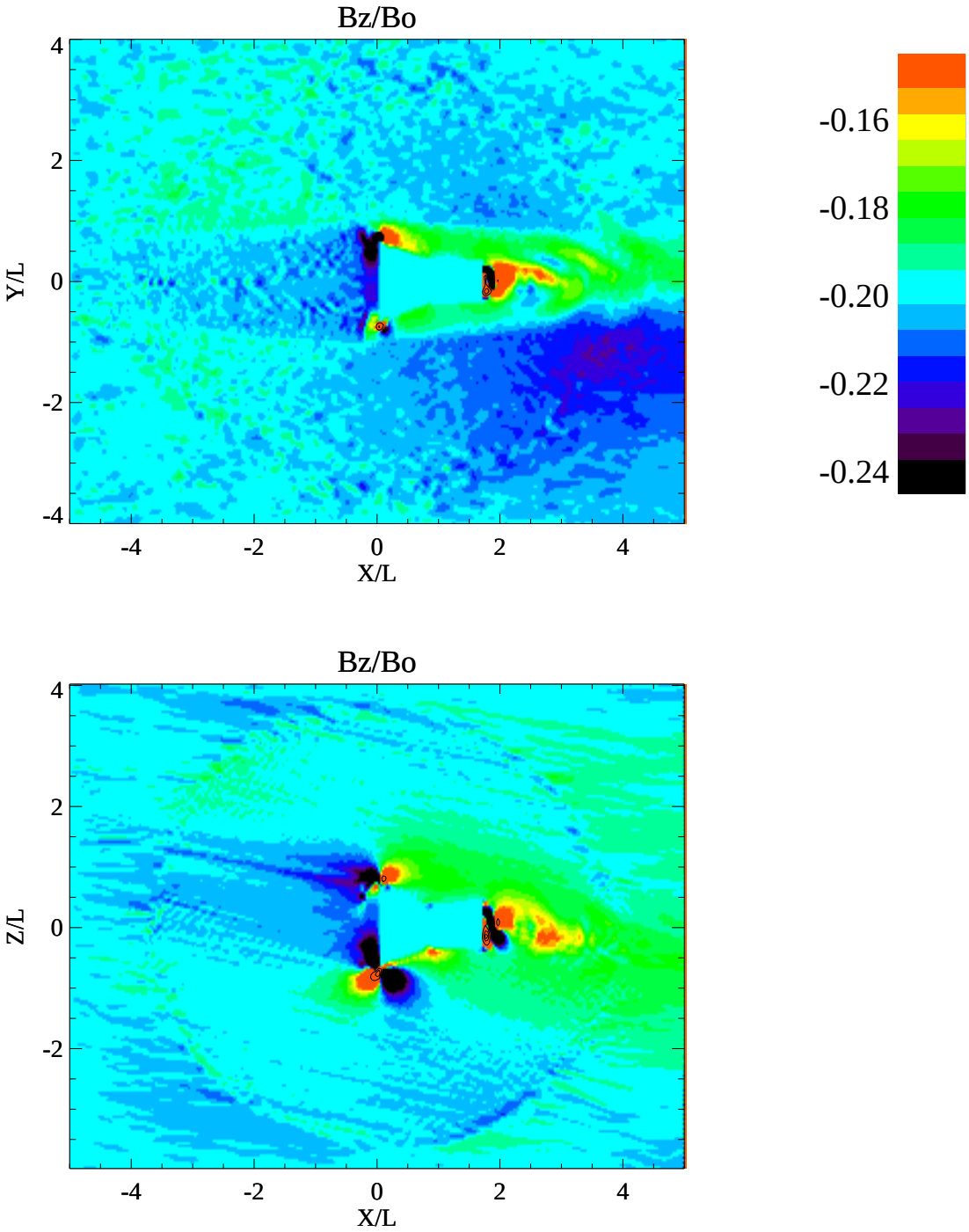

Figure 54. Magnetic field component $B_z(B_0)$ in the y-x ($z = 0$) and z-x ($y = 0$) planes. $U_0 = 200\,\mathrm{km/s}$, $M_A = 1.5$, $B_0 = 1500\,\mathrm{nT}$, $n = 5\times10^3\,\mathrm{cm}^{-3}$, $\beta_\mathrm{p} = 0.1$, $\beta_\mathrm{e} = 0.1$, $\theta_{bu} = 11^o$. Nonlinear saturation of the perturbations at $t = 0.29\,T_{ce}(0.04\,T_{transit})$ (case c).

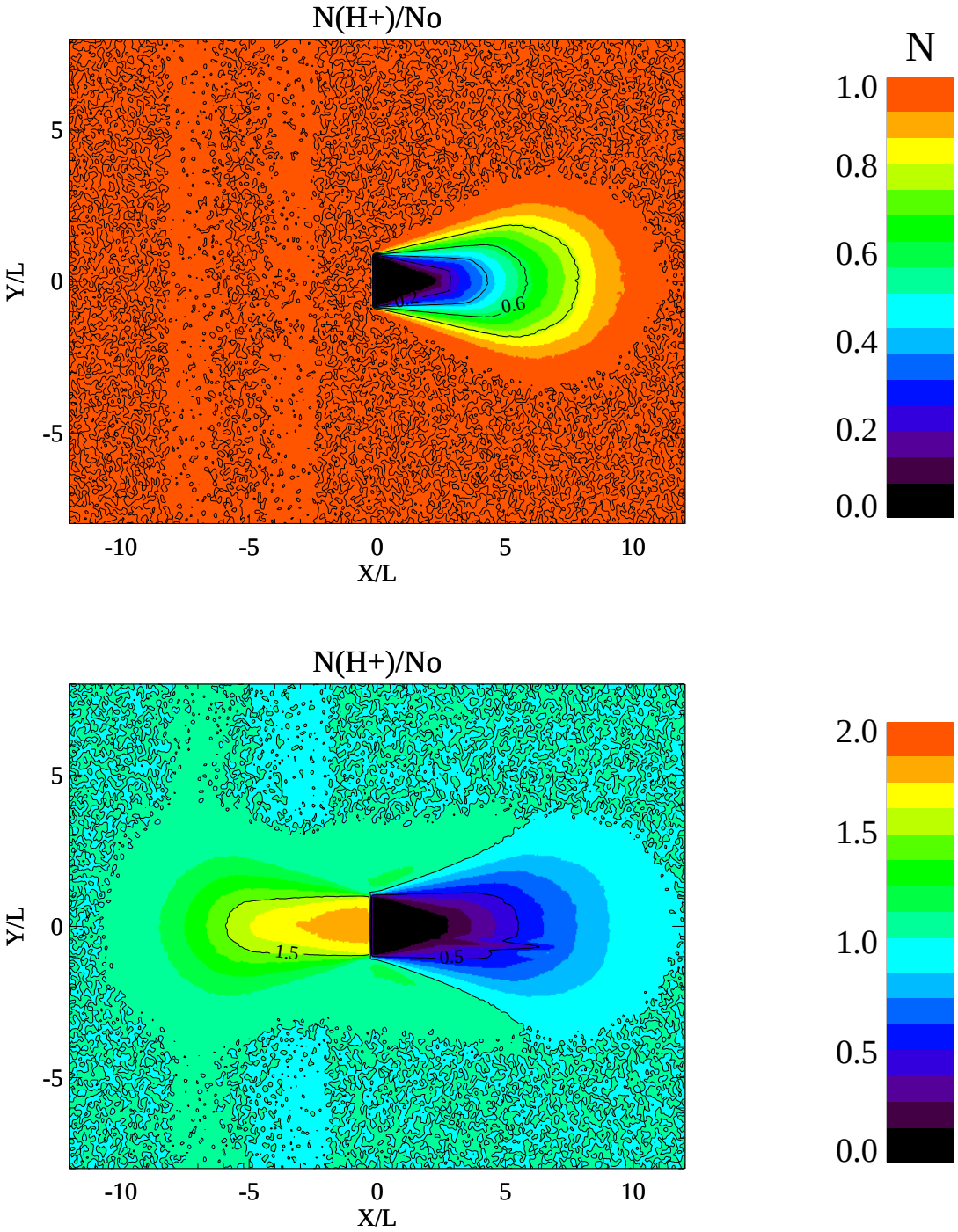

Figure 55. Solar wind ion density in the y-x plane. $U_0 = 200\,\mathrm{km/s}$, $M_A = 1.5$, $B_0 = 1500\,\mathrm{nT}$, $E_0 = U_0 B_0 = 0.3\,\mathrm{V/m}$, $n_{SW} = 5 \times 10^3\,\mathrm{cm}^{-3}$, $\beta_\mathrm{p} = 0.1$, $\beta_\mathrm{e} = 0.1$, $\theta_{bu} = 0^o$. Nonlinear saturation of the perturbations at $t = 2.2\,T_{ce}(0.26\,T_{transit})$ (case d, top; case e, bottom).

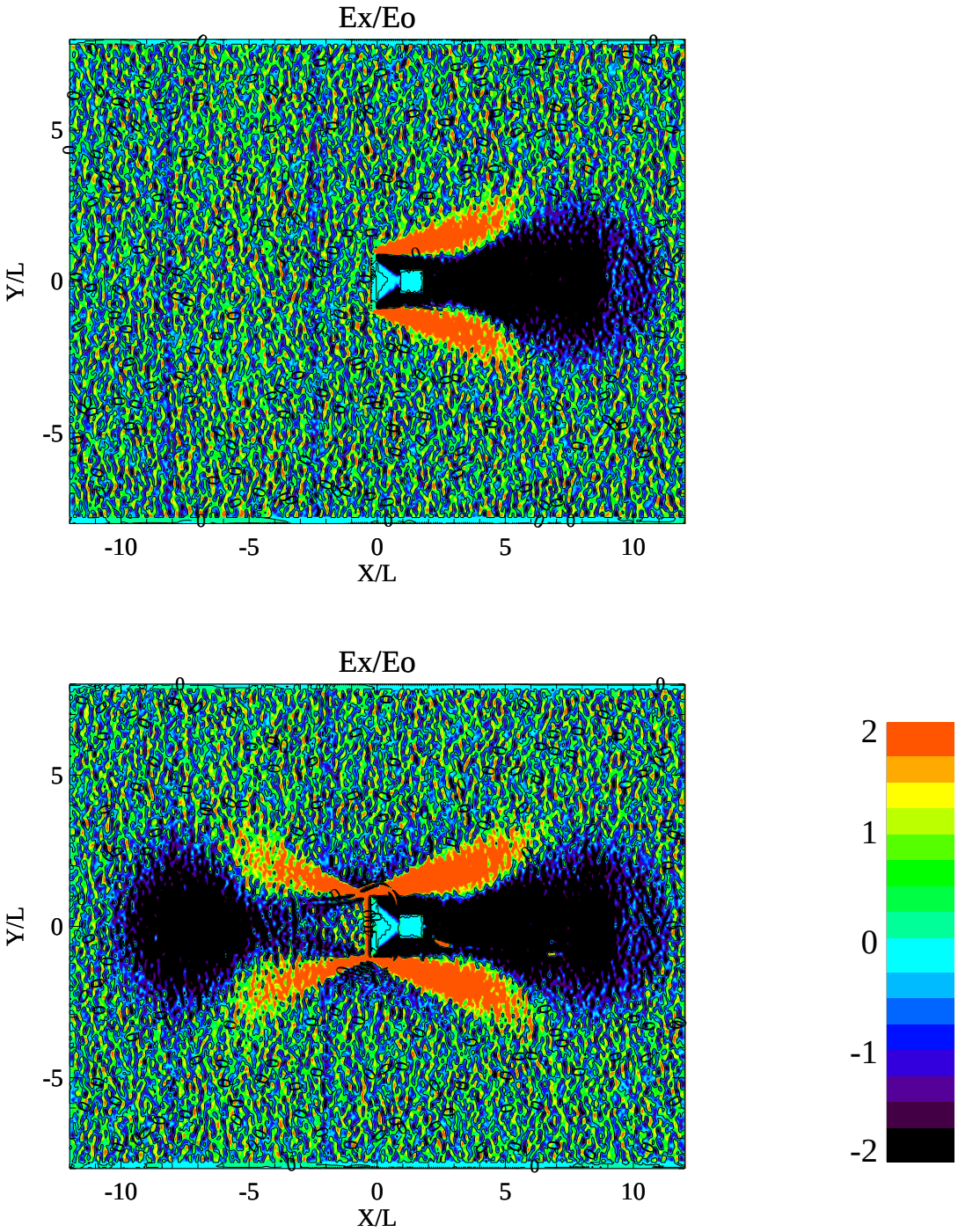

Figure 56. Electric field component $E_x(E_0)$ in the y-x plane. $U_0 = 200\,\mathrm{km/s}$, $M_A = 1.5$, $B_0 = 1500\,\mathrm{nT}$, $E_0 = U_0 B_0 = 0.3\,\mathrm{V/m}$, $n_{SW} = 5 \times 10^3\,\mathrm{cm}^{-3}$, $\beta_\mathrm{p} = 0.1$, $\beta_\mathrm{e} = 0.1$, $\theta_{bu} = 0^o$. Nonlinear saturation of the perturbations at $t = 2.2\,T_{ce}(0.26\,T_{transit})$ (case d, top; case e, bottom).

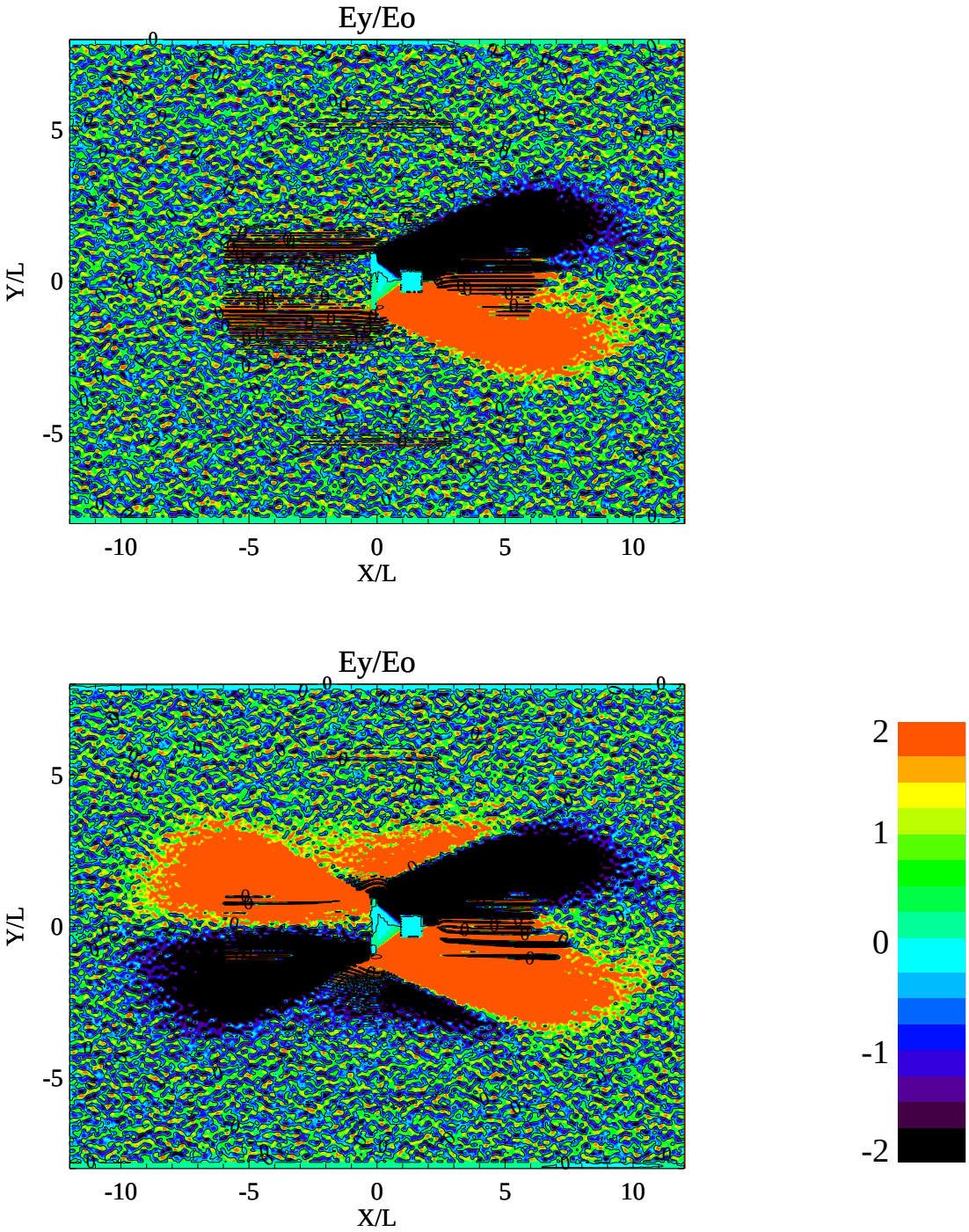

Figure 57. Electric field component $E_y(E_0)$ in the y-x plane. $U_0 = 200\,\mathrm{km/s}$, $M_A = 1.5$, $n_{SW} = 5 \times 10^3\,\mathrm{cm}^{-3}$, $\beta_\mathrm{p} = 0.1$, $\beta_\mathrm{e} = 0.1$, $\theta_{bu} = 0^o$. Nonlinear saturation of the perturbations at $t = 2.2\,T_{ce}(0.26\,T_{transit})$ (case d, top; case e, bottom).

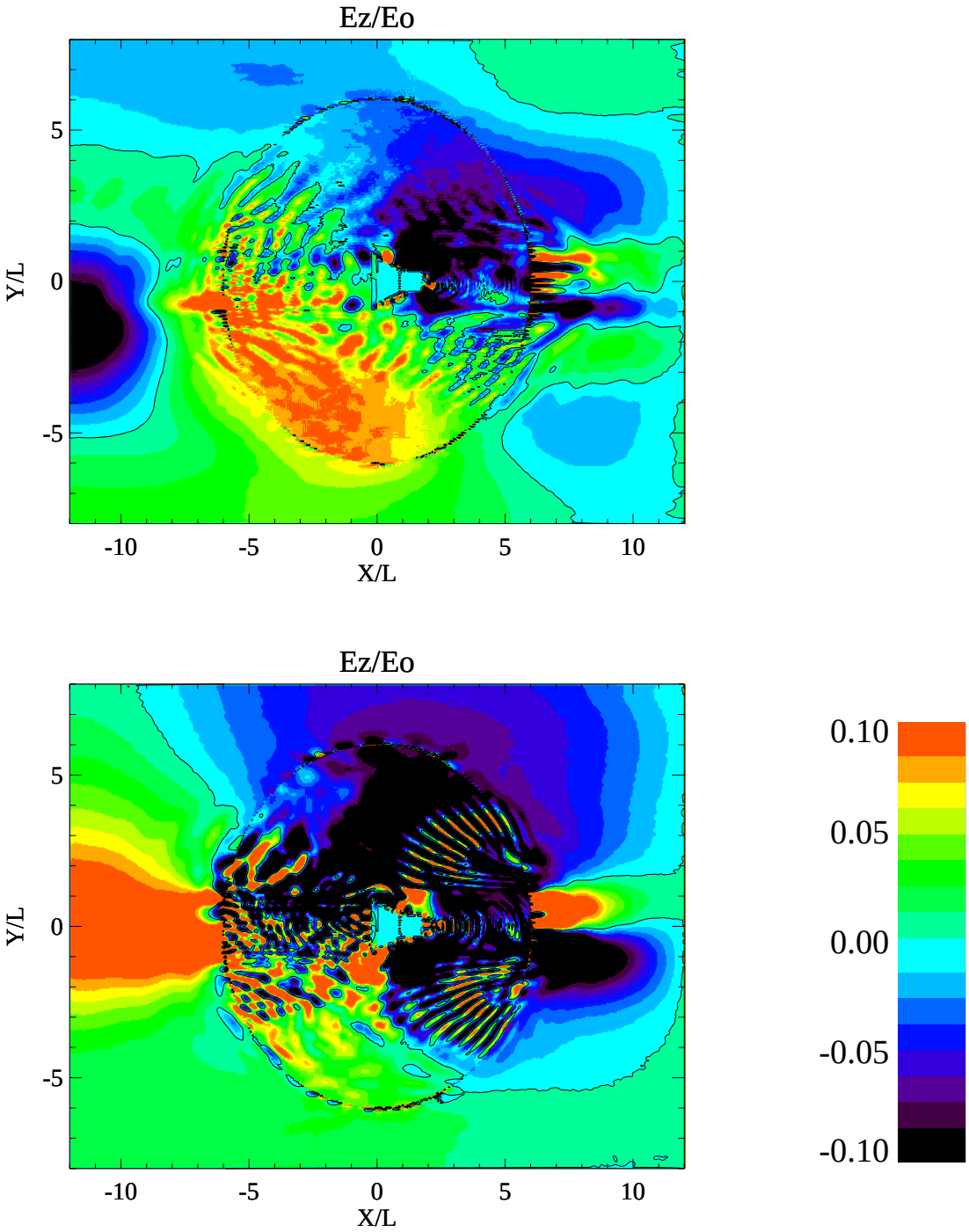

Figure 58. Electric field component $E_z(E_0)$ in the y-x plane. $U_0 = 200\,\mathrm{km/s}$, $M_A = 1.5$, $n_{SW} = 5 \times 10^3\,\mathrm{cm}^{-3}$, $\beta_\mathrm{p} = 0.1$, $\beta_\mathrm{e} = 0.1$, $\theta_{bu} = 0^o$. Nonlinear saturation of the perturbations at $t = 2.2\,T_{ce}(0.26\,T_{transit})$ (case d, top; case e, bottom).

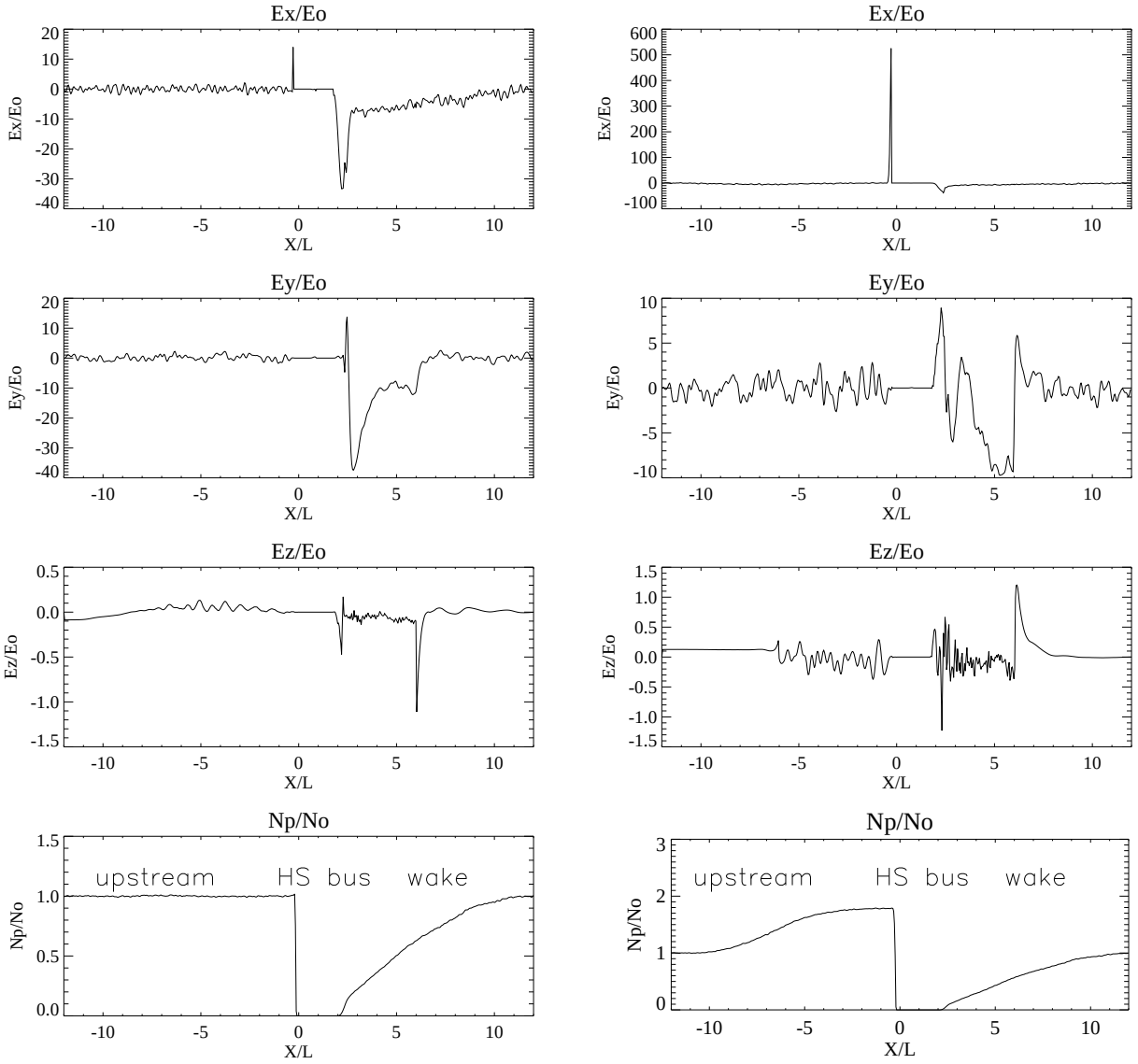

Figure 59. 1-D cuts for the electric field component $E_x(E_0)$, $E_y(E_0)$ and $E_z(E_0)$ $(y = 0)$. $U_0 = 200\,\mathrm{km/s}$, $M_A = 1.5$, $B_0 = 1500\,\mathrm{nT}$, $n = 5 \times 10^3\,\mathrm{cm}^{-3}$, $\beta_\mathrm{p} = 0.1$, $\beta_\mathrm{e} = 0.1$, $\theta_{bu} = 0^o$. Nonlinear saturation of the perturbations at $t = 2.2\,T_{ce}(0.26\,T_{transit})$ (case d, left; case e, right).

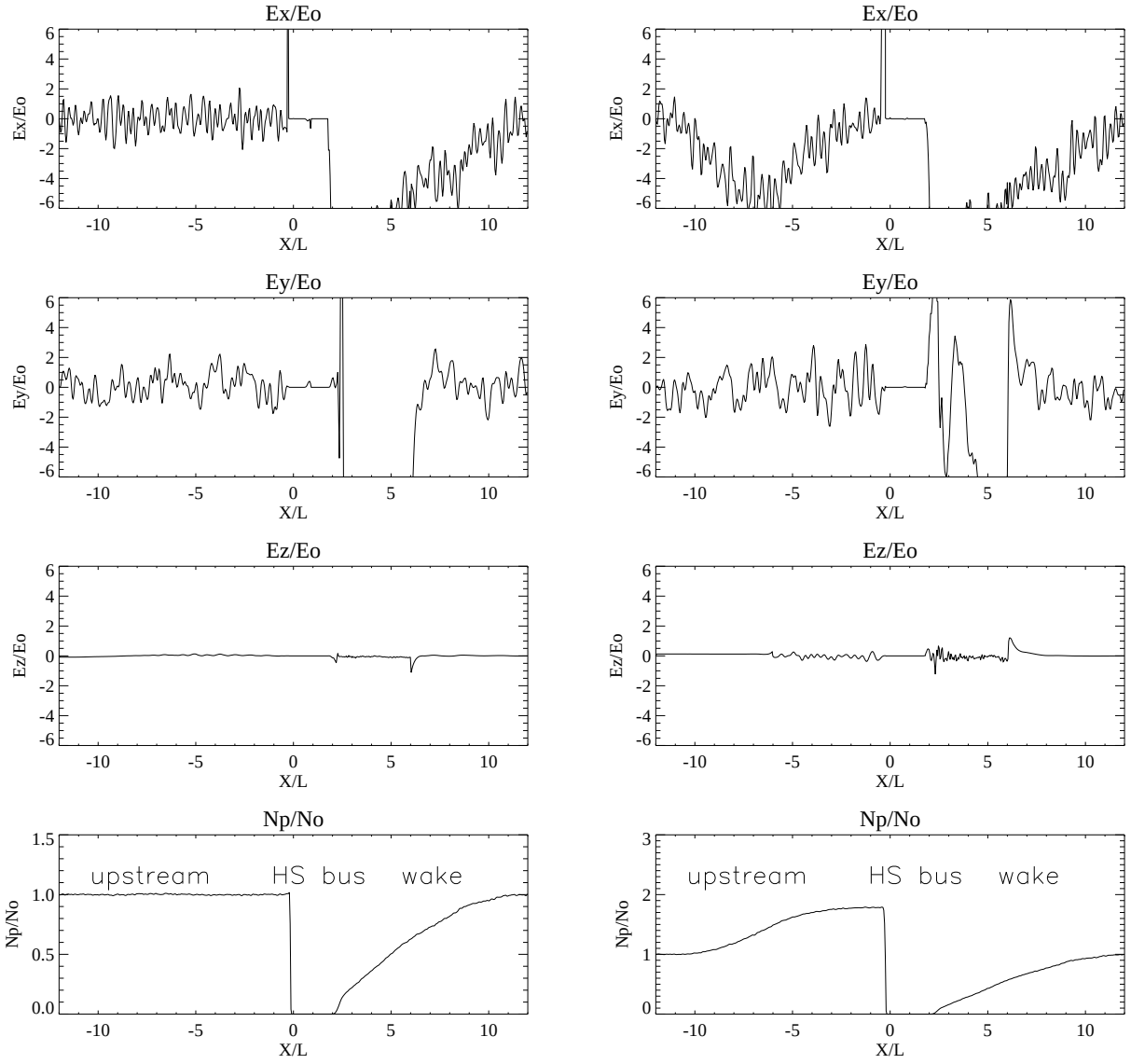

Figure 60. 1-D cuts for the electric field component $E_x(E_0)$, $E_y(E_0)$ and $E_z(E_0)$ $(y = 0)$. $U_0 = 200\,\mathrm{km/s}$, $M_A = 1.5$, $B_0 = 1500\,\mathrm{nT}$, $n = 5 \times 10^3\,\mathrm{cm}^{-3}$, $\beta_\mathrm{p} = 0.1$, $\beta_\mathrm{e} = 0.1$, $\theta_{bu} = 0^o$. Nonlinear saturation of the perturbations at $t = 2.2\,T_{ce}(0.26\,T_{transit})$ (case d, left; case e, right).

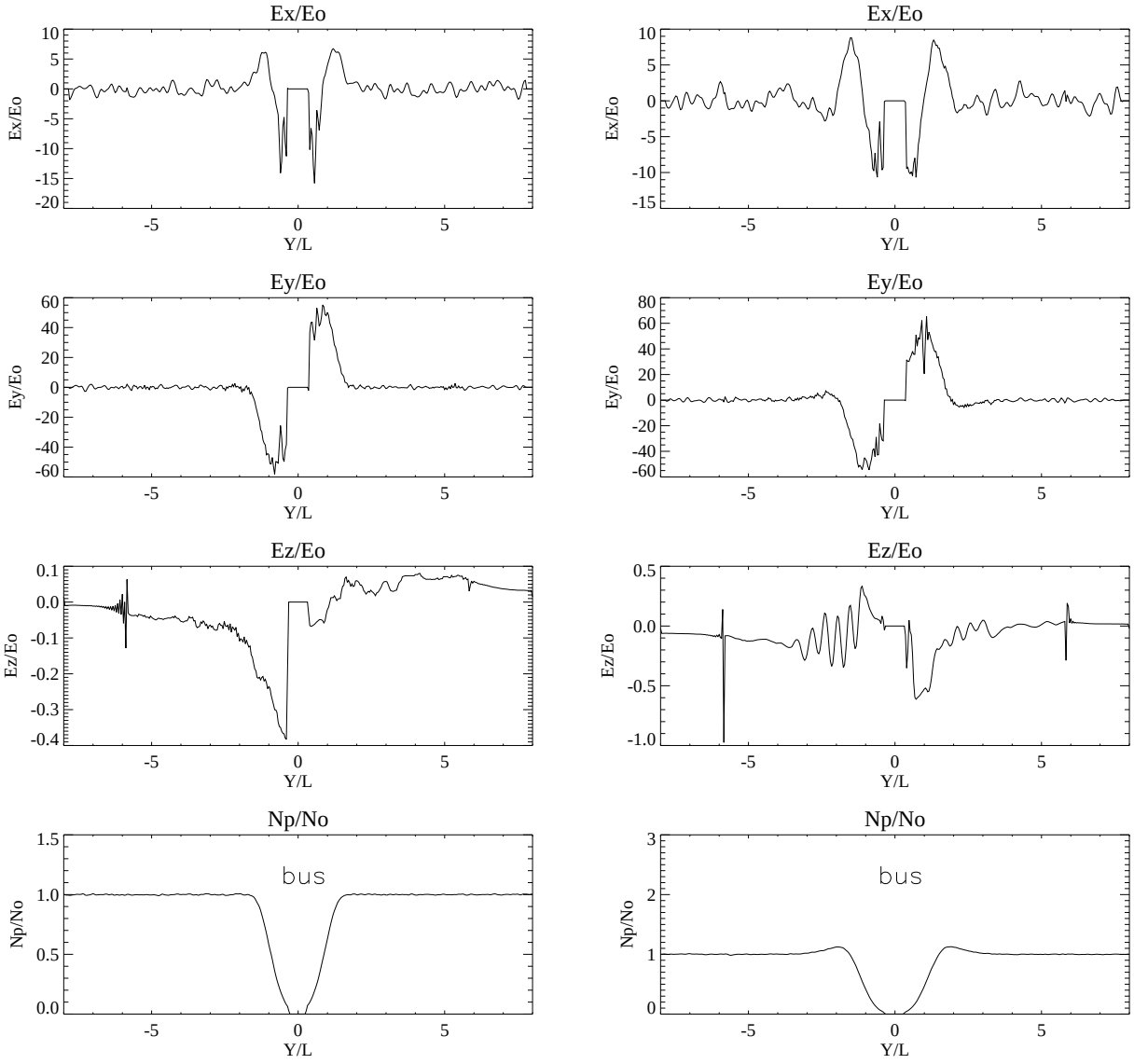

Figure 61. 1-D cuts for the electric field component $E_x(E_0)$, $E_y(E_0)$ and $E_z(E_0)$ ($x = 1.5$). $U_0 = 200\,\mathrm{km/s}$, $M_A = 1.5$, $B_0 = 1500\,\mathrm{nT}$, $n = 5 \times 10^3\,\mathrm{cm}^{-3}$, $\beta_\mathrm{p} = 0.1$, $\beta_\mathrm{e} = 0.1$, $\theta_{bu} = 0^o$. Nonlinear saturation of the perturbations at $t = 2.2\,T_{ce}(0.26\,T_{transit})$ (case d, left; case e, right).

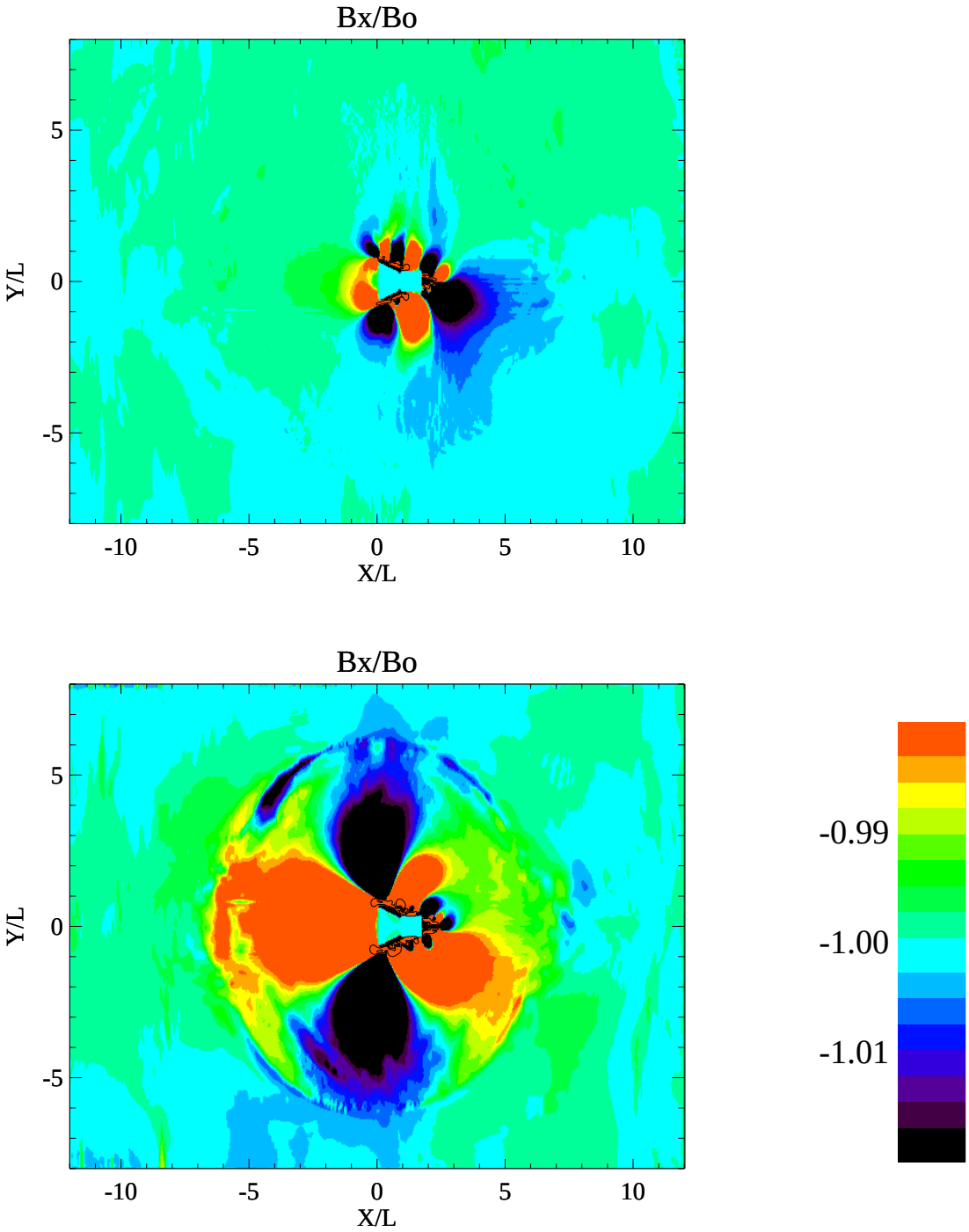

Figure 62. Magnetic field components $B_x(B_0)$ in the y-x plane. $U_0 = 200\,\mathrm{km/s}$, $M_A = 1.5$, $B_0 = 1500\,\mathrm{nT}$, $n = 5 \times 10^3\,\mathrm{cm}^{-3}$, $\beta_\mathrm{p} = 0.1$, $\beta_\mathrm{e} = 0.1$, $\theta_{bu} = 0^o$. Nonlinear saturation of the perturbations at $t = 2.2\,T_{ce}(0.26\,T_{transit})$ (case d, top; case e, bottom).

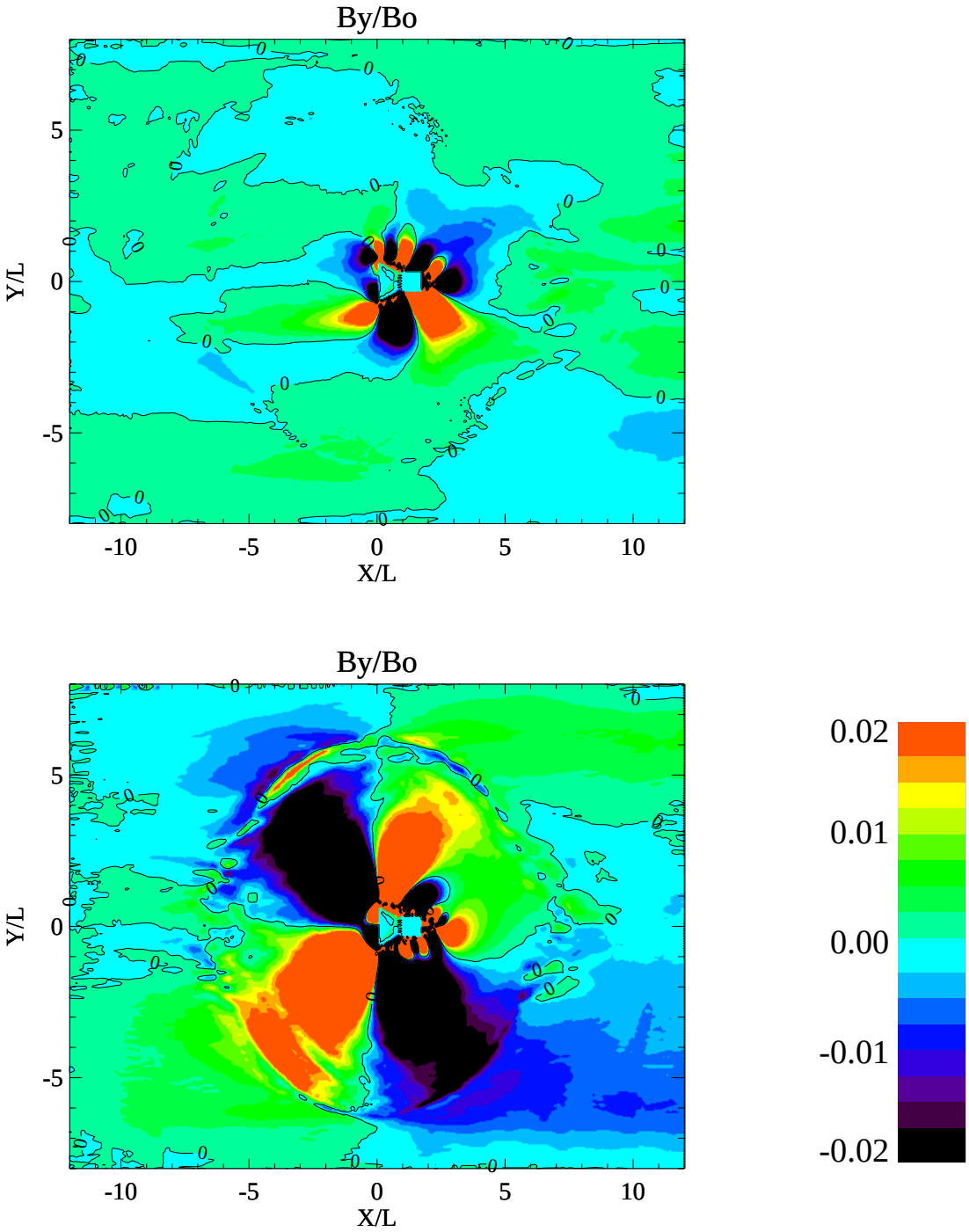

Figure 63. Magnetic field components $B_y(B_0)$ in the y-x plane. $U_0 = 200\,\mathrm{km/s}$, $M_A = 1.5$, $B_0 = 1500\,\mathrm{nT}$, $n = 5 \times 10^3\,\mathrm{cm}^{-3}$, $\beta_\mathrm{p} = 0.1$, $\beta_\mathrm{e} = 0.1$, $\theta_{bu} = 0^o$. Nonlinear saturation of the perturbations at $t = 2.2\,T_{ce}(0.26\,T_{transit})$ (case d, top; case e, bottom).

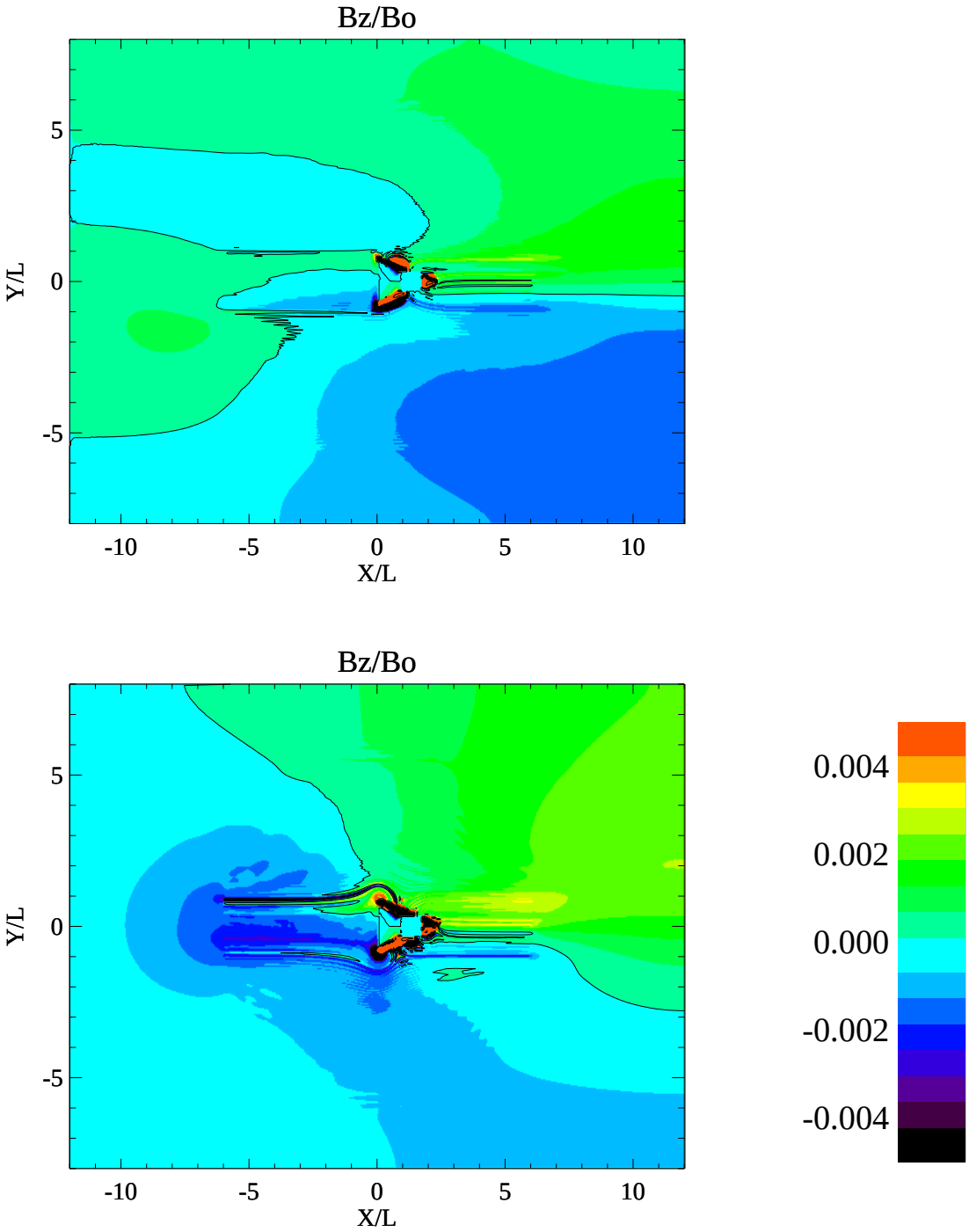

Figure 64. Magnetic field component $B_z(B_0)$ in the y-x plane. $U_0 = 200\,\mathrm{km/s}$, $M_A = 1.5$, $B_0 = 1500\,\mathrm{nT}$, $n = 5 \times 10^3\,\mathrm{cm}^{-3}$, $\beta_\mathrm{p} = 0.1$, $\beta_\mathrm{e} = 0.1$, $\theta_{bu} = 0^o$. Nonlinear saturation of the perturbations at $t = 2.2\,T_{ce}(0.26\,T_{transit})$ (case d, top; case e, bottom).

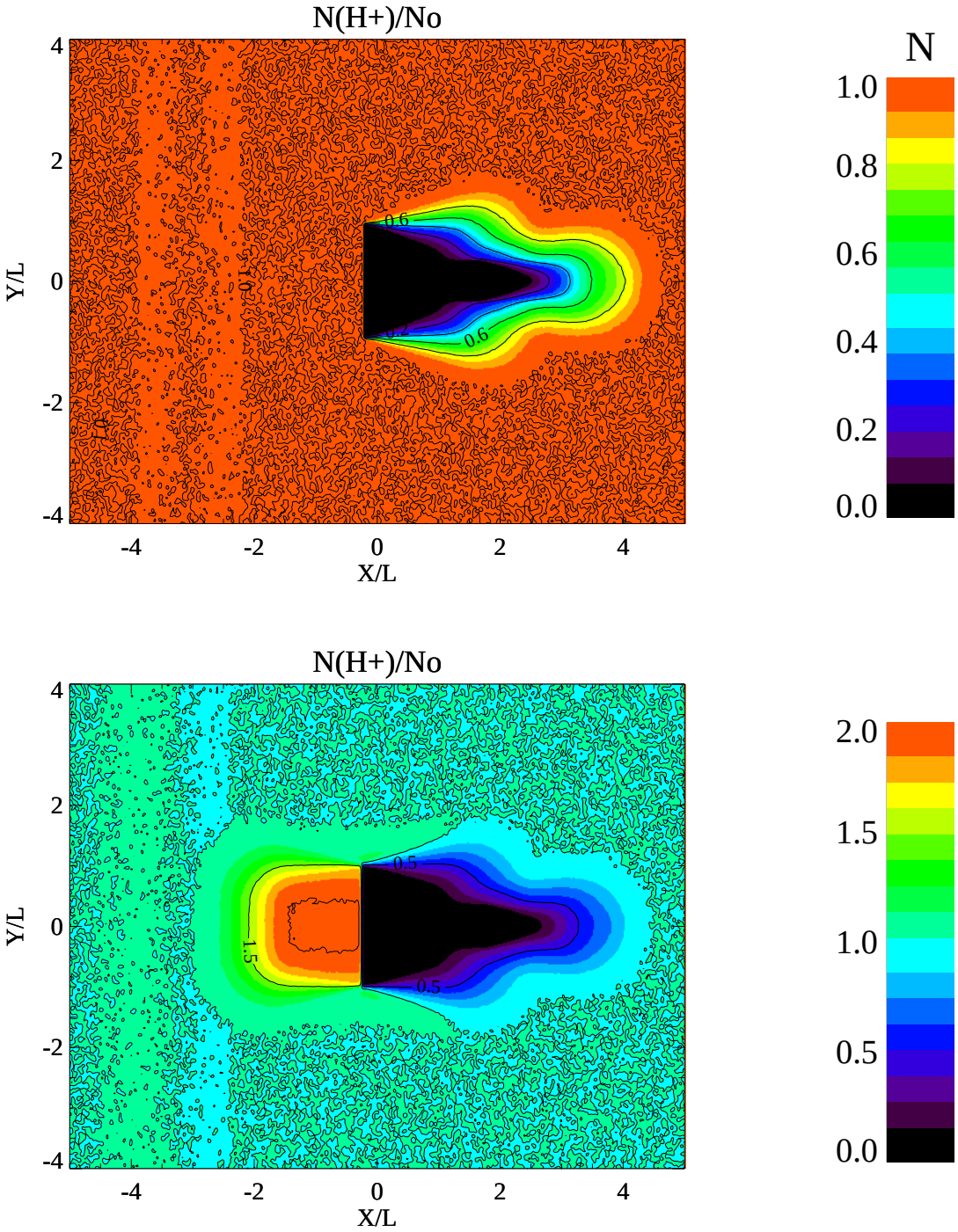

Figure 65. Solar wind ion density in the y-x plane. $U_0 = 200\,\mathrm{km/s}$, $M_A = 1.5$, $B_0 = 1500\,\mathrm{nT}$, $E_0 = U_0 B_0 = 0.3\,\mathrm{V/m}$, $n_{SW} = 5 \times 10^3\,\mathrm{cm}^{-3}$, $\beta_\mathrm{p} = 0.1$, $\beta_\mathrm{e} = 0.1$, $\theta_{bu} = 0^o$. Nonlinear saturation of the perturbations at $t = 1.0\,T_{ce}(0.12\,T_{transit})$ (case d', top; case e', bottom).

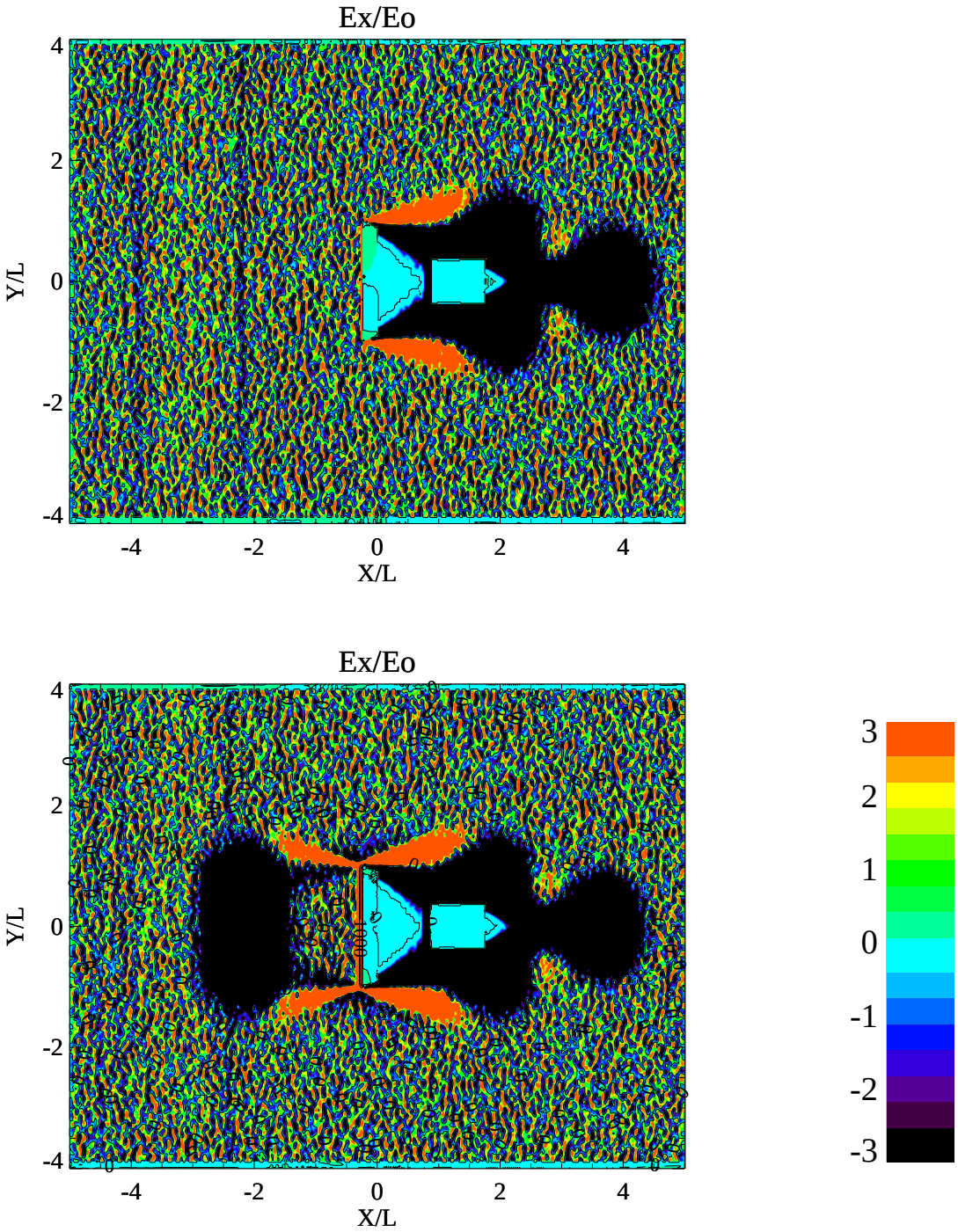

Figure 66. Electric field component $E_x(E_0)$ in the y-x plane. $U_0 = 200\,\mathrm{km/s}$, $M_A = 1.5$, $B_0 = 1500\,\mathrm{nT}$, $E_0 = U_0 B_0 = 0.3\,\mathrm{V/m}$, $n_{SW} = 5 \times 10^3\,\mathrm{cm}^{-3}$, $\beta_\mathrm{p} = 0.1$, $\beta_\mathrm{e} = 0.1$, $\theta_{bu} = 0^o$. Nonlinear saturation of the perturbations at $t = 1.0\,T_{ce}(0.12\,T_{transit})$ (case d', top; case e', bottom).

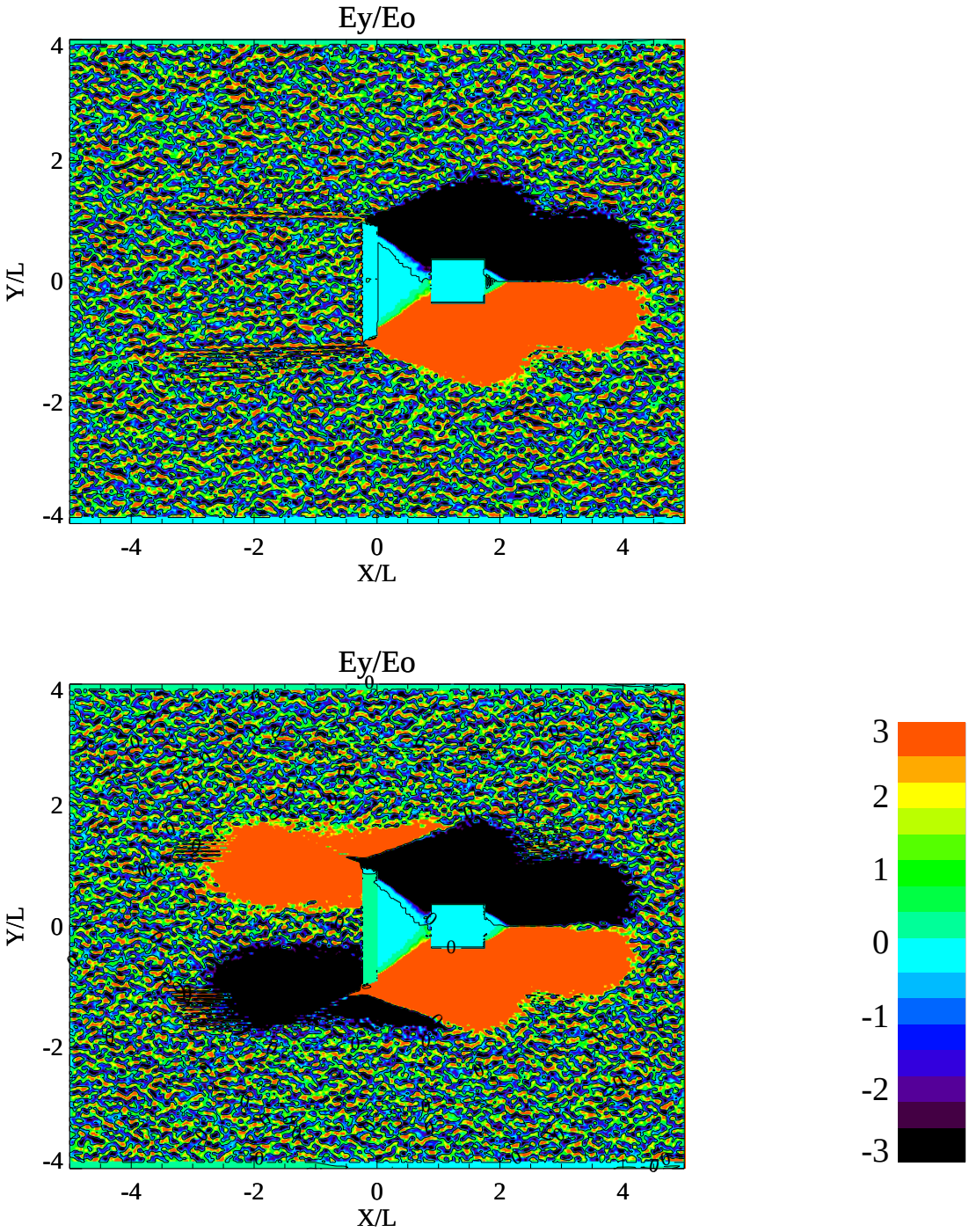

Figure 67. Electric field components $E_y(E_0)$ in the y-x plane. $U_0 = 200\,\mathrm{km/s}$, $M_A = 1.5$, $n_{SW} = 5 \times 10^3\,\mathrm{cm}^{-3}$, $\beta_\mathrm{p} = 0.1$, $\beta_\mathrm{e} = 0.1$, $\theta_{bu} = 0^o$. Nonlinear saturation of the perturbations at $t = 1.0\,T_{ce}(0.12\,T_{transit})$ (case d', top; case e', bottom).

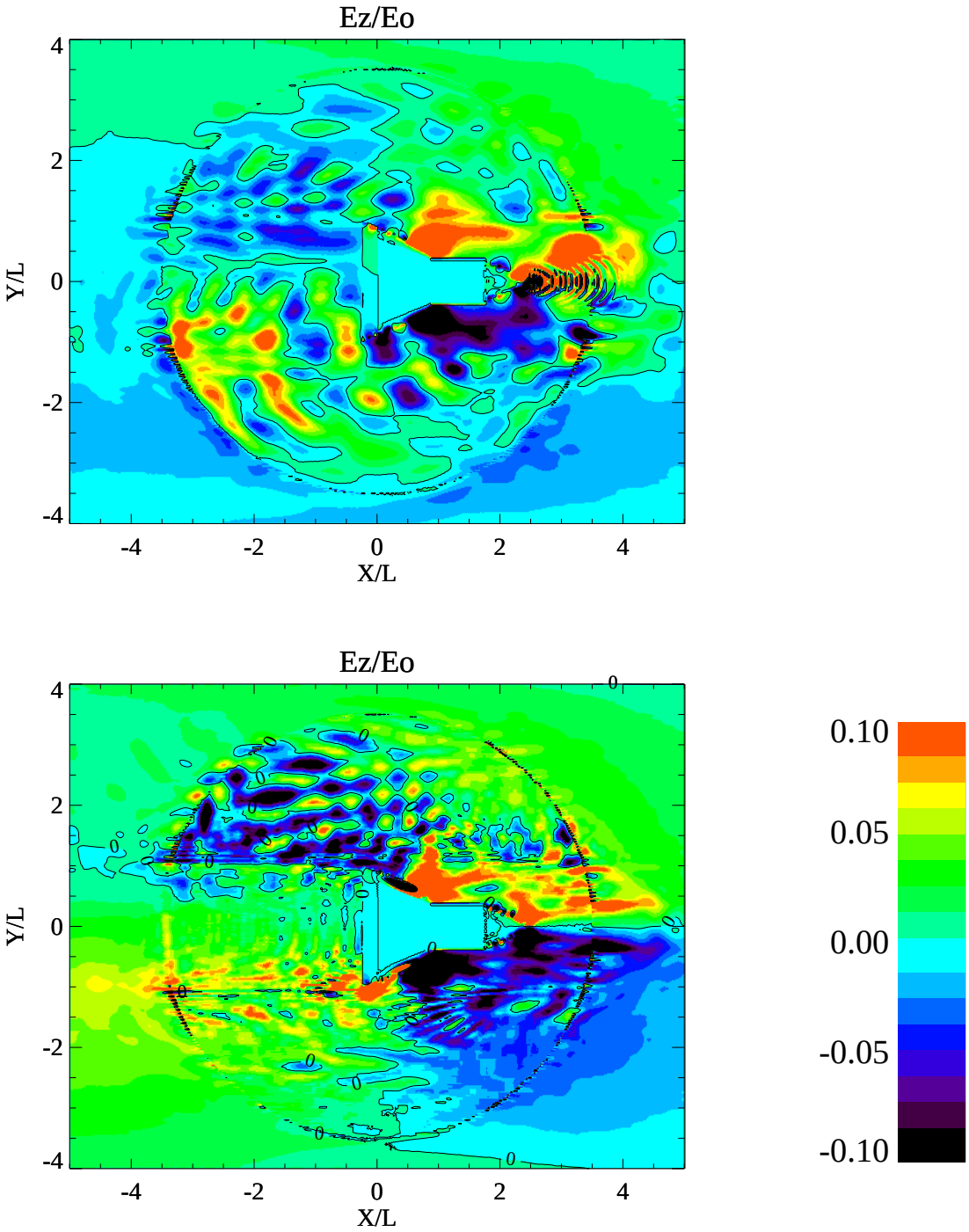

Figure 68. Electric field components $E_z(E_0)$ in the y-x plane. $U_0 = 200\,\mathrm{km/s}$, $M_A = 1.5$, $n_{SW} = 5 \times 10^3\,\mathrm{cm}^{-3}$, $\beta_\mathrm{p} = 0.1$, $\beta_\mathrm{e} = 0.1$, $\theta_{bu} = 0^o$. Nonlinear saturation of the perturbations at $t = 1.0\,T_{ce}(0.12\,T_{transit})$ (case d', top; case e', bottom).

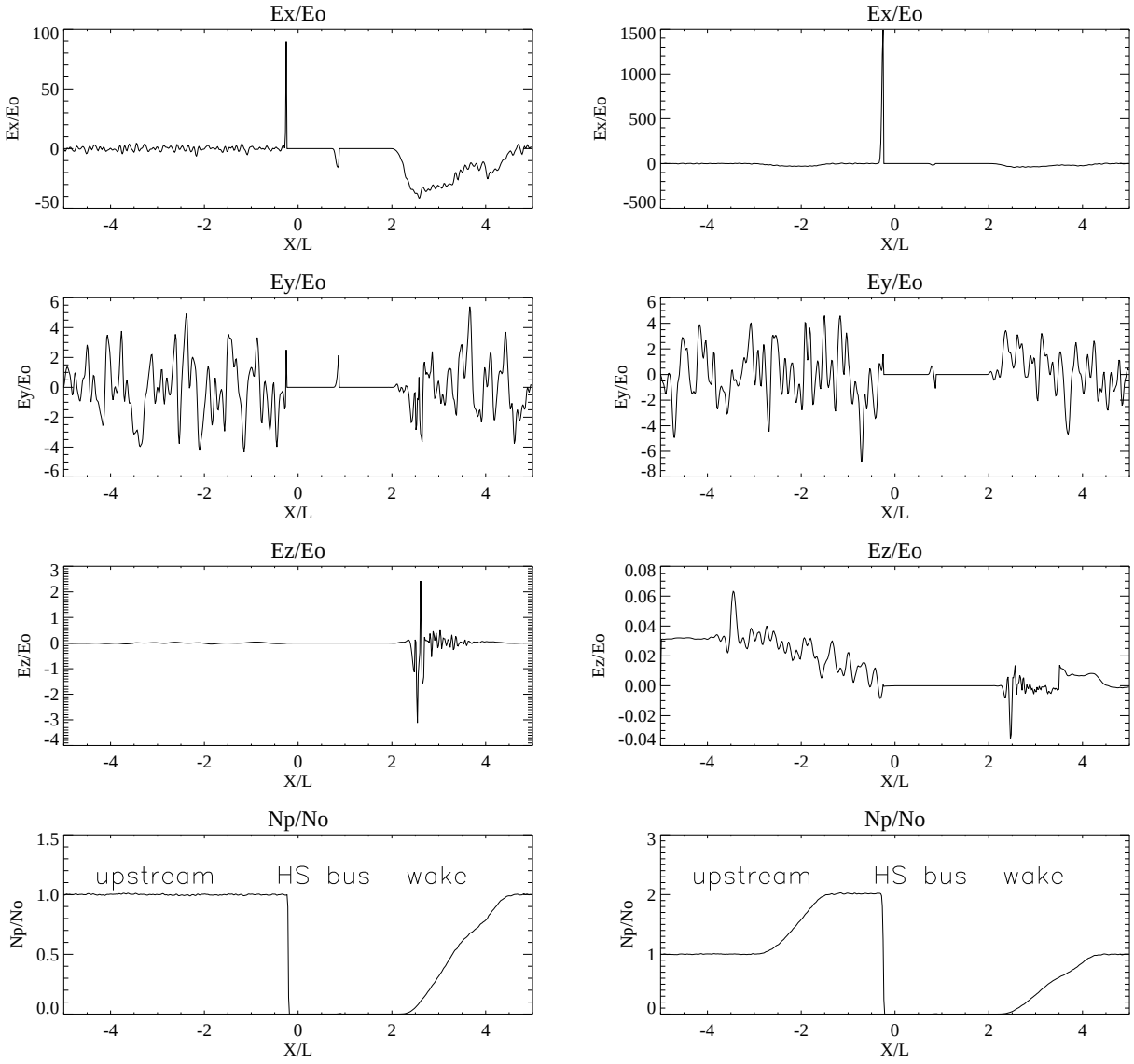

Figure 69. 1-D cuts for the electric field component $E_x(E_0)$, $E_y(E_0)$ and $E_z(E_0)$ $(y = 0)$. $U_0 = 200\,\mathrm{km/s}$, $M_A = 1.5$, $B_0 = 1500\,\mathrm{nT}$, $n = 5 \times 10^3\,\mathrm{cm}^{-3}$, $\beta_\mathrm{p} = 0.1$, $\beta_\mathrm{e} = 0.1$, $\theta_{bu} = 0^o$. Nonlinear saturation of the perturbations at $t = 1.0\,T_{ce}(0.12\,T_{transit})$ (case d', left; case e', right).

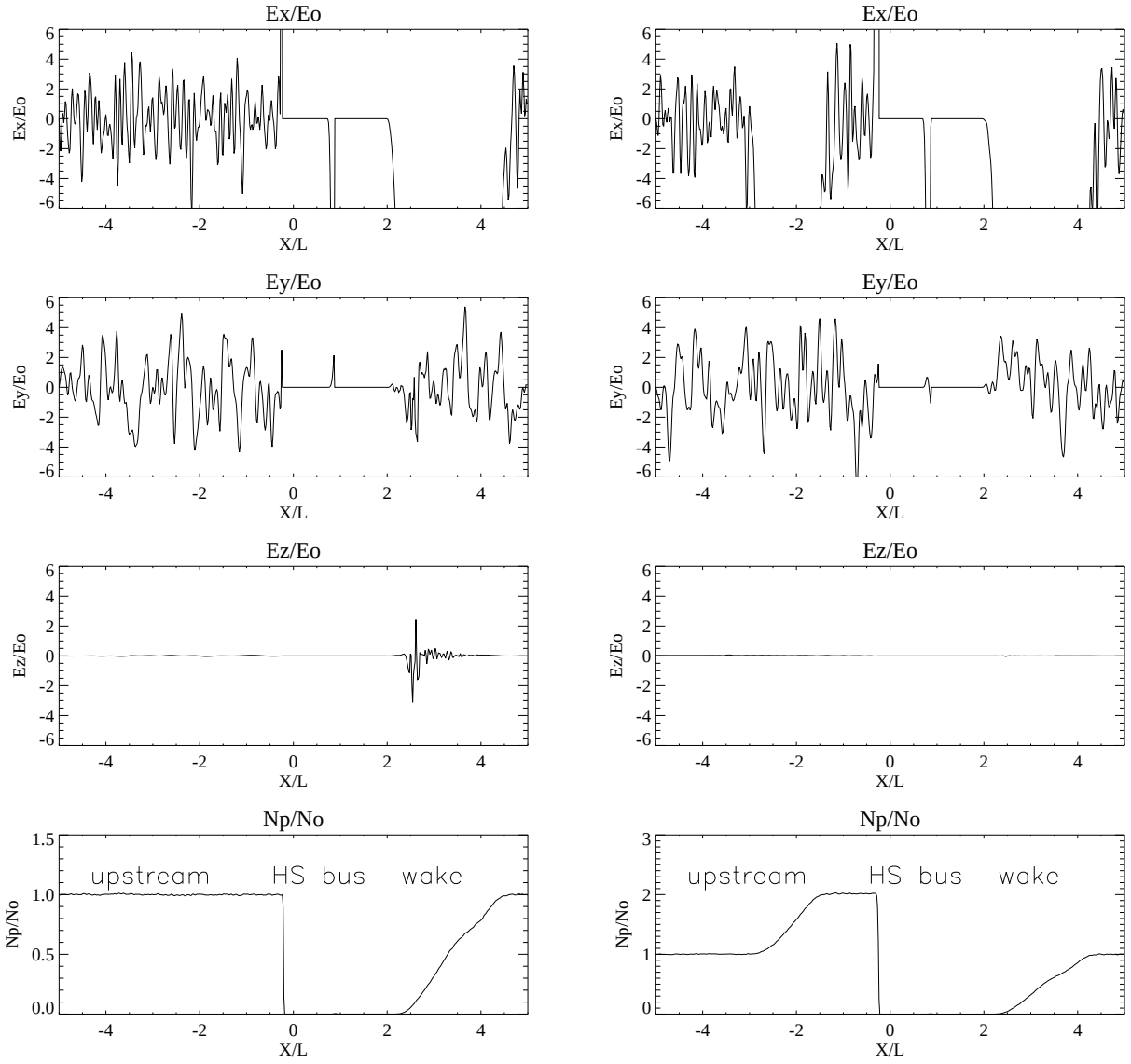

Figure 70. 1-D cuts for the electric field component $E_x(E_0)$, $E_y(E_0)$ and $E_z(E_0)$ $(y = 0)$. $U_0 = 200\,\mathrm{km/s}$, $M_A = 1.5$, $B_0 = 1500\,\mathrm{nT}$, $n = 5 \times 10^3\,\mathrm{cm}^{-3}$, $\beta_\mathrm{p} = 0.1$, $\beta_\mathrm{e} = 0.1$, $\theta_{bu} = 0^o$. Nonlinear saturation of the perturbations at $t = 1.0\,T_{ce}(0.12\,T_{transit})$ (case d', left; case e', right).

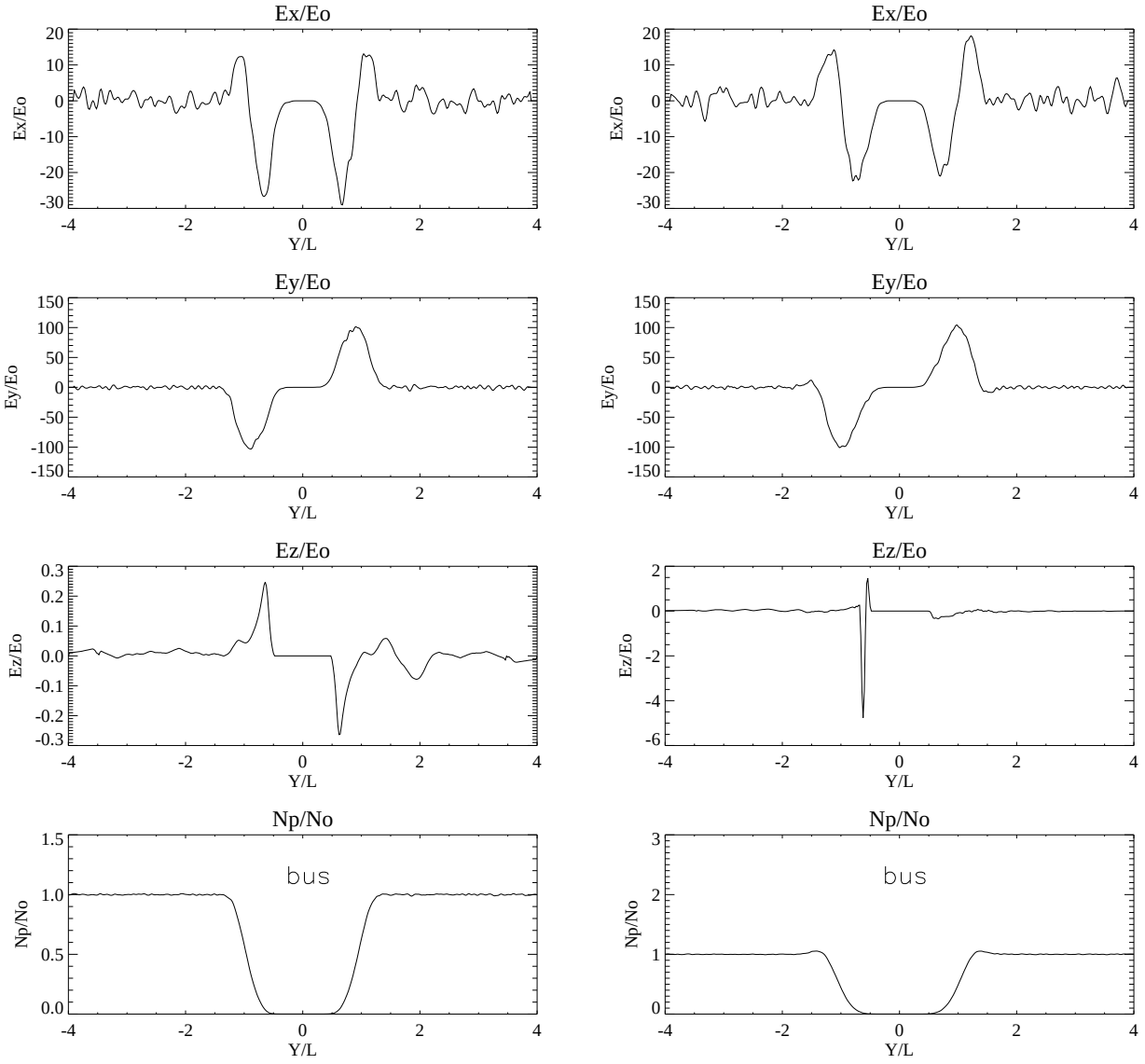

Figure 71. 1-D cuts for the electric field component $E_x(E_0)$, $E_y(E_0)$ and $E_z(E_0)$ ($x = 1.5$). $U_0 = 200\,\mathrm{km/s}$, $M_A = 1.5$, $B_0 = 1500\,\mathrm{nT}$, $n = 5 \times 10^3\,\mathrm{cm}^{-3}$, $\beta_\mathrm{p} = 0.1$, $\beta_\mathrm{e} = 0.1$, $\theta_{bu} = 0^o$. Nonlinear saturation of the perturbations at $t = 1.0\,T_{ce}(0.12\,T_{transit})$ (case d', left; case e', right).

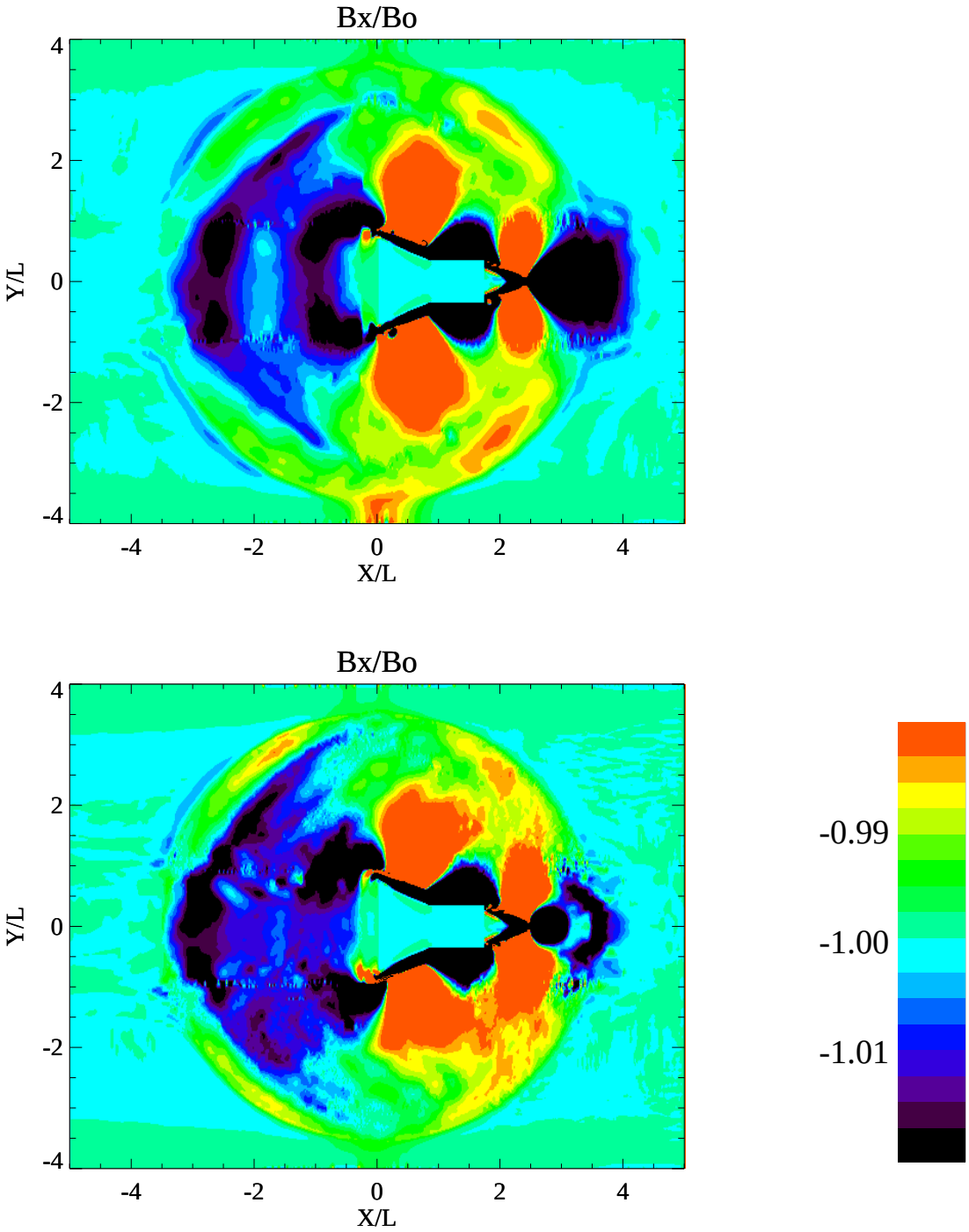

Figure 72. Magnetic field components $B_x(B_0)$ in the y-x plane. $U_0 = 200\,\mathrm{km/s}$, $M_A = 1.5$, $B_0 = 1500\,\mathrm{nT}$, $n = 5 \times 10^3\,\mathrm{cm}^{-3}$, $\beta_\mathrm{p} = 0.1$, $\beta_\mathrm{e} = 0.1$, $\theta_{bu} = 0^o$. Nonlinear saturation of the perturbations at $t = 1.0\,T_{ce}(0.12\,T_{transit})$ (case d', top; case e', bottom).

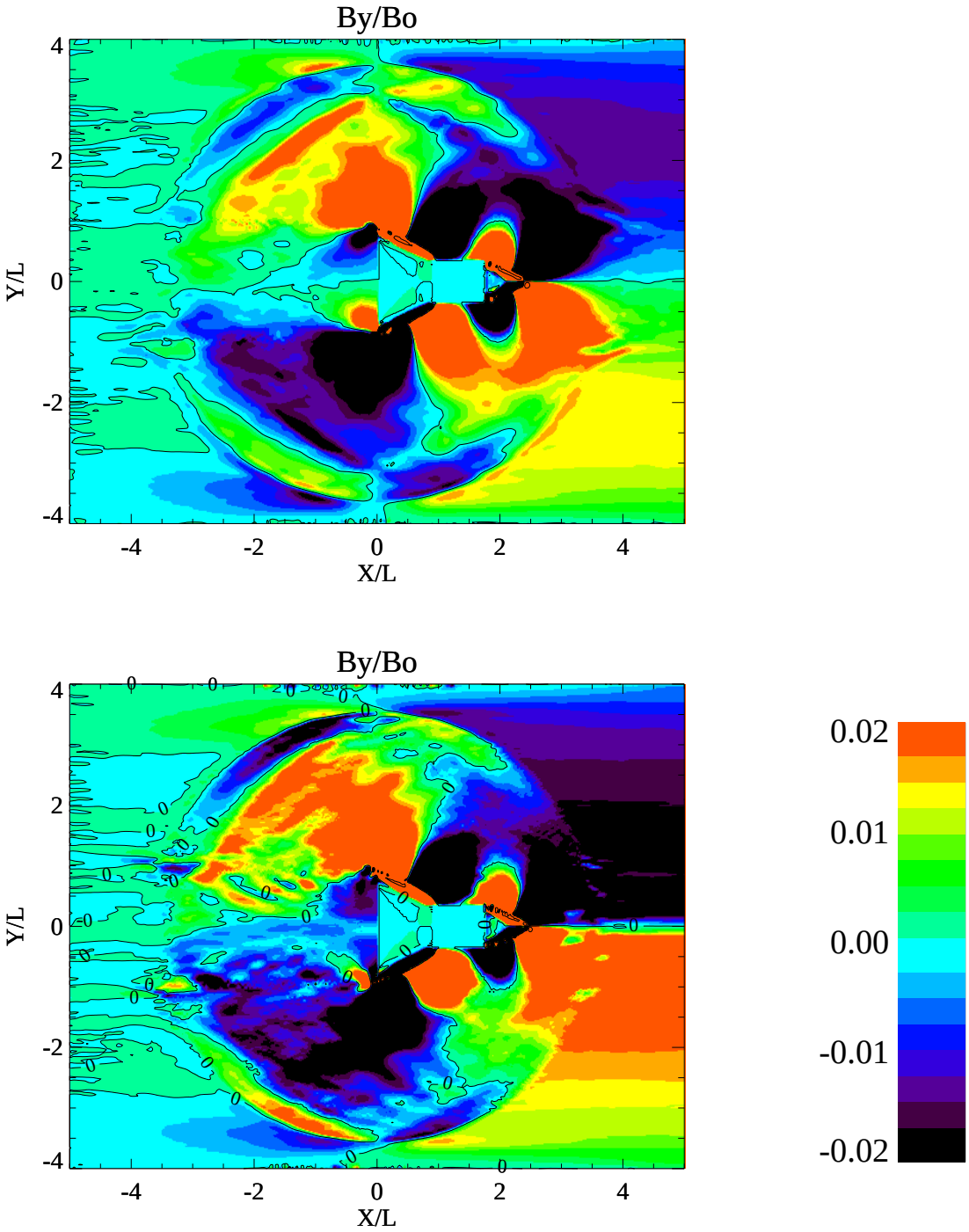

Figure 73. Magnetic field components $B_y(B_0)$ in the y-x plane. $U_0 = 200\,\mathrm{km/s}$, $M_A = 1.5$, $B_0 = 1500\,\mathrm{nT}$, $n = 5 \times 10^3\,\mathrm{cm}^{-3}$, $\beta_\mathrm{p} = 0.1$, $\beta_\mathrm{e} = 0.1$, $\theta_{bu} = 0^o$. Nonlinear saturation of the perturbations at $t = 1.0\,T_{ce}(0.12\,T_{transit})$ (case d', top; case e', bottom).

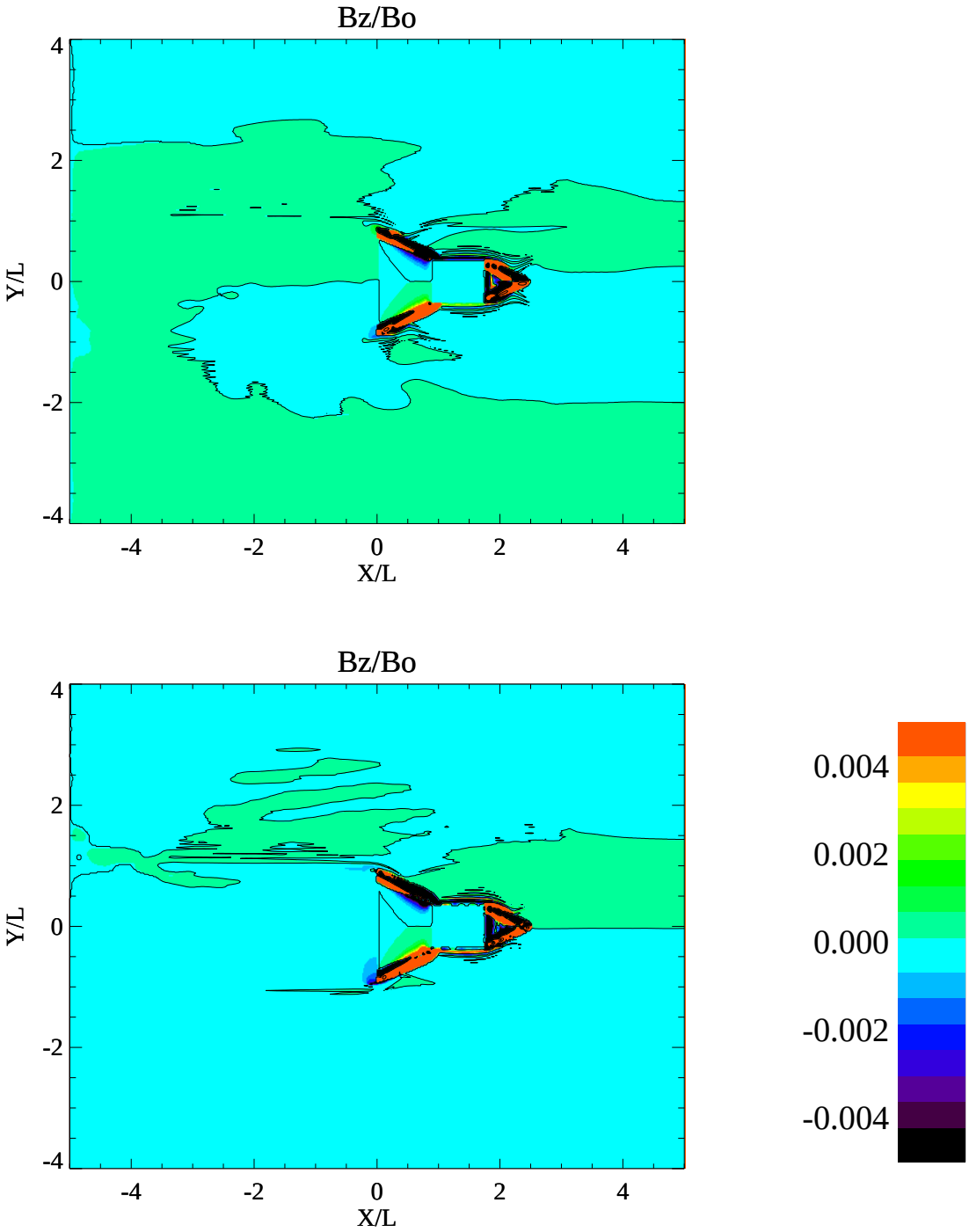

Figure 74. Magnetic field component $B_z(B_0)$ in the y-x plane. $U_0 = 200\,\mathrm{km/s}$, $M_A = 1.5$, $B_0 = 1500\,\mathrm{nT}$, $n = 5 \times 10^3\,\mathrm{cm}^{-3}$, $\beta_\mathrm{p} = 0.1$, $\beta_\mathrm{e} = 0.1$, $\theta_{bu} = 0^o$. Nonlinear saturation of the perturbations at $t = 1.0\,T_{ce}(0.12\,T_{transit})$ (case d', top; case e', bottom).

REPORT DOCUMENTATION PAGE

Form Approved
OMB No. 0704-0188

1. REPORT DATE *(DD-MM-YYYY)*	2. REPORT TYPE	3. DATES COVERED *(From - To)*
01-12-2010	Technical Memorandum	January 1, 2009 - September 1, 2010

4. TITLE AND SUBTITLE

The Interaction of the Solar Wind with Solar Probe Plus
— A 3D Hybrid Simulation
Report No. 2: The study for the distance 9.5Rs

5a. CONTRACT NUMBER

5b. GRANT NUMBER
NCC5–494

5c. PROGRAM ELEMENT NUMBER

6. AUTHOR(S)

Alexander S. Lipatov, Edward C. Sittler, Richard E. Hartle, and John F. Cooper

5d. PROJECT NUMBER

5e. TASK NUMBER

5f. WORK UNIT NUMBER
93672302010619

7. PERFORMING ORGANIZATION NAME(S) AND ADDRESS(ES)

Goddard Space Flight Center
Greenbelt, MD 20771

8. PERFORMING ORGANIZATION REPORT NUMBER
2011-00670

9. SPONSORING/MONITORING AGENCY NAME(S) AND ADDRESS(ES)

National Aeronautics and Space Administration
Washington, DC 20546-0001

10. SPONSORING/MONITOR'S ACRONYM(S)
NASA GSFC

11. SPONSORING/MONITORING REPORT NUMBER
TM-2010-215863

12. DISTRIBUTION/AVAILABILITY STATEMENT

Unclassified-Unlimited, Subject Category: 75, 90
Report available from the NASA Center for Aerospace Information, 7115 Standard Drive, Hanover, MD 21076. (443)757-5802

13. SUPPLEMENTARY NOTES

14. ABSTRACT

Our paper is a 2.5D and 3D numerical plasma models of the interaction of the solar wind (SW) with the Solar Probe Plus spacecraft (SPPSC). These results should be interpreted as a basic plasma model for which the derived SW interaction with spacecraft (SC) could have consequences for both plasma wave and electron plasma measurements on board SC in the inner heliosphere. We observe an excitation of the low frequency Alfven and whistler type wave directed by the magnetic field with an amplitude of the electromagnetic field oscillation about of (0.015-0.06) V/m. The compression waves and the jumps in an electric field with an amplitude of about 1.5 V/m and (12-18) V/m were also observed. The observed strong electromagnetic perturbations may be a crucial point in the electromagnetic measurements, which were planned in future Solar Probe Plus mission.

15. SUBJECT TERMS

Solar Probe Plus, plasma physics, astrophysics, solar wind; Alfv´en waves, Whistlers, ionospheres, atmospheres, induced magnetospheres, magnetic barrier, satellites

16. SECURITY CLASSIFICATION OF:			17. LIMITATION OF ABSTRACT	18. NUMBER OF PAGES	19b. NAME OF RESPONSIBLE PERSON
a. REPORT	b. ABSTRACT	c. THIS PAGE			Edward C. Sittler
U	U	U	U	117	19b. TELEPHONE NUMBER *(Include area code)* (301) 286-9215